A HIGH-FLUX COLD ATOM SOURCE BASED ON A NANO-STRUCTURED ATOM CHIP

Von der QUEST-Leibniz-Forschungsschule der
Gottfried Wilhelm Leibniz Universität Hannover

zur Erlangung des akademischen Grades
Doktor der Naturwissenschaften
- Dr. rer. nat. -
genehmigte Dissertation von

M.Sc. Hendrik Heine

2023

Referent: Prof. Dr. Ernst Maria Rasel
Korreferent: Dr. Dennis Schlippert
Korreferent: Prof. Dr. Kai Bongs
Datum der Promotion: 22.11.2023

Abstract

A high-flux cold atom source based on a nano-structured atom chip

Modern physics is challenged by existential questions about the most fundamental interactions of matter. While three of the four known fundamental forces are modeled in the grand unified theory [1], gravity seems to be incompatible in its current formulation. Many physicists search to unify them, but often the invented models violate well-tested assumptions such as the Einstein Equivalence Principle, a cornerstone of General Relativity. Despite macroscopic tests of this principle have already been carried out to high precision [2–4], quantum tests exploiting matter-wave interferometry [5–7] may provide complementary information [8] with even higher precision [9–11]. These yield their ultimate performance with Bose-Einstein condensates (BECs) over long evolution times as conventionally achieved by free-fall in space [12]. As such, a new generation of high performance BEC sources is required with strict budgets on size, weight and power demands. Efforts to miniaturize these sources have been pursued with promising results using atom chips [13–15], but further miniaturization of these setups is necessary.

In an attempt to simplify the usage of atom chips, the following thesis describes the development of a nano-structured atom chip that allows for single-beam magneto-optical trapping. The chip is implemented in a dedicated atom chip test facility that has been planned, built and characterized in the scope of this thesis. The facility features a state-of-the-art master oscillator power amplifier laser system, compact control electronics [13, 15–17] and a high-flux $2D^+$-MOT as an atomic source.

Despite the simplified setup, magneto-optical trapping of 1.1×10^9 Rubidium atoms was achieved within $1\,\mathrm{s}$ which is comparable to other atom chip setups and well above previous achievements with grating MOTs [18–23]. Illuminating the grating with a beam profile from a custom-built top-hat beam expander was instrumental to achieve balanced laser cooling in a large volume above the grating. This allowed to cool 4.7×10^8 atoms to $13\,\mathrm{\mu K}$ and transfer 2.4×10^8 atoms into a large-volume Ioffe-Pritchard type magnetic chip trap, demonstrating the required mode-matching between the laser cooled atoms and the magnetic trap. The trapped atoms were then used to characterize the magnetic field environment of the test facility using radio frequency spectroscopy gauging the surrounding magnetic bias coils.

These results demonstrate the feasibility of using a nano structured atom chip to build a single-beam BEC source which could become the foundation of future high-performance quantum sensors on ground and in space.

Key words: Atom chip, grating magneto-optical trap, gMOT, Bose-Einstein Condensate, BEC

Contents

CHAPTER 1

Introduction

The *holy grail* of cold atom physics was the first experimental observation of a Bose-Einstein condensate (BEC) as reported in 1995 by the groups of Cornell [24] and Ketterle [25]. Since then, BECs have become the cornerstone of many cold atom experiments due to their unique quantum properties and significant theoretical and experimental progress has been reported [26]. They were intensively studied in optical lattices and quantum simulators were realized that mimic the physics of strongly correlated condensed matter systems, giving insights into, e.g. high-temperature superconductors [27, 28]. Furthermore, BECs are interesting input states for atom interferometry on long time scales [12]. The availability of ultra-low expansion rates with effective temperatures down to the pK regime [29, 30] could allow for interferometry times in the order of many seconds as required for tests of the Einstein Equivalence Principle [11, 31], space gravity gradiometers [32, 33] or gravitational wave detection in the low frequency band [34–39]. These visionary endeavors will require a new generation of high-flux BEC sources that are small and rebust enough to enable such missions. The availability of such sources is thus of the highest interest to many fields of cold atom physics.

The first realization of a BEC was achieved in a time orbit potential (TOP) magnetic trap by forced evaporative cooling [24]. In this experiment, they loaded a magneto-optical trap (MOT) for $300\,\mathrm{s}$ to capture 1×10^7 atoms and subsequently cooled them optically to $20\,\mathrm{\mu K}$. This allowed them to trap the atoms magnetically where they applied RF-driven evaporative cooling over a duration of $70\,\mathrm{s}$ until the BEC transition was reached. The full experimental cycle time was thus on the order of many minutes driven by the initial loading time and the duration of evaporative cooling. This is intuitively very clear since the MOT was loaded directly from the background gas which was kept at very low pressure ($\sim 1 \times 10^{-11}\,\mathrm{mbar}$) in order to reduce background gas collisions in the magnetic trap experimental stage. If you want to utilize BECs for metrological applications though, it is vital to strongly reduce the time it takes to create them in order to minimize the dead time in which no measurement can be performed.

On the one hand, the initial MOT loading time can be greatly reduced by separating the vacuum system in two regions: The first region has a high background pressure of the source gas (e.g. $\sim 3 \times 10^{-7}\,\mathrm{mbar}$ for Rubidium) where cold atoms can be quickly gathered. They are then transferred into a second chamber where the pressure is very low and the evaporation to quantum degeneracy is performed. This splitting is commonly referred to as a Double-MOT setup with a 2D- and 3D-MOT. In these setups, orders of magnitude

higher atomic flux can be achieved, e.g. in [40] a flux of $\Phi = 2 \times 10^{10}\,\mathrm{s}^{-1}$ was reached[1] even with rather low cooling power available. It is thus possible to load $\sim 1 \times 10^9$ atoms within a few hundred milliseconds to cut down on the MOT loading time.

On the other hand, cooling towards quantum degeneracy has to speed up as well. Evaporative cooling relies on selectively removing atoms with the highest energies from an ensemble. The remaining atoms in the trap will then exchange energy and momentum through elastic collisions and re-thermalize at a lower temperature. As long as atoms above the average energy in the trap are removed, this is a cooling effect. The efficiency of this process is higher when more energy is taken away per particle that leaves the trap. It is thus more efficient to evaporate slow enough in order to allow for sufficient elastic collisions and remove only the far end of the energy distribution. However, in typical experimental realizations, the vacuum conditions are not perfect. External collisions with the background gas may transfer sufficient energy to an atom to leave the trap which sets an upper bound for the evaporation time. Therefore, the timescale in which evaporative cooling should be applied is dominated by two things: The rate of elastic collisions in the trap and the rate of atomic loss. If you evaporate too quickly (much quicker than the rate of elastic collisions), the atoms will not have enough time to exchange energy and the cooling becomes inefficient. If you evaporate too slowly (much longer than the lifetime of the trap), the evaporative cooling itself is efficient but many atoms are lost to background gas collisions which in turn is inefficient as well. It would thus be ideal to use a very high rate of elastic collisions while maintaining long lifetimes of the trap.

The two-body elastic collision rate Γ_{el} in a harmonic trap is given by [41]

$$\Gamma_{\mathrm{el}} \equiv n\,\sigma\,v_r \tag{1.1}$$

where $n \equiv N/V$ is the density of N atoms in the volume V, $\sigma = 8\pi a^2$ is the scattering cross section with the s-wave scattering length a and $v_r = \sqrt{2}\bar{v}$ is the relative velocity between the scattering atoms with mean velocity $\bar{v}$ [42]. The volume can be described by the product of the characteristic lengths in an harmonic oscillator

$$V = \prod_{i=x,y,z} \sqrt{\frac{2\pi k_{\mathrm{B}} T}{m\omega_i^2}} = \left(2\pi \frac{k_{\mathrm{B}} T}{m\bar{\omega}}\right)^{3/2} \tag{1.2}$$

where k_{B} is Boltzmann's constant, T is the temperature of the ensemble, m is the mass of the atom and $\bar{\omega} \equiv \sqrt[3]{\omega_x\,\omega_y\,\omega_z}$ is the geometric trap frequency. Substituting the mean velocity from a Maxwell-Boltzmann distribution

$$\bar{v} = \sqrt{\frac{8k_{\mathrm{B}} T}{\pi m}} \tag{1.3}$$

---

[1] Note that this is only the flux sent out by the 2D-MOT which does not necessarily mean that all of these atoms can be captured in a subsequent 3D-MOT. For this to happen, the capture velocity band needs to be sufficiently overlapped.

finally yields with equations 1.1 and 1.2

$$\Gamma_{\text{el}} = \frac{8\sqrt{2}a^2 m}{\pi k_{\text{B}}} \frac{N\bar{\omega}^3}{T} \propto \frac{N\,\omega_x\,\omega_y\,\omega_z}{T} \tag{1.4}$$

which is proportional to the product of the Eigenfrequencies of the trap. It is therefore useful to trap the ensemble in a high frequency trap in order to increase the elastic collision rate. In turn, the trap frequency ω_i in the direction $i = \{x,y,z\}$ of a magnetic trap is governed by the curvature of the magnetic field [43]

$$\omega_i = \sqrt{\frac{\mu_{\text{m}}}{m}\frac{\text{d}^2 B}{\text{d}x_i^2}}. \tag{1.5}$$

It can be shown [44] that for the TOP trap in the outlined experiment above the time averaged field is given by

$$\bar{B} = B_b + \frac{C_2^2}{4B_b}\left(x^2 + y^2 + 8z^2\right) \tag{1.6}$$

where B_b is the magnitude of the rotating field and

$$C_2 = -3\mu_m I \frac{a^2 b}{2\left(a^2 + b^2\right)^{5/2}} \stackrel{a \approx b}{\sim} \frac{I}{a^2} \tag{1.7}$$

is a geometric factor for a pair of coils with radius a separated by a distance $2b$ in which a current I flows. For this magnetic trap, the trap frequencies are then given by

$$(\omega_x,\omega_y,\omega_z) = \sqrt{\frac{\mu_{\text{m}}}{4mB_b}}C_2\left(\sqrt{2}, \sqrt{2}, 4\right) \propto C_2 \tag{1.8}$$

For typical experimental coil setups, $a \approx b$ and thus $\omega \sim I/a^2$ which favors small coil radii and high currents. Experimentally, an external coil is limited in size by the outer diameter of the vacuum chamber a_{min} and an increase in current strongly increases the dissipated Power $P = I^2 R$ following Ohm's law. Therefore, pure coil setups around a vacuum chamber are intrinsically limited when an increase in trap frequency is desired on a tight power budget. A solution to this challenge is to drastically reduce the distance from the field-generating structure to the atoms by placing wires directly inside the vacuum chamber. This is the core idea of the atom chip where microfabricated wires are placed on a wafer in various configurations to generate the required magnetic fields (see chapter 2).

Indeed, implementations of such atom chip devices have successfully proven to be reasonably compact high-flux BEC sources [14, 15] with up to 4×10^5 atoms in the BEC every 1.6 s. However, there are still open challenges that need to be tackled:

- When it comes to real space mission scenarios, the requirements on **s**ize, **w**eight, **a**nd

power demands ("SWAP budget") are crucial. For such missions to happen, big steps in SWAP reduction have to be developed since they are still not possible with what is available today.

- The initial magneto-optical trap is typically realized using multiple beams. For example, four optical beams are used in a mirror-MOT out of which two are reflected off of a mirror surface on the atom chip. Consequently, the required light balance for laser cooling relies on the stability of all beams towards each other and any drift or misalignment over the lifetime of the mission may result in a critical failure. While readjustments are commonly performed with systems on ground, they are virtually impossible in space.

- High precision experiments typically require the vacuum chamber to be encapsulated inside a magnetic shield which is very bulky and contributes heavily to the overall weight budget. Therefore, reducing the size of the internal components is a very efficient way to reduce the weight of the magnetic shield.

A promising way to address these challenges is the implementation of single-beam optical cooling. Two approaches prevail: Pyramidal reflectors [45–49] that reflect an incoming beam into their hollow core and planar optical reflection gratings [18–21, 50–53] that use the diffraction of light. While the reflectors hide the atomic cloud in their inside, making detection very difficult[1], the grating preserves full optical access from all sides and is thus an interesting approach to pursue. In addition, gratings are manufactured the same way as atom chips by using lithography and other micro production technologies. Therefore, the combination of these two is naturally synergetic with strong potential for miniaturization and scalability into mass-production. However, current implementations of such grating MOTs [19–21, 50–53] have neither demonstrated high atom numbers, nor high flux or low temperatures. They were mainly implemented in simple vapor cells without dedicated high-flux atomic sources which justifies further investigation.

The following chapters present the implementation of an optical grating on an atom chip combining the advantages of versatile atomic trapping from an atom chip with the simplicity of a grating MOT. After a brief introduction into the fundamentals of the grating MOT and atom chips (chapter 2), a test facility (chapter 3) is outlined which was planned, constructed and characterized in the scope of this thesis. The facility features a $2D^+$-MOT as an atomic source, a master oscillator power amplifier (MOPA) laser system and electronics to control the full atom-optical experiment. The performance of the atom chip is evaluated in chapter 4 where results on magneto-optical trapping, optical cooling, magnetic trapping and evaporative cooling are presented. The atoms are then used as a magnetic field probe to characterize the bias coils of the test facility. Finally, chapter 5 outlines the roadmap of further developments and the next generation of atom chips.

---

1 This is especially difficult in the absence of gravitational acceleration in space which would otherwise pull the atoms out of this region. In space, the atoms will remain within.

CHAPTER 2

A nano-structured atom chip

This chapter introduces the idea of the grating magneto-optical trap (gMOT) and outlines the combination with an atom chip to achieve a simplified source of cold atoms. The realized atom chip of this work is presented and the force equations for the grating MOT are derived. Finally, the forces in the gMOT are calculated in a computer simulation to study the capture of atoms from an atomic beam.

2.1 Grating magneto-optical trap

Magneto-optical traps (MOTs) use light forces to cool and capture neutral atoms. The exerted force of the light acts, on average, in the direction of light propagation which is why light needs to be applied from all spatial directions. In the standard approach, three pairs of counter-propagating light beams are aligned perpendicularly to each other intersecting in a common point, much like in a Cartesian coordinate system. This requires a total of six independent light beams. However, it was found that it is not strictly required that the beams are perpendicular to each other: For confinement in N dimensions, only N+1 beams are required. Therefore, 3D-confinement is possible with 4 beams, e.g. in a tetrahedron-like configuration where the light is shined in along the symmetry axes through the four vertices. This can be realized not only by independent beams but also by using a single large beam and angled reflectors such as separate [48] or hollow pyramidal [45, 47, 54, 55] mirrors. The benefit of this approach is that the reflected secondary beams are derived

Fig. 2.1: Principle of the grating MOT. Three binary reflection gratings are illuminated from a single large incoming beam (top) to diffract light into a total of six secondary beams. The three inwards diffracted beams are used as the beams for the gMOT together with the incoming beam.

from the primary incoming beam which means that any power fluctuation is common to all beams. This increases the stability of the system as laser cooling relies on the relative intensity between light beams and prevents de-adjustments as degrees of freedom are
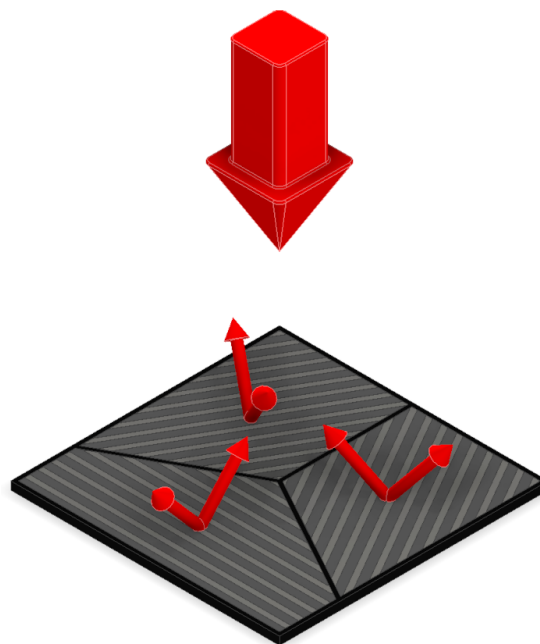
removed. Furthermore, it greatly simplifies the optical setup of the laser system as only a single input beam is required.

However, the atoms are then trapped in the volume of the surrounding reflectors and their analysis becomes difficult as they block the side view. The natural extension of this idea is to generate the light deflection from planar optics through diffraction as illustrated in figure 2.1. Three binary reflection gratings are manufactured in a pattern of equilateral triangles so that each individual grating section diffracts light in two diffraction orders for a total of six diffracted beams. The three inwards pointing beams are used for magneto-optical trapping together with the incoming beam. The diffraction angle of the gratings is calculated using the grating equation

$$m\lambda = d(\sin\theta_m - \sin\alpha) \tag{2.1}$$

where α is the angle of incidence, λ is the wavelength of the light, d is the period of the grating and m is the diffraction order with corresponding diffraction angle θ_m. For perpendicular illumination ($\alpha = 0$), diffraction is generated pairwise in symmetrical orders $\pm m$ so that next to the desired inwards diffraction order, also an outwards diffraction order is created. Choosing $\lambda < d < 2\lambda$ ensures that only a single pair of orders with $m = \pm 1$ is created in addition to the zero order $m = 0$. Suppressing the latter is achieved by choosing a suitable height $h \approx \lambda/4$ of the binary grating to cause destructive interference[1]. This way, a nano-structured grating chip can generate all required light beams for magneto-optical trapping from a single input beam. This configuration is referred to as a grating magneto-optical trap (gMOT).

2.1.1 Light balance

Light balance in the grating MOT configuration is achieved when the intensity-weighted wave vectors

$$\vec{s} = \sum_i I_i \vec{k}_i \tag{2.2}$$

of all contributing light beams compensate each other [18] such that $\vec{s} = \vec{0}$. This problem can be split into two components: Radial components parallel to the grating surface and axial components along the incoming beam, which is assumed to be normal to the grating surface. In radial direction, all contributions stem from diffracted beams so that the balance on the central axis is always achieved for radially symmetric grating illumination. Axial balance is achieved when the projection of all diffracted beams onto the axial direction compensate the intensity of the incoming beam (see figure 2.2).

When the grating is illuminated with a local intensity $I(\vec{r})$ at some position $\vec{r}$, the diffracted intensity is halved due to the symmetric diffraction into two orders (± 1) but is also amplified due to area compression: As the beam is diffracted to the side, the width of the beam decreases by $w_o/w_i = \cos\theta$ and consequently the intensity is enhanced by

---

[1] Additional phases from the sidewalls of the grating cause a deviation from the ideal height $h = \lambda/4$ which is in practice counteracted by etch depth adaption [56].
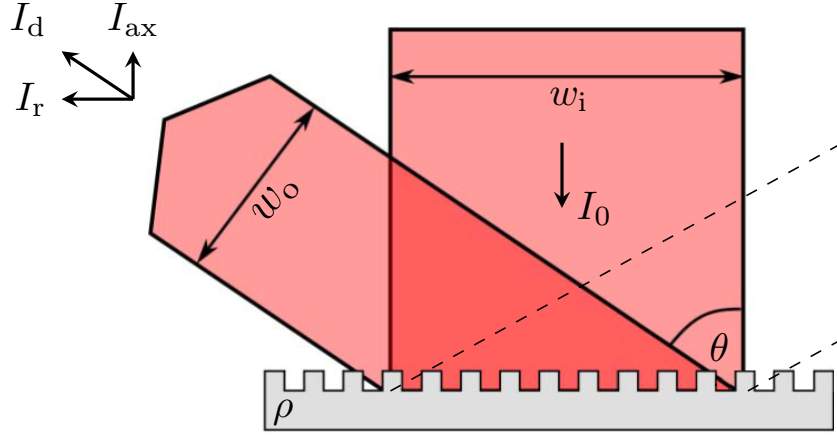
Figure 2.2: Light diffraction on a 1D grating with symmertrical first order diffraction (red & dashed). The outgoing intensity I_d is first halved due to the symmetric power splitting into the diffraction orders but then increased by $w_i/w_o = 1/\cos\theta$ due to 1D area compression. After diffraction, the outgoing intensity can be split into radial (I_r) and axial (I_{ax}) components. The finite power reflectivity ρ of the grating diminishes the intensity further. Figure modified from [51].

the inverse of that. Furthermore, the reflectivity of the grating is finite and absorption in the material further reduces the diffracted power P_d by a reflectivity factor ρ. With these consideration, the diffracted intensity I_d reads

$$I_d = \frac{P_d}{A_d} = \frac{\frac{\rho}{2}P_0}{A_0\frac{w_o}{w_i}} = \frac{\rho}{2\cos(\theta)}I(\vec{r}), \tag{2.3}$$

where the upwards axial projection

$$I_{ax} = I_d\cos(\theta) = \frac{\rho}{2}I(\vec{r}), \tag{2.4}$$

is independent of the diffraction angle θ. In total, if N grating sections are used, axial intensity balance is achieved in the center when

$$I(0) = N * I_{ax} = N\frac{\rho}{2}I(\vec{r}) \tag{2.5}$$

which means that the materials' power reflectivity should be $\rho = 2/N$ for constant intensities $I(\vec{r}) = I_0$ and each diffracted beam carries $1/N$ of the power. In practice, the power reflectivity of the grating is often worse due to additional losses, so that for $N = 3$ grating sections typically Aluminum is used with $\rho_{Al} \approx 87\% > 2/3$ [19, 57].

For non-homogeneous light illumination $I(\vec{r}) \neq I_0$, the problem becomes more complex: Consider, for example, a Gaussian beam illumination where the center of the Gaussian is matched to the center of the gratings. The strong central intensity of the Gaussian beam needs to be compensated by three diffracted beams. For a given point on the central
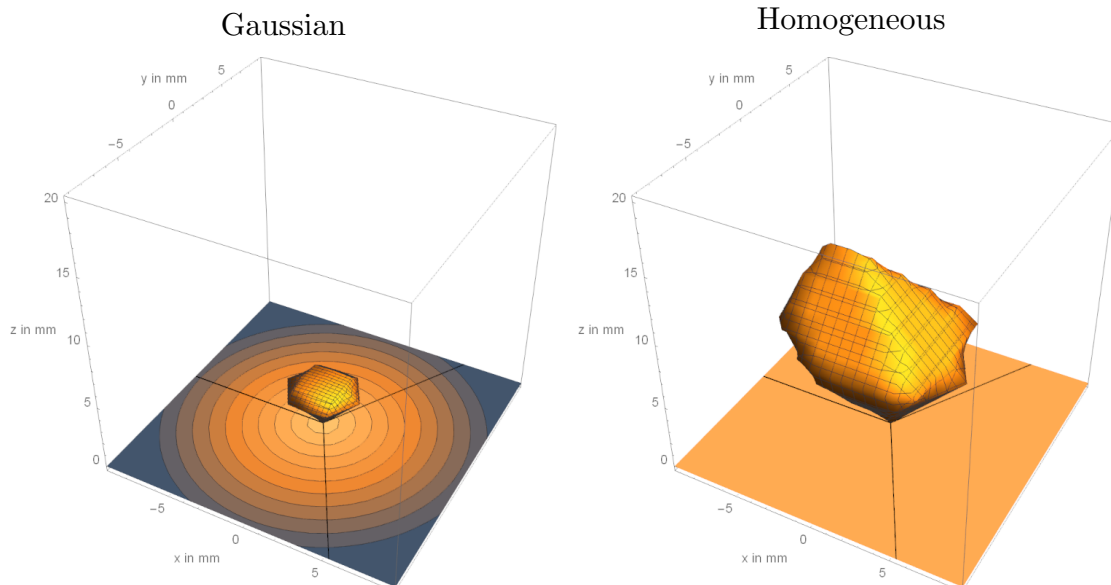
Figure 2.3: Comparison of balanced light intensities for grating illumination with a Gaussian beam (left) and a homogeneous intensity distribution (right). Each grating zone diffracts light in its respective $\pm 1^{\text{st}}$ order where all inwards pointing orders intersect with an incoming beam from the top. Balanced laser cooling is achieved when the intensity-weighted wave vectors $\vec{s} = \sum_i I_i \vec{k}_i$ compensate each other. For Gaussian illumination at elevated heights, the diffracted orders fail to compensate the strong input beam due to the reduced radial intensity. This issue is circumvented for homogeneous intensity illumination (right) which greatly increases the volume in which balanced laser cooling may happen. The plot shows regions in which the imbalance is small, e.g. here $|\vec{s}| < 5\,\%$. Sampling the full volume with random points allows to calculate the volume of balanced laser cooling as the fraction of samples for which the imbalance is small. For homogeneous illumination of this grating, the volume is estimated to be $0.35\,\text{cm}$.

symmetry axis, the light contributions from the diffracted beams can be traced back to respective radial positions on the grating plane. The local intensity at these spots $I(\vec{r})$ determines the intensity of the diffracted beams. Higher axial positions will trace back to further radial positions which are lower in intensity for a Gaussian beam. Therefore, intensity balance can only be achieved at a specific height where the power reflectivity ρ is just right. Deviations from this position will cause axial intensity imbalance though it would be directed towards the point of balance. However, in radial direction the light imbalance will always be directed outwards making laser cooling difficult to achieve without additional spatial inwards forces.

The volume in which balanced laser cooling is possible can be visualized by calculating the norm of the balance vector (equation 2.2) spatially. For every point $\vec{p} = (x,y,z)$ in the volume above the grating, one needs to find the intensities $I_i(x,y,z)$ of all contributing wave vectors $\vec{k}_i$. These originate from the illumination profile of the grating $I_0(x',y')$ at some position (x',y') on the grating plane. This point can be found by tracing back $\vec{p}$ along

the unit vector $\vec{\hat{k}}_i$ for a distance $z/\cos(\theta)$ until it reaches the grating plane where $I_0(x',y')$ holds. Then the illumination profile only needs to be evaluated at

$$I_i(x,y,z) = I_0 \left(x - \frac{z}{\cos(\theta)} k_{i,x}, y - \frac{z}{\cos(\theta)} k_{i,y} \right). \tag{2.6}$$

Figure 2.3 plots the outcome into a region plot where $|\vec{s}| < 5\,\%$. As it can be seen by comparison, the volume in which balanced laser cooling is possible is quite limited for a Gaussian illumination of the grating. The diffracted beams simply fail to compensate the strong central part of the beam at elevated heights as the radial intensity decreases. In contrast, for flat intensity distributions, the volume of balanced intensities is only limited by the spatial extend of the grating. The maximum volume was estimated to be $\approx 0.35\,\mathrm{cm}^3$ by sampling random points in a cubic volume above the $2\,\mathrm{cm} \times 2\,\mathrm{cm}$ grating shown in figure 2.3. For every point, equation 2.2 is evaluated and the fraction of points with small imbalance is referenced to the full volume of sampling.

With these considerations, the experimental implementation will strongly rely on the illumination profile of the grating where realizing a homogeneous grating illumination is key to achieve balanced laser cooling in a large volume. Therefore, a tophat beam expander was designed and built in the scope of this thesis (see section 4.1) which was used to achieve the experimental results.

2.2 Introduction to atom chips

Generating spatially varying magnetic fields for atomic physics is traditionally done using coils around the vacuum chamber. On the one hand, homogeneous fields are achieved with coils in the so-called Helmholtz configuration where a pair of coils is separated by a distance equal to their radius and an equal parallel current is sent through them. This creates a homogeneous field in the center of the arrangement. On the other hand, inhomogeneous fields as required for magnetic and magneto-optical trapping are achieved using anti-parallel currents. As detailed in the introduction (chapter 1), coil setups scale intrinsically unfavorable with the size as the field decays quickly with the distance. In practice, this is often compensated by using very high currents which may require active cooling solutions such as water cooling.

In contrast, atom chips seek to achieve strong magnetic fields by being close to the atoms. Bringing the wires into the vacuum chamber allows to benefit from the very strong gradients and curvatures in the close vicinity to the wire, even at moderate currents. While this brings its own challenges in terms of vacuum requirements and ther-

Fig. 2.4: Basic principle of the atom chip. A current I_0 generates a circular magnetic field around a wire. When it is compensated by an external magnetic bias field B_0 at a given position z_0 above the wire, the total field is locally shaped like a 2D-quadrupole. Figure modified from [43].

mal management, it also opens many possibilities for applications that are on a strict power budget. The basic principle of the atom chip is depicted in figure 2.4 and works as follows:

Consider a wire segment of length $\vec{dl}$ at position $\vec{r}'$ in which a current I_0 flows. Then the magnetic flux density at point $\vec{r}$ generated by that wire is described by the law of Biot-Savart

$$\mathrm{d}\vec{B}(\vec{r}) = \frac{\mu_0}{4\pi} I_0 \mathrm{d}\vec{l} \times \frac{\vec{r} - \vec{r}'}{|\vec{r} - \vec{r}'|^3} \tag{2.7}$$

where μ_0 is the magnetic permeability. From the cross product it is evident that the direction of the magnetic field vector is always perpendicular to the wire and therefore the magnetic field lines form a circle around the wire segment. The magnitude of the field drops as $1/|\vec{r}|$. Next, an external magnetic bias field is used to compensate the circular field at some distance z_0 above the wire. The resulting total field is locally shaped like a 2D quadrupole field around z_0 that stretches along the wire. As such, it features a local
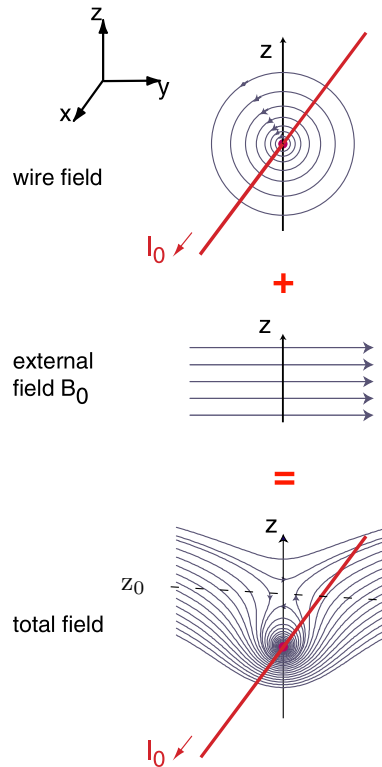
minimum with vanishing magnitude and the principal axes are rotated by 45° with respect to the external field. This field is very useful as it can be used for, e.g. magneto-optical trapping or (guided) magnetic traps. However, it is only generated in two dimensions and full confinement can not be achieved with a single wire strip alone. Adding more wires in perpendicular directions allows to shape the magnetic field landscape in a more complex manner. Many different combinations of wires can be found in the extensive literature (e.g. [43, 58, 59]) but here we will just focus on the basic building blocks relevant to this work which is the "O" and "H/Z" shape.

2.2.1 Multi-wire combinations

The above example considered only a single 1D wire which will only generate field components in the perpendicular directions to its extent. For a full 3D magnetic field, more complex wire structures have to be laid out. The total magnetic field is then derived following the superposition principle where even the most complex wires structures can be approximated by adding more subsets of strings. More complicated wire structures are typically composed of simpler subsets of wire settings such as single wires and sets of parallel wires. Let us therefore first consider a set of parallel wires with either identical parallel or antiparallel currents as depicted in figure 2.5.

For parallel currents, both wires create identical fields that globally add up as if they were composing a single wire. However, right in between the wires, the field vanishes due to field components coming once from the left and once from the right side of the curling magnetic field. This field configuration appears locally like a quadrupole field which is tilted by 45° with respect to the wire plane. It can be shifted up or down using an external bias field aligned along the axis of wire separation. Note, that far away where the wire separation becomes negligible in comparison to the distance to the wire, this configuration behaves exactly like the single wire case described in the previous section. Though in contrast, for stronger external fields, two separate quadrupoles will emerge, one above each individual wire.

In contrast to parallel currents, the behavior completely changes when one of the currents in reversed: For anti-parallel currents, the fields add up in the center between the wires and point in the direction perpendicular to the wire plane. Following the idea of field compensation from the previous section, applying an external bias field in the vertical direction may compensate the wire field at some height above the wire plane. At this point, again a quadrupole field emerges but this time the orientation is not tilted with respect to the wire plane but is upright. Note, that due to the symmetry of the arrangement two separate quadrupoles are generated, one above and one below the wire plane.
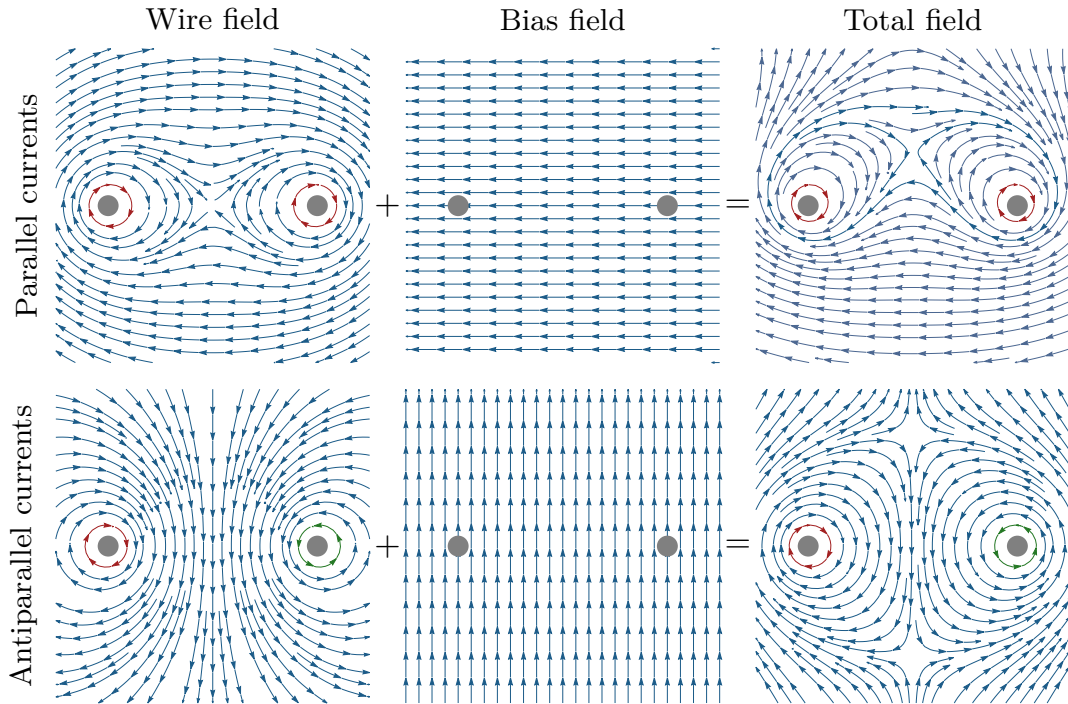
Figure 2.5: Generation of magnetic field configurations with two parallel wires (grey) and a magnetic bias field. **Top row:** For equal parallel currents, the wire fields (left) globally add up but locally compensate each other in the central point between them and a local quadrupole field is created. Overlaying an aligned bias field (middle) may then shift its position up or down in the total field (right). Note, that the onset of the far field behavior becomes visible when the height is much bigger than the wire separation. Then both wires appear like a single wire (see figure 2.4). **Bottom row:** For anti-parallel currents, the magnetic fields add up in between the wires. Overlaying an aligned bias field (middle) then compensates the wire field at some positions above and below the wire plane where an upright quadrupole field is generated (right).

2.2.2 Ioffe-Pritchard-type magnetic chip trap

A Ioffe-Pritchard type magnetic trap is known as the workhorse for atomic physics with magnetic traps. In the traditional configuration, four "Ioffe bars" arranged in a square along a vacuum chamber would have pairwise opposite currents in neighboring bars to generate a quadrupole field in the center of the arrangement [61] (see figure 2.6a). Atoms in the center would be radially confined but could move axially in the magnetic field zero along the bar direction. Therefore, an additional field is overlaid in the axial direction by using two Helmholtz-like coils but with greater separation which generates a parabola-shaped potential for a full 3D confinement (figure 2.6c). The advantage of this configuration is that the parabola potential maintains a non-zero field in the center of the trap where the total magnetic field would otherwise become zero. This prevents so-called Majorana losses where the Lamor frequency, which is proportional to the magnetic field, becomes zero and allows an atom to change its magnetic sub-state and leave the trap.
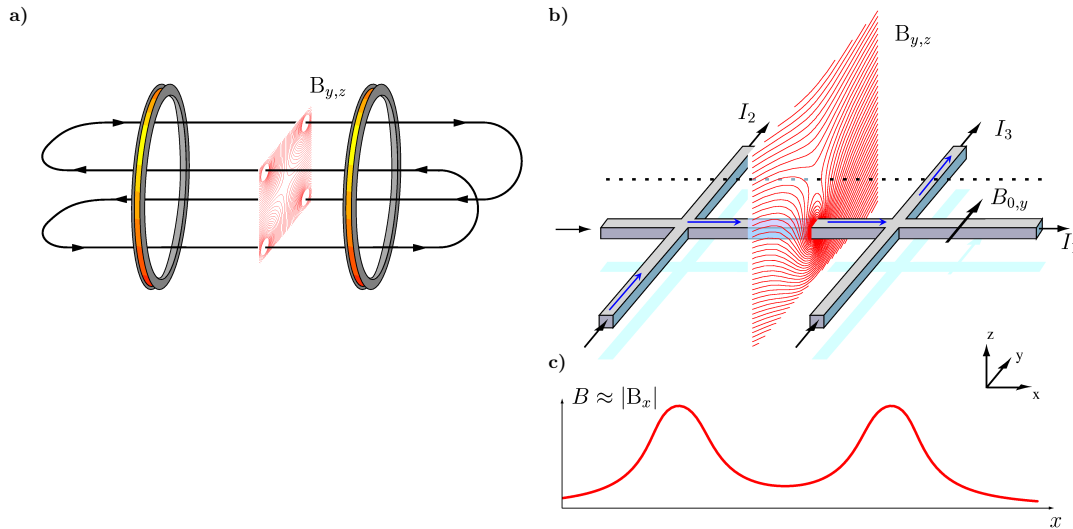
Figure 2.6: Comparison of a Ioffe-Pritchard type magnetic trap for traditional macroscopic structures a) and atom chips structures b). In the traditional case, four wires with neighbor-wise alternating currents create a quadrupole field in the center of the arrangement which provides radial trapping. Along the axial direction, a pair of Helmholtz-coils with extended distance causes axial confinement as indicated in c). For the atom chip wires, similar radial confinement is provided by the single horizontal wire together with an external field $B_{0,y}$. The axial field contributions are caused by the parallel wires. This wire configuration is known as an "H"-trap due to its shape. Note that the wires can be truncated into a "Z"-shape through which only a single current needs to be sent (blue arrows in b). Figure modified from [60].

In analogy, such a trap can also be generated with the tools of an atom chip. The quadrupole field from the single-wire case behaves exactly like the field of the Ioffe-Bars: The field is strong in the direction perpendicular to the wire but vanishes along the wire axis. What is missing is again the axial confinement along the wire direction and the non-zero trap bottom field. This purpose can be fulfilled by a pair of wires with parallel currents. If the magnetic field minimum is held above the wire plane by the single wire and an external field, there is a natural non-zero field by a set of parallel wires which acts as the trap bottom field. In addition, they provide a parabola-like potential with a minimum in the center. The axial field can be tuned by applying an additional external field which moves the field components of the parallel wires up or down. The full configuration consists of a single horizontal wire with two vertical parallel wires of equal parallel current in an "H"-shape as depicted in figure 2.6b). This configuration can be simplified to require only a single current by trimming the parallel wires into a "Z"-shape (blue arrows in figure 2.6b). The current then flows from e.g. the bottom left of a side wire through the central horizontal wire and the top right of the second side wire. Note, that by trimming the wires, the total field strength of the wires is reduced due to the shorter wire length.

2.2.3 Upright magnetic quadrupole field

The gMOT needs a 3D upright magnetic quadrupole field to capture atoms. In traditional coil setups, this field would be generated by a pair of Anti-Helmholtz coils around the vacuum chamber which generates a magnetic quadrupole field along the coil separation axis. The required gradients around $\sim 10 - 20\,\mathrm{G/cm}$ [19, 50, 52] are commonly obtained using such coils but with an atom chip available, one might as well make use of it. As previously discussed, such a field can be generated in 2D by considering the parallel-wire case with anti-parallel currents where two upright quadrupoles emerged when a perpendicular external field is added. This field is symmetric under rotation around the vertical axis: When an identical set of wires is taken and rotated, the quadrupole orientation is maintained and the contributions add up. A full 3D field is therefore obtained by rotation of the wires into either a rectangular wire arrangement with pairwise opposing wires or - as the more continuous version - a wire loop. Such a wire loop is illustrated in figure 2.7 as a planar coil which was extended to eight windings to increase the field strength. As long as the coil is wound symmetric, i.e. every strip of wire has an opposite partner of equal length the quadrupole field is centered. Note, that

Fig. 2.7: Upright magnetic quadrupole field from a wire loop with external bias field perpendicular to the wire plane. The vicinity of the magnetic field zeroes has been colored red.

this geometry is also well-behaved in the sense that weak external fields parallel to the wire plane will just move around the minimum in its respective direction. This way, it is easy to align the position of the MOT with respect to the light fields. The achievable gradients depend on the exact geometry of the loop, the number of windings, the applied current and the position of the field minimum. Notably, when the field minimum is moved further away from the loop, also the gradient decreases. This gives an effective coupling of the gradient with the minimum position. Therefore, both the current in the loop and in the coil must be adjusted if the field minimum is to be shifted along the vertical to maintain the gradient.

In conclusion, it is possible to replace the bulky high-current quadrupole coils for magneto-optical traps with just an in-vacuum wire loop and a significantly smaller external bias coil. The bias coil is typically required anyway to compensate external magnetic fields, so it just has to be made a little stronger to keep up with the fields of the atom chip.
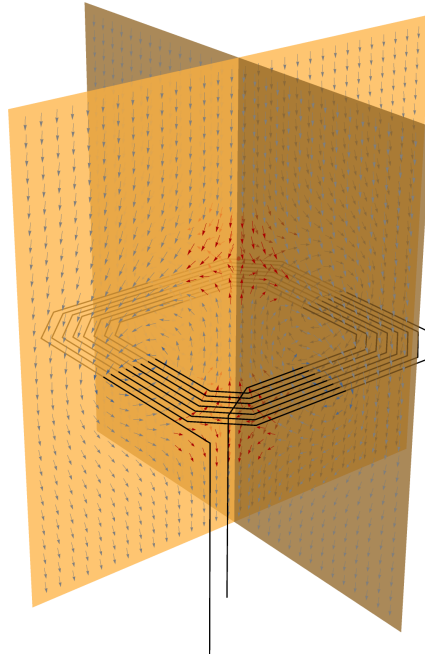
2.3 Grating atom chip

The atom chips employed for the high-flux BEC sources of our group [14, 15, 62, 63] are well established and feature a multi-layer chip assembly. They are based on a copper mount for heat conduction which houses wires for the magnetic field of the MOT and H-wires for a large-volume magnetic trap (see section 2.2.2). This initial magnetic trap is realized by additional support through the first atom chip layer ("Base-Chip") which features a Z-structure. This is to transfer a large fraction of the optically cooled atoms into the magnetic trap. From there, the atoms are further transferred into a tighter trap that features higher trap frequencies for evaporative cooling towards the BEC. The final trap is realized by combining the Z-structure on the Base-Chip with an additional smaller Z-structure on the final top-most chip layer ("Science-Chip"). In principle, the planar grating of the gMOT is a very interesting candidate to be combined with these technologies. As previously discussed, the required magnetic field can be readily obtained through atom chip wires and the central challenge becomes adding the grating to the chip. Both structures are manufactured using lithography techniques and therefore their combination seem naturally compatible albeit not necessarily easy from the manufacturing requirements.

The critical step when working with atom chips is the transfer from the magneto-optical into the magnetic trap: While the shape of the magnetic trap is prolate (cigar-shaped) along the central horizontal wire, the magneto-optically trapped atoms may have a different spatial distribution. Mode-matching between the two shapes will play a significant role for an efficient transfer into the magnetic trap. For the previously used atom chips, a mirror-MOT is employed that spatially matches well with the magnetic trap in its similar prolate shape[1]. However, gMOTs were observed to be mostly oblate[2] (pancake-shaped) which may lead to a significantly reduced transfer efficiency. Studying the magnetic trap transfer is therefore of key importance for the realization of an efficient grating atom chip.

To combine the atom chip with the grating, one needs to structure the top-most atom chip layer (i.e. the Science-Chip) with the grating pattern. From an engineering point of view, this is quite challenging as the atom chip wires give an uneven surface onto which the required laser- or electron-beam lithography can not be applied well. The wires would have to be either embedded in the surface or an additional planarization layer. Before this engineering challenge is taken, it is worth to investigate if the transfer into the magnetic trap works well for the gMOT. To test this, the Science-Chip layer can be replaced with a plain grating chip of similar height though this removes the capability of the chip to generate high-frequency magnetic traps as required for evaporative cooling. The applicability of the gMOT technology can then be estimated based on previous experiences

---

1   Similarly to the magnetic trap, the gradient from the utilized "U"-wire is strong in the radial direction and much weaker axially.

2   The shape of the gMOT is determined by the spring constants $\left(\kappa_{\parallel}, \kappa_{\perp}\right) \propto \left(\frac{1}{4}\sin\theta\tan\theta, 1-\cos\theta\right)$ of the trap which depends on the diffraction angle θ [50]. For angles below the tetrahedron angle $\theta < \theta_t = \arccos(1/3) \approx 70.5°$, $\kappa_{\parallel} < \kappa_{\perp}$ and the shape becomes oblate. It only becomes prolate for $\theta > \theta_t$ but perpendicular to the grating plane which would be even worse for the overlap with the magnetic trap.
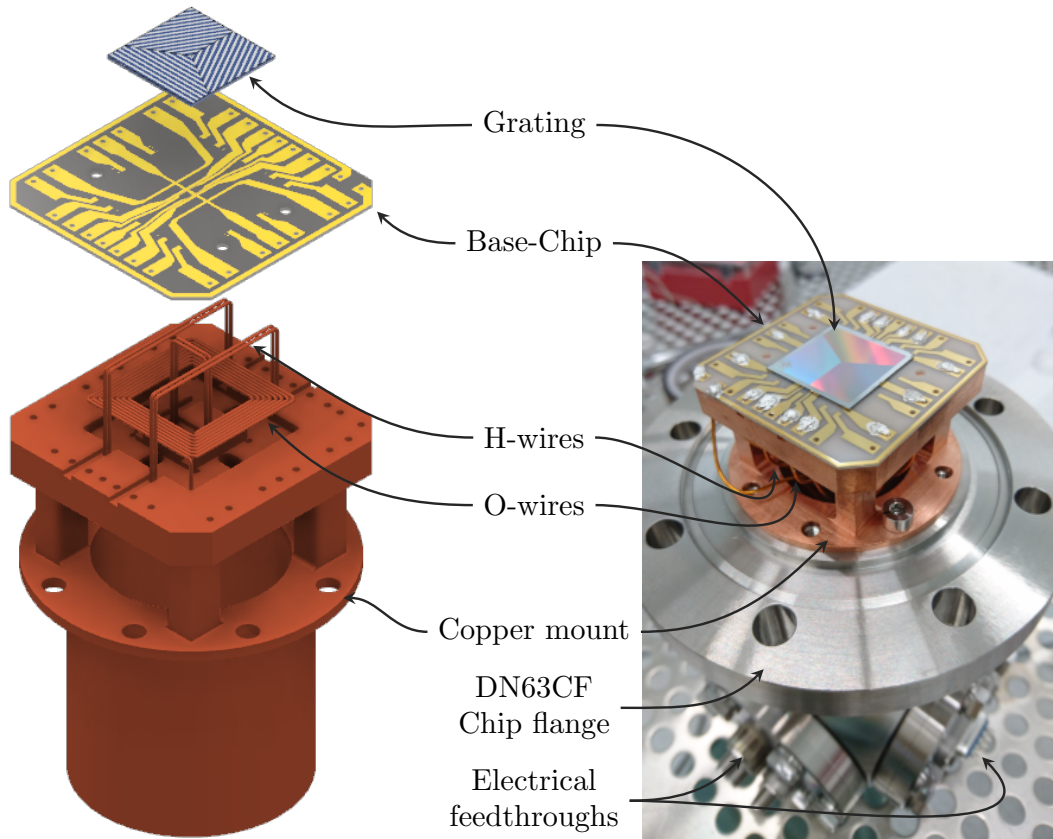
Figure 2.8: Grating atom chip in a CAD explosion view (left) and final assembly (right). Mesoscopic "H" and "O"-copper wires are placed into a copper mount which is topped with the Base-Chip. The chip is connected to vacuum feedthroughs via wires that are glued on the surface with an electrically conducting adhesive. The grating is glued on top as the final chip layer. A DN63CF chip flange accommodates the copper holder and attaches it to the vacuum chamber.

with other atom chips.

Figure 2.8 shows the CAD model and final assembly of the grating atom chip that combines a plain grating chip with the lower layers of an atom chip. A wire loop is embedded in a copper mount to generate the upright magnetic quadrupole field for the gMOT (see section 2.2.3). The loop has an inner wire separation of 15 mm with eight windings extending to an outwards wire separation of 25 mm. With a current of up to 10 A in the loop, magnetic field gradients of up to 35 G/cm can be obtained in a relevant distance of about 1 cm above the wire plane. The next layer consists of an "H"-wire structure for the initial magnetic trap (section 2.2.2) with 29 mm length for the side wires and 8 mm for the central wire. Both are wound in a loop of two wires to increase the field strength. A single atom chip layer featuring various wire structures, most notably a Z-wire, is placed on top which is identical to the model used in references [15] and [63]. A grating chip with a size of 22 mm × 22 mm and 550 µm height is placed as the final layer instead of the

second chip layer. It features a central $20\,\text{mm} \times 20\,\text{mm}$ nano-structured area with three grating regions oriented along the edges of an equilateral triangle. Each region is a 1D binary grating with a period of $d = 1080\,\text{nm}$ to diffract light with $\lambda = 780.2\,\text{nm}$ at an angle of $\theta \approx 46°$.

2.3.1 Grating Chip Assembly

The assembly of the atom chip has been carried out in the cleanroom facilities of the Laboratory of Nano and Quantum Engineering (LNQE) of Leibniz Universität Hannover. An overview of the chip assembly procedure is summarized in figure 2.9.

Before the atom chip is assembled, the chip flange needs to be prepared: First, the copper mount is inserted into the chip flange (see figure 2.8). Both parts are adapted to one another so that their insertion radii match tightly[1] which ensures good heat conductance from the chip to the outside vacuum chamber. The chip is then held in position by eight vented titanium screws. On the bottom side, a six-way DN40CF cube is attached to the chip flange which leaves space for up to five feedthrough flanges for electrical connections. After flange preparation, the actual atom chip is built.

First, the wire loop is formed from a Kapton-insulated copper wire [Allectra 311-KAP-060]. Since it is quite hard to manually shape a solid copper wire in free form with high precision, a bending aid with a detachable lid was used. The wire was first inserted from a hole in the center and the lid is attached so that the coil can be spooled radially. To get the inner bending radii tight enough, the bending is manually enhanced using pliers with three fingers. As the winding number increases, the radius in the corners also increase which is in principle fine but has to be accounted for in the magnetic field simulation (see figures 2.7 and A.1).

The loop is inserted into the copper holder with a tight fit. This provides initial mechanical stability before it is glued into position using a thermally conductive glue [EPO-TEK H77[64]] which also increases heat conduction. The straight sections of the loop are pressed into position with spacers and a large glass cube to prevent the loop from snapping out of position during the gluing process. The epoxy is then cured at a temperature of $120\,°\text{C}$ in a vacuum oven for two hours.

Next, the H-wires are placed into the chip mount and glued into position following the same procedure. Each wire section consists of two loops to enhance the effective magnetic field. The Base-Chip then encloses the mesoscopic wires with the next layer. It is glued on the flat copper areas using again a thin layer of [EPO-TEK H77[64]]. During curing, it is also pressed on the copper mount with a large glass block.

Before the grating is put on the chip, the electrical connections are established. The chip structures and the mesoscopic wires need to be connected to the electrical feedthroughs [Allectra 210-D09-C40 & 242-SMADF50-C40-3] which is implemented using Kapton-insulated stranded wires [Allectra 311-KAPM-075]. On the feedthrough side, the wires are directly

---

[1] In fact, the tolerances are so low that the parts can easily get stuck if not inserted perfectly perpendicular. This is enhanced by the fact that there is no lubrication anymore once the parts are cleaned. If that happens, the parts can be taken apart by exploiting the differential thermal expansion between Copper and Titanium. When cooled, the Copper shrinks more than the Titanium which sets the part free.
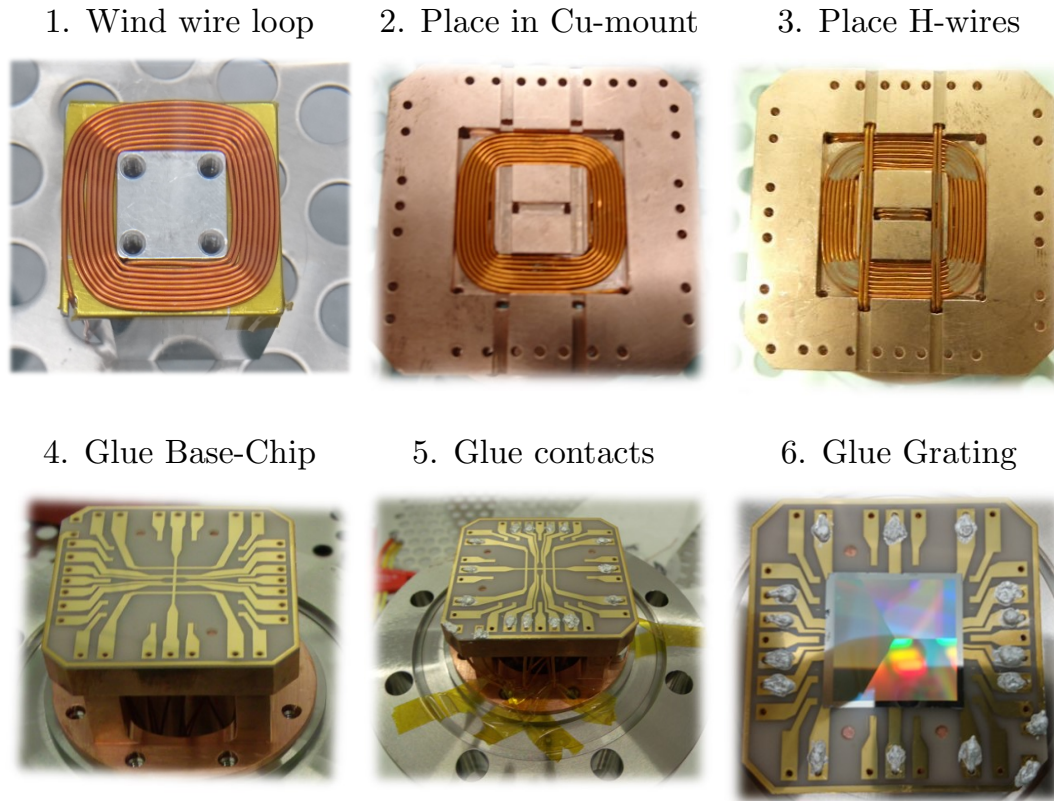
1. Wind wire loop   2. Place in Cu-mount   3. Place H-wires

4. Glue Base-Chip   5. Glue contacts   6. Glue Grating

Figure 2.9: Assembly steps of the grating atom chip in the cleanroom. 1. The wire loop is prepared using a winding aid with a detachable lid. Eight windings were wound into a planar coil. 2. The loop is placed into the copper mount. A tight fit prevents displacements but the wires are glued in position using `[EPO-TEK H77 [64]]` for increased heat conductance nevertheless. 3. Placement of the H-wires. Two loops are wound for each wire to increase the field strength. 4. The Base-Chip is glued on top using `[EPO-TEK H77[64]]` for heat conduction. 5. Stranded wires are contacted on the Base-Chip pads using an electrically conductive epoxy `[EPO-TEK H21D[65]]`. They connect to the electrical feedthroughs in the back of the chip. 6. As the last step, the grating is glued in the center of the Base-Chip using again `[EPO-TEK H77[64]]`.

attached with crimped contacts and assembled into a ceramic D-Sub connector `[Allectra 211-FS09-UHV]`. On the chip side, the wires are glued onto the pads of the Base-Chip using an electrically conducting glue `[EPO-TEK H21D[65]]` which contains silver particles to establish the electrical connection. The glue then attaches the separated strands over a broad area on the chip contact pads. It is cured for 15 min at 120 °C in a vacuum oven. Finally, the grating is glued centered on the Base-Chip using again the thermally conducting glue `[EPO-TEK H77[64]]`.

The assembled chip system was then placed into the atom chip test facility (chapter 3).
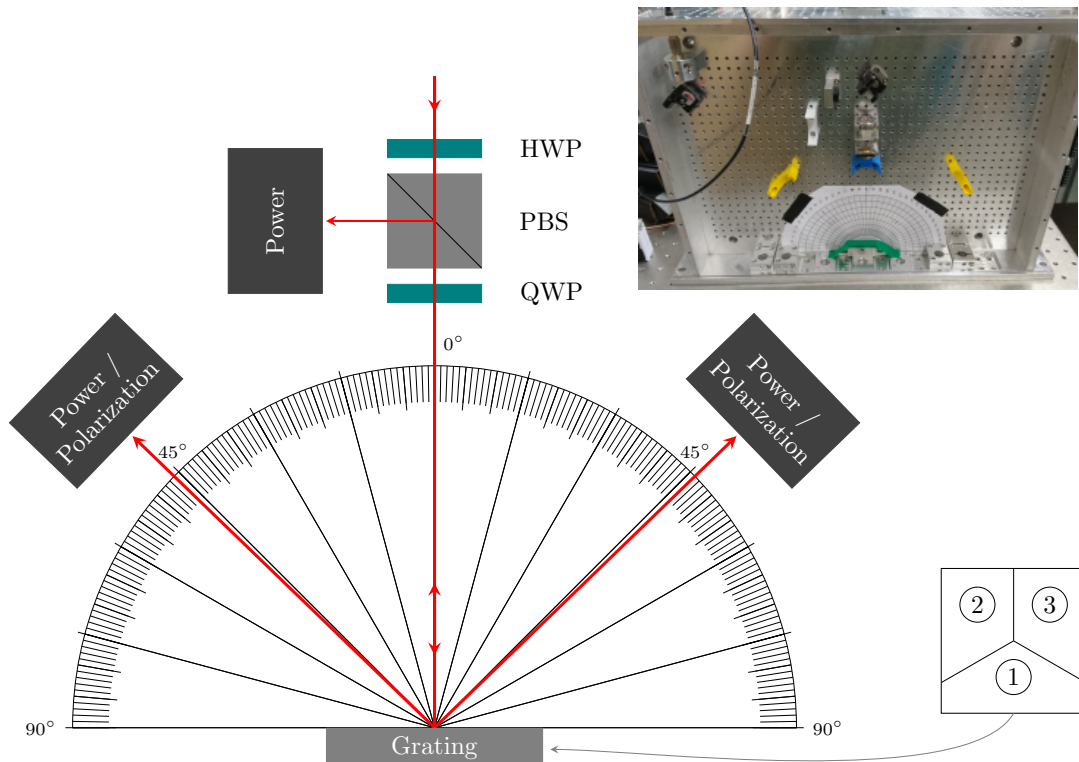
Figure 2.10: Setup for the grating characterization. Linearly polarized light is sent through a polarizing beam splitter (PBS) and adjusted in polarization by a quarter waveplate (QWP) to be circular polarized before it is normally incident on the grating region that is to be characterized. The surface of the grating is placed in the center of a polar grid so that the diffraction angle into the $\pm 1^{\text{st}}$ order can be measured. The normal incidence is verified by symmetric diffraction angles. In both diffraction orders, the power and polarization is recorded by either a powermeter or a polarization analyzer. The 0th order is retro-reflected from the grating and passes the QWP again which leads to reflection at the PBS where its power is recorded. The regions on the grating are labeled ① - ③ as depicted. The inset image shows the experimental setup in the lab.

2.3.2 Grating characterization

The triangular grating which was used for the atom chip has been kindly provided by the University of Strathclyde, Glasgow, UK [19, 57]. It was manufactured into a Silicon wafer using electron beam lithograph with a period of $d = 1080\,\text{nm}$ at an etch depth of $h \approx \lambda/4$ to suppress zero order diffraction. Afterwards the grating pattern was coated with Aluminum to yield a diffraction efficiency into the first diffraction order of $\eta_g \approx 1/3$. To verify the parameters of the implemented grating, I characterized it using the setup of figure 2.10.

A linearly polarized laser beam of $\lambda = 780.2\,\text{nm}$ with a diameter of $1\,\text{mm}$ is passed through a polarizing beam splitter (PBS) and a subsequent quarter wave plate (QWP) to change the polarization to circular. The stokes parameters characterizing the polarization state were

Table 2.1:   Results of the grating region characterization as shown in figure 2.10. The diffraction orders ± 1 have been labeled to indicate if they point in- or outwards and retro-reflection means 0th diffraction order. Ideally, the diffraction efficiency should be $\eta_g = 1/3 \approx 33.3\,\%$ for the inwards beams and the retro-reflection should vanish.

Region	Diffraction angle in °	Diffraction efficiency η_g in %		
		inwards	retro	outwards
①	46.0(5)	39.2(20)	2.4(1)	33.6(20)
②	46.0(5)	36.1(20)	2.1(1)	35.0(20)
③	46.0(5)	33.5(20)	2.2(1)	41.0(20)

recorded to be $(S_1, S_2, S_3) = (-0.036, 0.015, -0.999)$ using a commercial polarization analyzer `[Schäfter+Kirchhoff SK010PA]` which indicates nearly pure left-handed circular polarization $(S_3 = -1)$. The light is then diffracted off of the grating which is placed next to a polar grid to read off the diffraction angle. Symmetric diffraction angles indicate normal incidence of the laser beam onto the grating. The diffraction efficiency into the $\pm 1^{\text{st}}$ diffraction orders is found by measuring the diffracted power relative to the incident power. In addition to this intended diffraction, also a 0th order occurs as a back-reflection from the grating. This light passes the quarter waveplate again and is reflected at the PBS where its power is recorded. All three regions ① - ③ (see figure 2.10) of the grating have been analyzed using this method which is summarized in table 2.1. The measured diffraction angle of $\theta = (46.0 \pm 0.5)°$ corresponds to a grating period of $d = 1 * \lambda / \sin\theta \approx (1084 \pm 9)\,\text{nm}$ which fits well to the design parameters. While the diffraction angle is identical for all regions within the measurement uncertainty, the diffraction efficiency changes within a few percent between the grating regions. This may result in slight light imbalances in the final application. Furthermore, it is worth noting that the total power is not preserved as about 25 % of the light is lost. Though this has been already factored into the design which brings the diffraction efficiency close to the desired $\eta_g = 1/3$ in accordance to the considerations of section 2.1.1.

In general, gratings are known to significantly alter the polarization of light. Surprisingly, the light polarization after diffraction was found to be $S_3 \approx +0.97$ for all regions which indicates nearly perfect inversion of the handedness as it would be expected by the reflection from a metallic mirror.

2.4 Capture from an atomic beam

Grating MOTs are easy to use but it can be quite challenging to understand them intuitively as traditional 1D-considerations do not grasp the full beam configuration. Most of the time, they have been used to capture atoms from a background gas using external quadrupole coils which provide their field in a large spatial volume. With the magnetic fields generated by the atom chip and the intended capture from an atomic beam, things get even more complicated so it is worthwhile to study the grating atom chip assembly in a computer simulation. This section seeks to describe the forces in the gMOT and consider them in the context of atom chip magnetic fields to study the capture of atoms from an atomic beam.

2.4.1 Light forces in a gMOT

The forces in a magneto-optical trap are caused by atom-light interaction. Whenever a photon is absorbed from the light field, it excites the atom and imparts a directed momentum kick $\vec{p} = \hbar \vec{k}$ where $\hbar$ is the reduced Planck constant and $\vec{k}$ is the wave vector of the light. From this exited state it will decay back into the ground state either through spontaneous or stimulated emission. For stimulated emission into the same light field, the total momentum of the atom does not change at all. For spontaneous emission, a photon is emitted in a random direction applying an additional kick. Since this emission has no preferred spatial direction, the overall contribution averages out and the total momentum is directed along the lights' k-vector. The force can be understood best in a simple $F = 0 \rightarrow F' = 1$ system where light may drive transitions into the $m_{F'} = -1, 0, +1$ manifold with relative strengths $\alpha_{m_{F'}}$. It can be calculated by considering the rate of the applied momentum kicks

$$\vec{F} = \hbar \vec{k} R_{\text{sc}} \tag{2.8}$$

with the scattering rate

$$R_{\text{sc}} = \frac{\Gamma}{2} \frac{I/I_{\text{sat}}}{1 + I_{\text{tot}}/I_{\text{sat}} + 4\frac{\delta^2}{\Gamma^2}}, \tag{2.9}$$

where Γ is the natural linewidth of the transition, I/I_{sat} is the relative intensity with respect to the saturation intensity I_{sat}, $I_{\text{tot}} = \sum_j I_j$ is the total intensity, and $\delta = \omega - \omega_0$ is the light detuning of the laser frequency ω to the atomic transition ω_0. The force becomes velocity- and space dependent through the detuning: For an atom moving at velocity $\vec{v}$, the light frequency appears shifted by $\delta_v = \vec{k} \cdot \vec{v}$ due to the Doppler effect. Furthermore, if the atom is located in a magnetic field $\vec{B}(\vec{r})$, its energy levels are modified by the Zeeman effect

$$\Delta E(\vec{r}) = \mu_{\text{B}} g_F m_F |\vec{B}(\vec{r})| \tag{2.10}$$

where ΔE is the change in energy, μ_{B} is the Bohr magneton, g_F is the gyromagnetic ratio, and m_F is the magnetic substate. This detunes the optical transition by

$$\delta_Z(\vec{r}) = \frac{\mu_{\text{B}}}{\hbar} g_F \Delta m_F |\vec{B}(\vec{r})| \tag{2.11}$$

where Δm_F indicates the respective change between the states. Traditional laser cooling in a 6-beam MOT uses circular polarized light to drive transitions with $\Delta m_F = \pm 1$ for atoms in a quadrupole magnetic field

$$\vec{B}(x,y,z) = b' * (x\hat{e}_x + y\hat{e}_y - 2z\hat{e}_z) \tag{2.12}$$

where b' is the gradient of the field and $(\hat{e}_x, \hat{e}_y, \hat{e}_z)$ are the unity vectors of the cartesian coordinates. The 6 beams are aligned pairwise counter-propagating along the same axes with $\hat{\vec{k}} \parallel \hat{\vec{B}}$ so that π transitions with $\Delta m_F = 0$ are suppressed [61]. This provides a

restoring force towards the trap center if the polarization of the light is chosen correctly with respect to the magnetic field direction. The intensity in equation 2.9 therefore consists purely of contributions from circular polarized light $I = I_{\pm 1}$ where the index indicates Δm_F. The gMOT breaks this symmetry as $\hat{\vec{k}} \nparallel \hat{\vec{B}}$ for the diffracted beams. While the incoming beam is aligned along $\hat{e}_z$ as in the 6-beam MOT, the diffracted beams with wave vector $\vec{k}_j$ enclose an angle ϕ with the local magnetic field

$$\cos(\phi(\vec{r})) = \vec{k}_j \cdot \vec{B}(\vec{r}) \tag{2.13}$$

which may spatially vary[1] depending on the position of the atom in the magnetic field. After diffraction, the beams mostly retain their circularity but with inverted sign (i.e. left handed circular polarization becomes right handed and vice versa, see section 2.3.2). The atom, however, will perceive this light field not as purely circular polarized as it needs to be projected onto the local magnetic field axis leading to linear polarization contributions. Therefore, the diffracted light beams may also drive π transitions with $\Delta m_F = 0$. The force equation for a single beam j is then extended by summing over all polarization contributions as

$$\vec{F}_j(\vec{r},\vec{v}) = \hbar \vec{k}_j \frac{\Gamma}{2} \frac{I_j}{I_{\text{sat}}} \sum_{m_F = -1,0,+1} \frac{\alpha_{m_F}}{1 + I_{\text{tot}}/I_{\text{sat}} + \frac{4}{\Gamma^2}(\delta_0 - \vec{k}_j \vec{v} - \frac{\mu_{\text{B}} g_F}{\hbar} m_F |\vec{B}(\vec{r})|)^2}, \tag{2.14}$$

where α_{m_F} is the relative coupling strength for the respective transition. The strength is found by working out the relative intensities in the light beam driving σ_-, π and σ_+ transitions after the electric field polarization vector has been projected onto the magnetic field axis (see appendix A.1):

$$\alpha_{-1} = \frac{1 + \cos^2 \phi - 2 \sin \xi \cos \phi}{4} \tag{2.15}$$

$$\alpha_0 = \frac{1}{2} \sin^2 \phi \tag{2.16}$$

$$\alpha_{+1} = \frac{1 + \cos^2 \phi + 2 \sin \xi \cos \phi}{4}. \tag{2.17}$$

Here, ξ is the retardance between the perpendicular electric field components which determines the polarization. For circular polarization ($\xi = \pm \frac{\pi}{2}$) these can be written in the

---

1   Strictly speaking, this also occurs in traditional 6-beam MOTs at off-axis positions in the magnetic field [66]. This case is rarely discussed in the literature which often only considers the magneto-optical forces in 1D on axis.

simplified form

$$\alpha_{-1} = \left(\frac{1 \mp \cos\phi}{2}\right)^2 \tag{2.18}$$

$$\alpha_0 = \frac{1}{2}\left(\sin\phi\right)^2 \tag{2.19}$$

$$\alpha_{+1} = \left(\frac{1 \pm \cos\phi}{2}\right)^2. \tag{2.20}$$

Note, that $\sum_{m_F} \alpha_{m_F} = 1$ and for $\phi = 0$ (i.e. $\vec{k} \parallel \vec{B}$), $\alpha_0 = 0$ as well as $\alpha_{\pm 1} = 1$ is retained for each respective polarization.

This quite complex description of the gMOT allows to calculate the forces in a general manner but is not very intuitive. For small detunings $\delta_v, \delta_Z \ll \Gamma$, equation 2.14 may be approximated using a Taylor expansion

$$\vec{F}_j(\vec{r},\vec{v}) \approx \hbar\vec{k}_j \frac{\Gamma}{2}\frac{I_j}{I_{\text{sat}}} \sum_{m_F=-1,0,+1} \alpha_{m_F}\left(K + C\left(\vec{k}_j\vec{v} + \frac{\mu_{\text{B}}g_F}{\hbar}m_F|\vec{B}(\vec{r})|\right)\right) \tag{2.21}$$

where

$$K = \frac{1}{1 + I_{\text{tot}}/I_{\text{sat}} + 4\frac{\delta_0^2}{\Gamma^2}} \tag{2.22}$$

$$C = \frac{8\delta_0}{\Gamma^2}K^2 \tag{2.23}$$

are constants in a given system and the force becomes linear in $\vec{v}$ and $\vec{r}$ for a quadrupole magnetic field. Note, that this condition is often not satisfied as atoms emerging from e.g. an atomic beam have velocities of a few m/s (see section 3.3.2). For example, the Doppler detuning of a Rb atom moving with $15\,\text{m/s}$ is about $\delta_v \approx 2\pi \cdot 19.2\,\text{MHz}$ which is well *above* the natural linewidth $\Gamma \approx 2\pi \cdot 6\,\text{MHz}$.

2.4.2 Simulation: Trapping from an atomic beam

Even in the case of the linear approximation, the force equations for the gMOT are quite lengthy and hard to grasp. From the bare equations, one needs to always consider the local projections between light and magnetic field to determine the strength of the force components. Therefore, a computer simulation can help to gain some understanding and intuition of the cooling and trapping force in the gMOT.

With the force equation 2.14 from each beam at hand, one can study the total force in the gMOT by summing over all force contributions

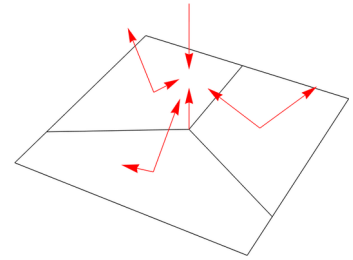$$\vec{F}(\vec{r},\vec{v}) = \sum_j \vec{F}_j(\vec{r},\vec{v}) \tag{2.24}$$

Fig. 2.11: Illustration of wave vectors in the gMOT shifted to their respective grating region. Not drawn to scale.
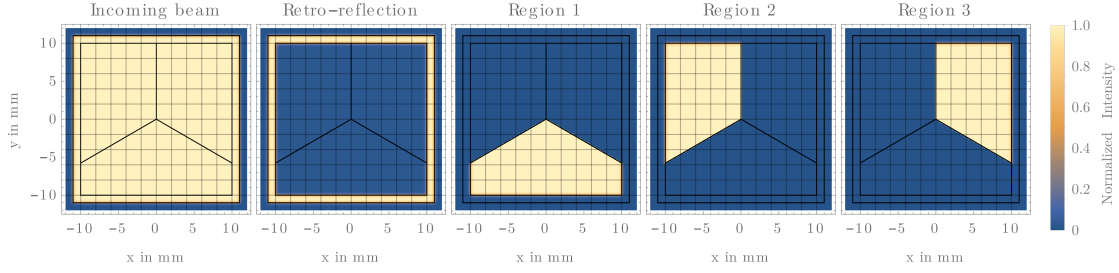
Figure 2.12: Plot of the modeled intensity distributions for the separate grating regions associated with different k-vectors. While the incoming beam is modeled to illuminate the full grating with constant intensity, the retro-reflection is relevant in the reflective ring outside the grating-area and the zero-order reflectivity. The three grating regions $1-3$ are a cut-out of the incoming beam profile with respect to the corresponding wave vectors. Each area is rolled off towards zero on all edges with a steep sigmoid function for differentiability of the intensity distribution which is required for solving the differential equations numerically.

from each beam j. One can then treat the total force classically and solve the equations of motion

$$\ddot{\vec{r}}(t) = \vec{F}\left(\vec{r}(t),\dot{\vec{r}}(t)\right)/m \tag{2.25}$$

with the boundary conditions

$$\vec{r}(0) = \vec{r}_0 \tag{2.26}$$
$$\dot{\vec{r}}(0) = \vec{v}_0 \tag{2.27}$$

of an atom at some position $\vec{r}_0$ with velocity $\vec{v}_0$. To determine the force, one needs to calculate the local magnetic field $\vec{B}(\vec{r})$ from a suitable model and find the respective intensities for each wave vector. For the magnetic field, one can simply use a quadrupole magnetic field as in equation 2.12 or model the field more extensively. Although the calculations take significantly longer, an atom chip magnetic field simulation was used in this work for a more realistic representation of the field. The wave vectors are determined from spherical coordinates

$$\vec{k}_n = \frac{2\pi}{\lambda} \begin{pmatrix} \sin\theta_m \cos\Phi_n \\ \sin\theta_m \sin\Phi_n \\ \cos\theta_m \end{pmatrix} \tag{2.28}$$

where θ_m is the signed diffraction angle with order m and $\Phi_n = 0°, 120°, 240°$ to match the vector with the respective grating area and diffraction order. For the incoming and retro-reflected beam, $\vec{k} = \frac{2\pi}{\lambda}(0,0,\mp 1)$ respectively. The total set of eight wave vectors is illustrated in figure 2.11 for clarity.

For the intensities, one has to be careful as they are *not* determined locally but rather by looking back from where the beams originated from on the grating. The source position

on the grating is found by tracing back to the plane of the grating along each respective k-vector (see section 2.1.1). At this point, the illumination profile of the grating is evaluated to find the local intensity. To ensure that each k-vector only acts from its respective grating region in the simulation, the intensity distribution is modeled separately for each k-vector according to figure 2.12. Each profile is a spatial cut-out of the overall intensity illumination from the incoming beam that could be chosen freely but is assumed to be constant in the following. The cut-outs are only non-zero for the respective grating region where the wave vector acts from. On the edges of each region, the intensity distribution is rolled off towards zero using a steep sigmoid function

$$f(\kappa,x) \propto \frac{1}{1 + \mathrm{e}^{-\kappa x}} \tag{2.29}$$

for differentiability of the intensity distribution where κ determines the steepness of the edge and is chosen to be large. This way, every beam is effectively modeled as an individual virtual source with unique profile. From these considerations, the total force on an atom can be calculated in the full volume above the grating. Solving the equations of motion numerically, the trajectory $\vec{r}(t)$ of an atom in the force field is found for initial conditions $\vec{r}_0, \vec{v}_0$. This can be used to model the capture from an atomic beam that enters the grating region from the outside as it is the case for the 2D$^+$-MOT.

Figure 2.13 shows the trajectory of an atom entering the atom chip region from the outside along a diagonal for various velocity cases. As the atom approaches the grating, it interacts first with an outwards diffracted beam. If the atom is too slow, it will already be pushed away before it even reaches the grating region. Faster atoms do reach the first grating region, where they are further cooled. In the beginning, they only interact with light from the top (illumination beam) and the front (outside diffraction order) which causes a drop in height as the top beam is much stronger than a single diffracted beam by design. Once they reach in a bit further due to their initial velocity, also the inwards diffracted beam from the outside grating region interacts with the atoms so that two light beams counteract the incoming beam. This may support the atom long enough to reach the central region where the spatial force contribution gets stronger and the atom swirls towards the final trapping position from below. Here, the velocity also goes towards zero as it is to be expected for the MOT configuration. It is worth noting that the final position is actually *above* the position of the magnetic field minimum which is indicated by the red dot. This is caused by magnetically-insensitive $\pi-$transitions that stem from the projection of light polarization onto the local magnetic field orientation. Velocities between $12 - 18\,\mathrm{m/s}$ are captured for the parameters in this simulation. Faster atoms are not stopped within the grating region and travel through without being captured.

The lesson learned from this simulation is that the outwards diffracted beam plays a crucial role in pre-slowing the atoms. While slow atoms are rejected by this, atoms at higher velocities typical for the 2D$^+$-MOT (see section 3.3.2) are well accepted due to the initial pre-slowing interactions. Tailoring the atomic source towards this acceptance band will therefore be beneficial for a high capture efficiency though this velocity range seems to work very well already.

Furthermore, it is worth noting that the initial drop in height due to light imbalances may be alleviated by increasing the height of the atomic beam with respect to the grating surface which is planned in the future.
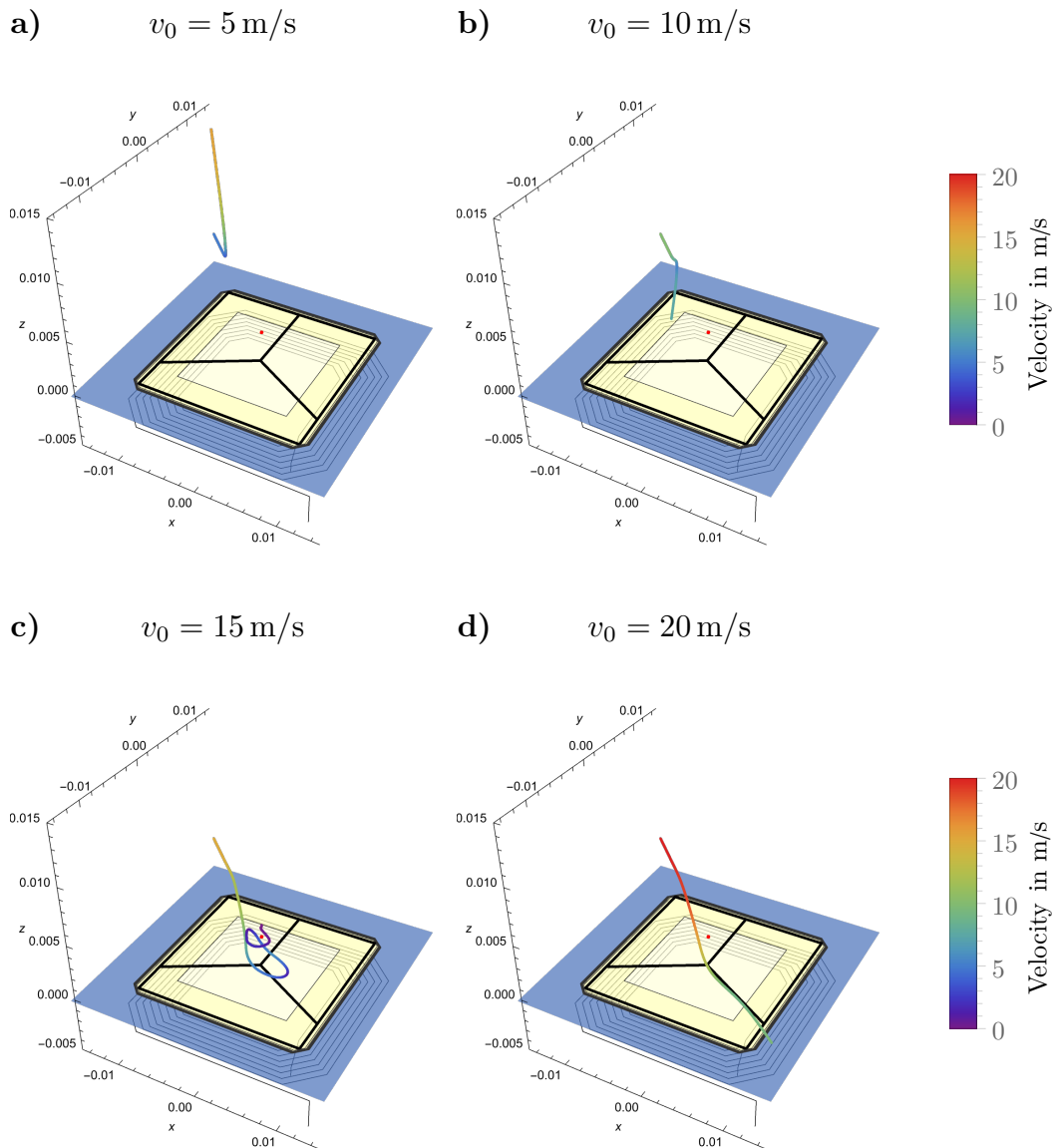
a) $v_0 = 5\,\text{m/s}$ **b)** $v_0 = 10\,\text{m/s}$

c) $v_0 = 15\,\text{m/s}$ **d)** $v_0 = 20\,\text{m/s}$

Figure 2.13: Numerical simulation of the gMOT capturing from an atomic beam of ^{87}Rb for various velocity cases. The trajectory $\vec{r}(t)$ solving the equations of motion is shown with the color indicating the local velocity. **a)** As the atom approaches the grating, it interacts with one of the outwards diffracted beams which expels atoms with insufficient velocities. **b)** On the way to the center, the atom is pushed downwards due to the local intensity imbalance from the stronger top beam which is unable to be balanced by two diffracted beams from below. **c)** If the atom was fast enough, it reaches the center, where the spatial force contribution dominates and the trajectory swirls towards the final position from the bottom which sits above the magnetic field minimum (red dot). This way, atoms with velocities of $12-18\,\text{m/s}$ are captured. **d)** Faster atoms are not stopped within the grating region and travel right through. The simulation uses $I/I_\text{sat} = 1.3$, $\delta_0 = -1.5\,\Gamma$ and $(\partial_z \vec{B})_z = 29.9\,\text{G/cm}$.

CHAPTER 3

A versatile Test Environment for Atom Chips

Atom chips have played a major role in shrinking BEC machines from lab-sized room-filling setups to transportable realizations that allow to conduct experiments in demanding environments. This enabled to perform experiments with BECs on microgravity platforms like the droptower in Bremen [14], on a sounding rocket in space [15] and also on the International Space Station (ISS) [67]. Despite their success, the atom chip technology has not fully matured since the tight schedule of these missions did not allow for significant technological advancement on the core technology itself. Therefore, an effort was made in the scope of this thesis to plan, set up, and conduct experiments with a dedicated test facility for atom chips.

In general, cold atom experiments are performed with lasers in a vacuum system exploiting electromagnetic fields to manipulate the energy levels of the atoms. Therefore, a multitude of equipment is required for the test facility:

- The **vacuum system** provides the environment in which the experiments are conducted. It consists of the main science chamber which houses the atom chip, a source chamber that provides a beam of cold atoms from which the chip trap is loaded and a tubing system that connects to vacuum pumps. The pressure needs to be in the ultra-high vacuum (UHV) range and is typically at 3×10^{-11} mbar in this setup.

- The **laser system** provides the optical light fields to manipulate the atoms. External Cavity Diode Lasers (ECDLs) are offset-locked in frequency to a transition in Rubidium. Their light is guided through an amplification module where the power is amplified and redistributed among different paths according to various tasks in the experiment. The system can generate light pulses using acousto-optical modulators (AOMs) and also features mechanical shutters to block the light completely.

- The **electronics system** takes care of the precisely timed control of experimental parameters. It controls the lasers, provides the currents to generate magnetic fields, and acquires data of the experimental run. A Field Programmable Gate Array (FPGA) helps to control various parts of the experimental periphery. It largely consist of components developed for micro-gravity experiments of the group which ensures transferability of results.

The following sections describe the components of the test facility in more detail.

3.1 Vacuum system

The vacuum system for a cold atom experiment is like the laboratory for any other physics experiment: It defines the surrounding environment in which experiments are conducted and may influence the experimental outcome by its properties. Having a good vacuum system is thus of the utmost importance for any cold atom experiment. This includes not only a low vacuum pressure to minimize background gas collisions but also the requirement to be non-magnetic as to not disturb the magnetic environment. Consequently, it is manufactured from Titanium which features not only excellent magnetic properties but also low outgassing rates [68]. In addition, the design must be flexible enough to allow for different kinds of atom chips to be tested, e.g. with a grating or a mirror-MOT, and it must do so under different orientations. It needs to be small enough so that the surrounding coils are still able to deliver reasonable magnetic field strengths without water cooling but at the same time be big enough to offer sufficient optical access. All in all, the design space is quite restricted and trade-offs have to be made.

The solution of this work is depicted in figure 3.1 and features two separate vacuum chambers: The science chamber housing the atom chip and the 2D$^+$-MOT as the atomic source. Both of them are connected with a differential pumping stage dividing them into two regions of different vacuum pressure. The atom chip is placed into a separate chip mount which is then attached to the science chamber. For atom chip replacement, a second chip mount can be conveniently prepared externally so that they can be quickly exchanged without exposing the vacuum system to air for a long time. The interconnection between these components is based on commonly used copper gasket metal seals following the CF standard which is usable down to the UHV region. For the optical access though, standard CF viewports have proven to be inefficient in terms of space usage and therefore indium-sealed windows are pressed into the science and source chamber. They offer superior surface and coating qualities at a reduced footprint size. This is comes with the downside that heating of the vacuum system is limited to well below the Indium melting temperature, typically not exceeding 100 °C. However, the small footprint allows optical access to be placed on various faces of the vacuum chamber allowing for different MOT configurations, i.e. 45°-access for a mirror-MOT and opposite access for a grating-MOT.

Mounting of the science chamber towards the vacuum pumps can be done flexibly on any of the three CF interconnects, i.e. 2x CF16 and 1x CF40. This way, the atom chip can be set up in three different orientations: vertically, at 45°, or horizontally with respect to the ground.

The chamber is pumped through a CF63 tubing system with a 60 l/s Ion Pump `[Gamma Vacuum TiTanIon Pump 75S]` and a Titanium Sublimation Pump `[Gamma Vacuum Titanium Sublimation Pump Filament Catridge CF40]`. Together they allow to pump the vacuum system to a pressure of 3×10^{-11} mbar reaching well into the ultra-high vacuum (UHV) regime.
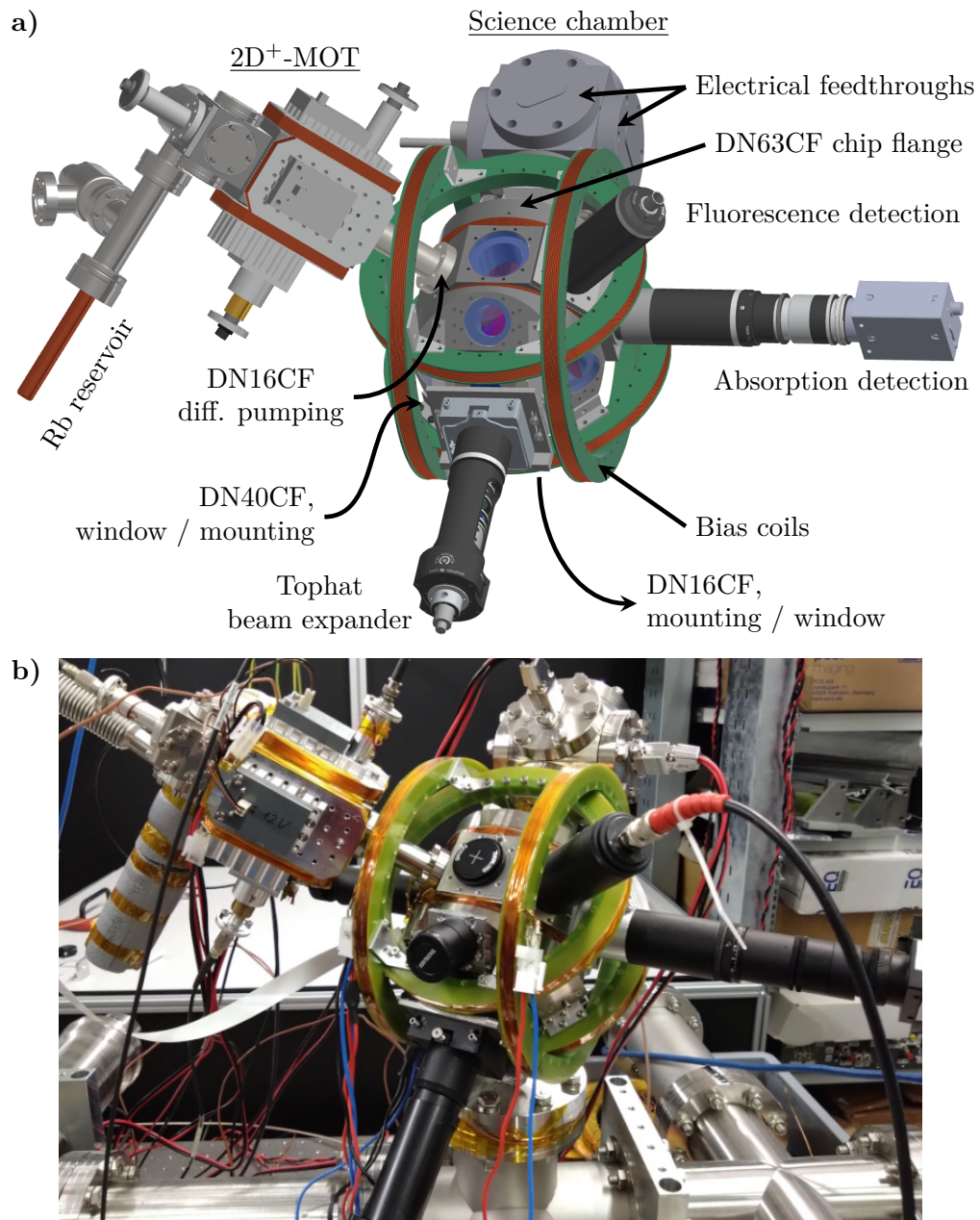
Figure 3.1: Overview of the vacuum system and its surrounding components. **a)** CAD drawing of the Double-MOT system in a 45° mounting configuration for the usage with a grating-chip. Cold atoms are loaded from the 2D$^+$-MOT source chamber into the science chamber through a differential pumping stage. While the sealing between the chambers is realized using standard CF metal gaskets, optical access is implemented via indium-sealed coated glass substrates. The atom chip is placed in the Science chamber with a DN63CF chip flange that features electrical feedthroughs in the back. For atom chip exchange, an additional chip flange is available on which the second chip may be prepared so that the exchange can be carried out quickly. One of the three bias coils is already implemented in a recess of the science chamber. **b)** Photograph of the built system.

3.2 Bias coils

The operation of the atom chip requires not only the chip fields but also external homogeneous bias fields. These are commonly generated by pairs of Helmholtz coils where the coil radius is equal to the distance between the coils. When an equal parallel current is sent through the coils, the resulting field is very homogeneous in the center which is where the atom chip should be placed. In terms of field strength, the coils need to be strong enough to compete with the generated chip fields which is highly relevant for the generation of tight magnetic traps. These are achieved only in the close vicinity of the chip wires so that a strong field needs to be applied to move the trap minimum close-by. In addition, the bias coils are also required to compensate external magnetic fields for sub-Doppler cooling where any residual field hampers the cooling efficiency and limits the achievable temperature.

The field strength in the center of a Helmholtz-coil is calculated by [69]

$$B = \frac{8\mu_0}{\sqrt{125}} \frac{IN_w}{a} \tag{3.1}$$

where I is the current through the coils, N_w is the winding number, a is the radius and $\mu_0 \approx 1.257 \times 10^{-6}\,\mathrm{N/A^2}$ is the permeability of free space. Since the maximum current[1] in the coil will be limited to $5\,\mathrm{A}$ [16], the radius should be kept as small as possible to maximized the field. The design parameters of the bias coils are therefore tightly connected to the size of the vacuum chamber as three independent Helmholtz-coils need to be fitted around it. This constraint has already been included in the design considerations of the vacuum chamber so that one coil pair is already wound into a recess of the wall (see figure 3.1) which creates the field in Z-direction (perpendicular to the chip surface). The coil radius is $a_z = 54\,\mathrm{mm}$ with a total of 34 windings. The other two Helmholtz-coils are placed around the chamber on fiber-reinforced plastic holders which allow them to be baked as well.

The strongest magnetic field needs to be applied in Y-direction to complement the atom chip. Therefore, the inner coil holder is tightly fitted around the vacuum chamber with a circular coil of $a_y = 84\,\mathrm{mm}$ radius which denotes the center of the winding cross-section that is $(10 \times 10)\,\mathrm{mm^2}$. Much weaker fields are required in X-direction for the magnetic trap bottom field, absorption detection and external field compensation. Here, the coil radius is $a_x = 98\,\mathrm{mm}$ on the outer coils.

The switching times of the coils will be restricted by the coil inductance that is determined by the winding number. A good balance between winding number and operation current should be used to minimize switching times but allow for sufficient magnetic field to be applied. Therefore, both coil holders are fitted with two sub-coils that can be connected externally into either the full coil or one of the two sub-coils. Within each holder, a total of 85 windings are wound with a $1.1\,\mathrm{mm}$ thick insulated copper cable. The wire layers alternate between 9 and 8 wires per layer where the wires lay in the gap between the two wires of the previous layer for highest packing density. The first sub-coil is wound with

---

1   The maximum current is only achieved if the available voltage is high enough for the respective load.

four layers with $2 \times 9 + 2 \times 8 = 34$ windings and the second coil features $3 \times 9 + 3 \times 8 = 51$ windings. While the full winding number is used in Y-direction to maximize the field, the X-direction only uses the smallest inner coil. The magnetic field generated by the coils was estimated in a computer simulation (see appendix A.3) and verified by RF spectroscopy (see section 4.8). The results are summarized in table 4.1.

3.3 Atomic Source

In principle, there are two kinds of atomic source concepts that can be followed: capturing atoms from a background gas or from a pre-cooled atomic beam. When loading from a background gas, the atom chip would be immersed in a gas of the atomic species that is to be trapped. A high background pressure of the gas benefits MOT loading as more atoms are available per volume. However, the atom chip seeks to trap atoms magnetically. Since the trap depth of the magnetic chip trap is only on the order of a few hundred µK, background gas collisions may transfer enough kinetic energy to an atom to escape the trap. Therefore, the background pressure needs to be kept sufficiently low such that background collisions do not dominate. This, in turn, extends MOT loading times because fewer atoms are available to gather from, and it prevents a high-flux of ultracold atoms.

The solution to circumvent this issue is to separate the final trapping region from the atomic source and capture from an atomic beam. The beam is formed in a separate vacuum chamber with high partial pressure and funneled through a differential pumping stage to reach the trapping region. This way, the pressure in the atom chip chamber can be kept low to minimize background collision losses. This approach is often referred to as a Double-MOT system with a $2D^{(+)}$-MOT. It has been successfully implemented in other atom chip devices (e.g. [14, 15, 63]) and is thus also utilized here.

3.3.1 Source Concept

The concept follows closely the $2D^{+}$-MOT design of [40] as successfully implemented in [14, 15, 63] with only minor modifications (see figure 3.2). Briefly, four coils are assembled around the vacuum chamber in racetrack configuration. When a current is sent through the coils such that it matches in direction for neighboring coil segments, a radial quadrupole field is generated along the central axis of the vacuum chamber. Due to the geometry of the coils, the field vanishes along the axial direction. Two circular cooling regions generated by two retro-reflected transversal cooling beams gather atoms from the background gas into a standard 2D-MOT. A counter-propagating set of pusher and retarder beams provides additional laser cooling along the axial direction, enhancing the setup to a so-called $2D^{+}$-MOT. Since the retarding beam is reflected from the polished 45° surface of the differential pumping stage, a shadow of the hole is left in the reflected beam. This provides an escape channel into the main vacuum chamber. By adjusting the power and power ratio of the pushing and retarding beams, the properties of the atomic beam can be manipulated. These parameters have been studied and are presented in the following section.
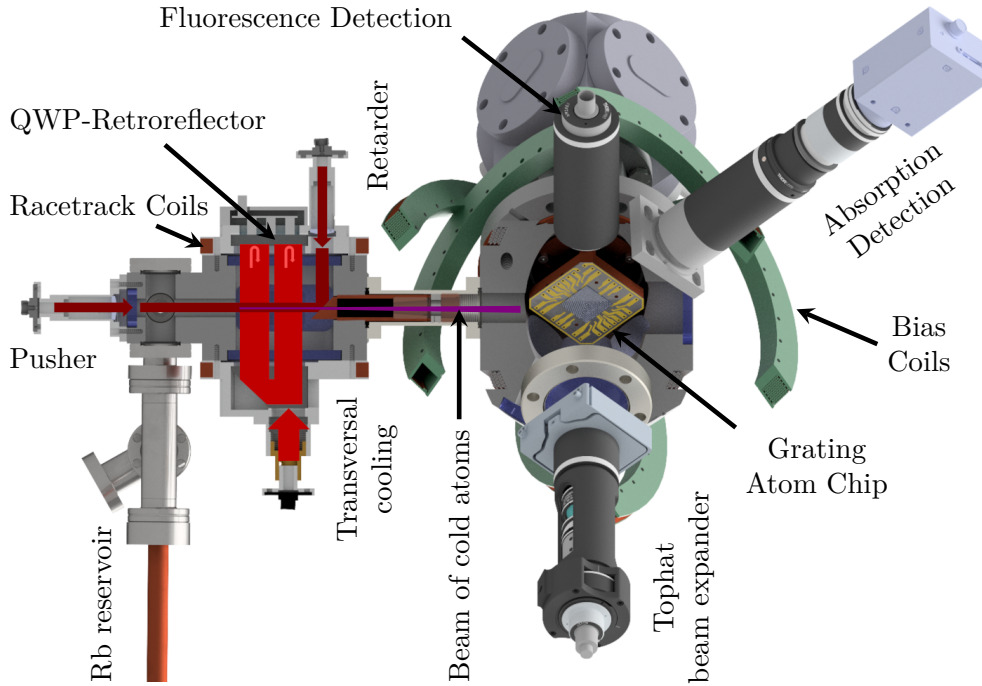
Figure 3.2: Sectional view through the 2D$^+$-MOT vacuum chamber. A standard 2D-MOT is generated by two transversal cooling beams next to each other that are retroreflected passing through a quarter waveplate (QWP) twice. The magnetic field is generated by four coils around the vacuum chamber in racetrack configuration generating a radial magnetic quadrupole field. The geometry is enhanced to a 2D$^+$-MOT by a set of counter-propagating pusher and retarder beams that traverse along the axial direction. The retarding beam is reflected from the 45° surface of the differential pumping stage leaving a shadow from the central hole. This provides an escape channel towards the main chamber to load the chip MOT. By adjusting the power and power ratios of the pushing and retarding beam, the properties of the beam of cold atoms can be adjusted.

3.3.2 Source Characterization

An atomic source is not only characterized by its number of atoms per second (i.e. the flux) but also by its velocity distribution. Typically, the highest possible flux is desired in the atomic source so that more atoms are trapped in shorter amounts of time. However, the 3D-MOT will only have a finite range of capture velocities which is notoriously low for atom chip MOTs due to their small beam diameters and small quadrupole extent. In particular, this gets even worse for the grating MOT (see section 2.4). It is therefore critical to engineer the output velocity distribution of the atomic source towards the capture range of the 3D-MOT.

The 2D$^+$-MOT has been characterized following the procedure described in [40]. Briefly, the beam of cold atoms is sent through the differential pumping stage to reach the science chamber. Here, a perpendicular probe beam shines in light that is scattered by the atomic beam isotropically. Parts of the scattered light are picked up by a photodiode from which

the flux can be calculated as atom number per unit time. The calculation is very similar to the atom number determination of section 3.5.1 but with the addition that the interaction time $d/\langle v_l \rangle$ of atoms with a mean longitudinal velocity $\langle v_l \rangle$ over the light interaction width d is taken into account:

$$\Phi = \frac{U_{\mathrm{PD}}}{G \cdot S \cdot \frac{\mathrm{d}\Omega}{4\pi} \cdot R_{\mathrm{sc}} \cdot h\nu} \frac{\langle v_l \rangle}{d}, \quad [\Phi] = \mathrm{atoms/s}. \tag{3.2}$$

The only unknown variable here is the mean forward velocity $\langle v_l \rangle$ of the atomic beam which has to be determined in a separate measurement:

By probing the atomic beam under an angle θ in a retro-reflection configuration, the atomic velocity is projected on the probe beam and a Doppler-shift

$$2\pi\Delta\nu = k \langle v_l \rangle \cos\theta \tag{3.3}$$

occurs. When the frequency of the probe beam is scanned, it becomes resonant once with the incoming beam and once with the retro-reflected beam as the Doppler shift acts in different directions. This way, the velocity distribution is mapped on the fluorescence signal as a double-peak signal where the distance between the peaks accounts for twice the Doppler shift so that the velocity is calculated as

$$\langle v_l \rangle = \frac{\pi\Delta\nu}{k\cos\theta}, \tag{3.4}$$

where $\theta = 45°$ was used in the following measurements. Probing the beam under $\theta = 90°$ then allows to determine the peak signal U_{PD} from which the flux can be calculated using equation 3.2. The far off-resonant photodiode voltage is taken as the reference level.

The forward velocity and flux may depend on multiple parameters of the 2D$^+$-MOT such as gradient, detuning, and in particular also the power(ratio) of the pushing and retarding beams. Previous experimental investigations [62, 70] have shown that the optimum magnetic field gradient of such a 2D$^+$-MOT is around 20 G/cm. However, due to technical limitations, the maximum available magnetic field gradient in this setup is only 16.2 G/cm which is used in the following. In a first step, the detuning is optimized for a fixed pusher power of 4.38 mW (intensity: 9.95 mW/cm^2) and then the pusher dependency is investigated.

Dependency on the detuning

Figure 3.3 shows the outlined measurement for different detunings $\delta_{2\mathrm{D}}$ of the cooling light in the 2D$^+$-MOT. The probe beam has a diameter of $d = 1.2$ cm and a power of 1.07 mW resulting in an intensity of 0.95 mW/cm^2. The light frequency of the probe beam is ramped linearly over a duration of 1 s to probe a range of ± 50 MHz around the calculated resonance of the ^{87}Rb D_2 cooling transition. A photodiode records the fluorescence signal perpendicular to the probe beam. For every detuning value, the velocity distribution is measured in the 45° retro-reflection setup and the Doppler shift is determined (see figure 3.3a). Afterwards, the flux is determined from the data of the 90° setup (figure 3.3b). It was found, that the forward velocity decreases with higher detunings and starting
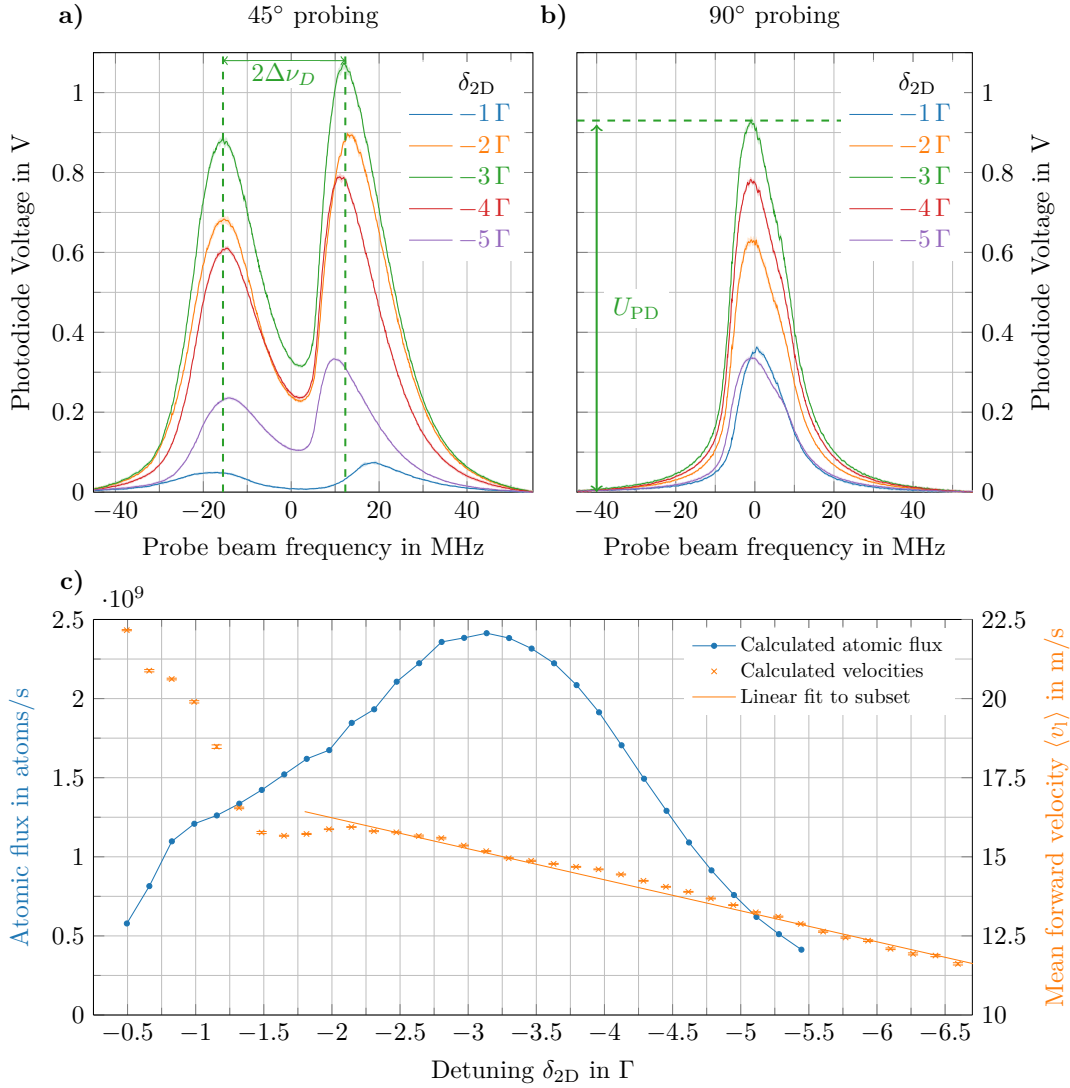
Figure 3.3: Mean longitudinal velocity and flux of the $2D^+$-MOT depending on the detuning. The beam of cold atoms is sent into the main chamber where it interacts with a probe beam which is scanned around the ^{87}Rb D_2 cooling transition frequency to become resonant with different velocity classes. A perpendicular photodiode picks up the fluorescence signal. The top figures show exemplary offset-subtracted fluorescence curves for different detunings δ_{2D} in the $2D^+$-MOT where each curve was averaged over 10 repetitions and the standard deviation is shown in the colored band. **a)** The probe beam is aligned under $\theta = 45°$ and retro-reflected by a mirror. The Doppler shift $\Delta\nu$ is mapped onto the fluorescence signal with a double-peak feature where the beam is resonant once to the incoming and once to the retro-reflected beam. Both peaks are fitted independently around the respective maximum with a Gaussian to determine the center frequency. The distance between the peaks accounts for twice the Doppler shift from which the mean forward velocity of the atomic beam is deduced (equation 3.4). **b)** The atomic beam is probed under $\theta = 90°$ without a mirror. The peak signal U_{PD} is determined to calculate the flux. **c)** Combining the information from both measurements, the mean forward velocity $\langle v_l \rangle$ (orange) is calculated which is used to determine the flux (blue). Blue lines are shown as a guide to the eye. The flux peaks at $\delta_{2D} = -3.1\,\Gamma$ with 2.4×10^9 atoms/s. Starting from $\delta_{2D} \approx -2\,\Gamma$, the mean forward velocity drops linearly with $0.98\,\mathrm{ms}^{-1}/\Gamma$.

from $\delta \approx -2\Gamma$, the velocity drops linearly with $0.98\,\mathrm{ms}^{-1}/\Gamma$. This is plausible, as higher detunings will reduce the scattering from the pusher- and retarder beam that together accelerate the atoms. Meanwhile, the flux peaks at $\delta_{2D} = -3.1\,\Gamma$ with $2.4 \times 10^9\,\mathrm{atoms/s}$.

Dependency of the pushing beam

In a second step, the dependency of the pusher power is investigated for a detuning of $\delta_{2D} = -3\,\Gamma$. The above measurements have been repeated where each time the power in the pushing beam is varied (figure 3.4). The power is adjusted by turning a rotatable half waveplate in the splitting module of the laser system (section 3.4) which rotates the polarization of the light. A subsequent polarizing beamsplitter cube then reflects different amounts of power into a beam dump reducing the transmission. Crucially, the power of the retarding beam has to be adjusted as well: If the power in the retarder is greater than the one in the pusher, the direction of flux is reversed and almost no atoms arrive in the science chamber. Therefore, the power in the retarding beam has been adjusted to maximize the photodiode signal for each pusher power value.

As the pusher power is increased, both the flux and the forward velocity increase. While the flux saturates towards $5 \times 10^9\,\mathrm{atoms/s}$ at higher powers, the forward velocity increases linearly with $1.4\,\mathrm{ms}^{-1}/\mathrm{mW}$. This effect is exactly opposite to the behavior of the detuning as more power increases the scattering rate from the pushing beam.

Conclusion

In conclusion, the 2D$^+$-MOT is able to produce an atomic flux of up to $5 \times 10^9\,\mathrm{atoms/s}$ though at the cost of an increasing the forward velocity. These parameters can be tuned using the detuning δ_{2D} and power in the pushing / retarding beam to engineer the output velocity. This should allow for an efficient loading of the grating MOT as predicted in section 2.4.
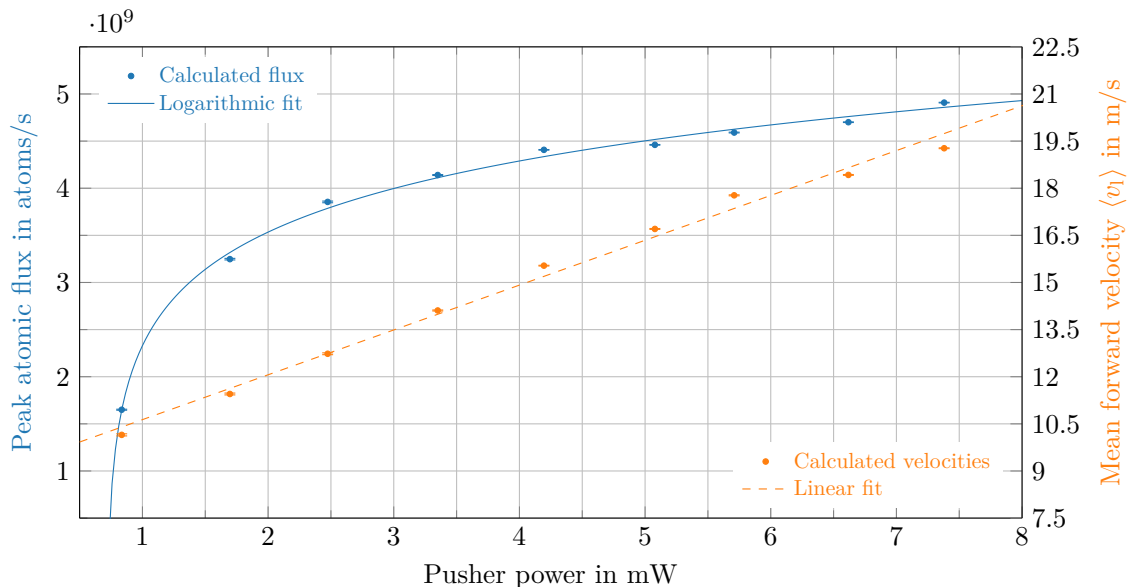
Figure 3.4: Atomic flux and mean forward velocity of the 2D$^+$-MOT for the variation of the pusher power. The measurements of figure 3.3 have been repeated for a fixed detuning $\delta_{2D} = -3\,\Gamma$ but this time the pusher power is changed. Both the atomic flux[a] and mean velocity increase with pusher power. While the flux saturates towards 5×10^9 atoms/s at higher powers, the velocity increases linearly with $1.4\,\mathrm{ms}^{-1}/\mathrm{mW}$. For every pusher power, the corresponding retarder power was adjusted to maximize the Photodiode signal.

---

a Note that the flux values are not directly comparable with respect to figure 3.3 since the oven temperature of the Rb source had been increased from $22\,°\mathrm{C}$ to $29\,°\mathrm{C}$ in between. This raises the partial pressure in the chamber and rescales the flux [40].

3.4 Lasersystem

The laser system is a critical component of the test facility. It provides frequency-tunable laser light and amplifies it to sufficient output power for the trapping and cooling of atoms. It allows to generate pulses for optical pumping and detection while addressing the relevant atomic transitions. The laser system was built within the framework of a master thesis [71] and was extended with splitting modules within a bachelor's thesis [72]. For completeness, I will briefly give an overview but will refer to these theses for details.

The laser system consists of 4 modules: The reference module, the ECDL module, the amplification & distribution module, and the splitting module, all depicted in figure 3.5. In the reference module, an external cavity diode laser (ECDL) is stabilized to the ^{85}Rb cooling transition $(5^2\mathrm{S}_{1/2}\,|F = 3\rangle \rightarrow 5^2\mathrm{P}_{3/2}\,|F = 4\rangle)$ by means of a modulation transfer spectroscopy [73]. Its light is guided through a polarization-maintaining single-mode fiber to the ECDL module where it is split to generate beatnotes with each of the four lasers. The beatnotes are picked up by fast photodiodes `[Hamamatsu Ultrafast MSM Photodetector G4176-03]` and are sent to the electronics system for frequency stabilization (see section 3.6). This way, two cooling lasers (one for the 2D$^+$-MOT and one for the 3D-MOT), one

repumping laser and a Bragg laser can be stabilized in frequency.

The light of the stabilized lasers is sent with polarization-maintaining single-mode fibers to the amplification module. Here, the light of the Bragg- and cooling lasers is amplified to up to 2 W using tapered amplifiers (TA) before it is overlaid in perpendicular polarization with the repumping light. Acousto-optical modulators are placed in the light path for the possibility of power adjustment and pulse shaping. Mechanical irises in front of the outgoing fibers are available to completely block the light. For the 2D$^+$-MOT, a 1-to-4 splitting module [72] is used to distribute the power among the transversal cooling-, pushing- and retarding beams with adjustable power ratios.
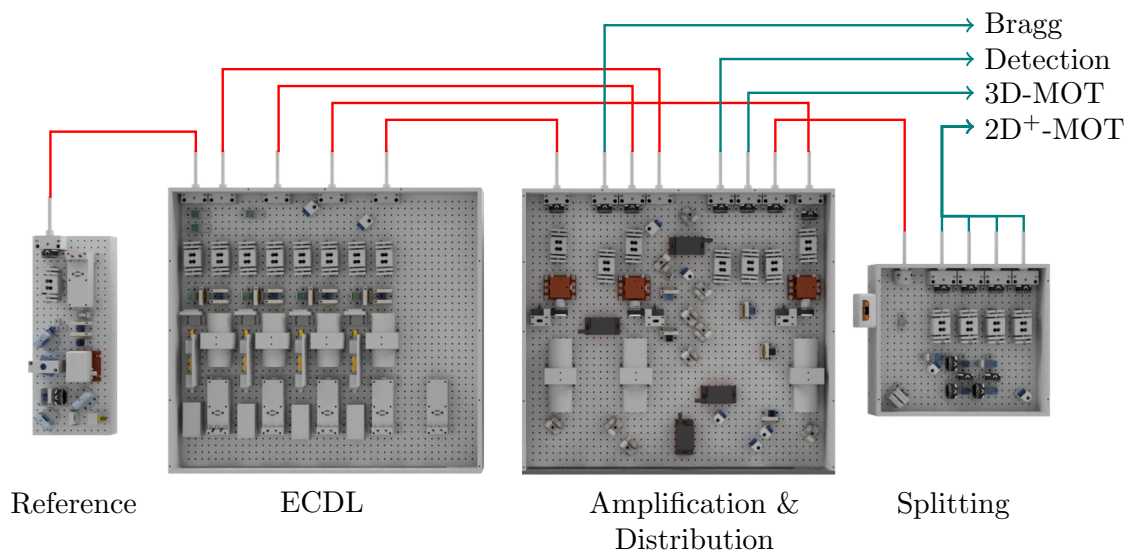
Figure 3.5: Overview of the four modules of the laser system. From left to right: A reference laser stabilized to a spectroscopy is guided into the ECDL module where beatnotes are established for four external cavity diode lasers (ECDLs) to stabilize their frequency. Their light is guided into the amplification and distribution module where tapered amplifiers are used to amplify the power of one Bragg- and two cooling lasers. The light of the repumping laser is overlaid on top of the cooling lasers before it is sent to the experiment. For the 2D$^+$-MOT, a splitting module distributes the power among four paths with adjustable power ratios as required for its operation.

3.5 Detection Systems

For the detection of the atoms, two kinds of systems are available: Fluorescence detection and absorption imaging. While the former just detects the scattering of light from the atoms on a photodiode, the latter also provides spatial information by recording the shadow of the cloud in (near) resonant light on a camera. This can be used to gather all kinds of interesting information such as the cloud position, size, shape, atom number and density. While the camera is comparably slow in taking images, the Photodiode can trace much faster signals and thus both systems provide complementary information over the course of the experimental cycle. In the following sections, both setups are described.

3.5.1 Fluorescence detection

The idea of the fluorescence detection is to deduce the number of atoms in a cloud by illuminating it from one side and recording the scattered light from a perpendicular perspective with e.g. a photodiode. This way, each of the N atoms will scatter the light with a rate R_{sc} creating a flux of isotropically emitted photons Φ_{em}:

$$N \cdot R_{sc} = \Phi_{em} \tag{3.5}$$

However, the photodiode picks up only a fraction $\frac{d\Omega}{4\pi}$ of the isotropically emitted light and thus

$$N = \frac{\Phi_{det}}{\frac{d\Omega}{4\pi} \cdot R_{sc}} \tag{3.6}$$

where $d\Omega$ is the solid angle of the photodiode. Expanding by the photon energy $E = h\nu$, where h is the Planck constant and ν is the photons frequency, allows to express the photon flux in terms of power

$$N = \frac{\Phi_{det} \cdot h\nu}{\frac{d\Omega}{4\pi} \cdot R_{sc} \cdot h\nu} = \frac{P_{det}}{\frac{d\Omega}{4\pi} \cdot R_{sc} \cdot h\nu} \tag{3.7}$$

which is in turn converted into an electric current I_{PD} by the photodiode with its power sensitivity S, specified by the manufacturer:

$$N = \frac{I_{PD}}{S \cdot \frac{d\Omega}{4\pi} \cdot R_{sc} \cdot h\nu}. \tag{3.8}$$

Finally, the photo current I_{PD} is converted into a voltage U_{PD} by a transimpedance amplifier with a gain G so that the atom number is calculated by

$$N = \frac{U_{PD}}{G \cdot S \cdot \frac{d\Omega}{4\pi} \cdot R_{sc} \cdot h\nu} \tag{3.9}$$

where

$$R_{sc} = \frac{\Gamma}{2} \frac{s_0}{1 + s_0 + 4(\delta/\Gamma)^2} \tag{3.10}$$

is the scattering rate with the natural linewidth of the transition Γ, the saturation parameter $s_0 = I/I_{sat}$ and the detuning δ. The voltage of the signal is then sampled by the analog input of the FPGA (see section 3.6) during the experiment and the atom number can be calculated afterwards, knowing the relevant parameters.

Experimental implementation and conversion factor

In the experiment, a lens system is used directly behind the viewport of the vacuum chamber in order to increase the surface $d\Omega$ from which light is gathered which increases the signal-to-noise ratio. Figure 3.6 shows a CAD model of the implemented lens system
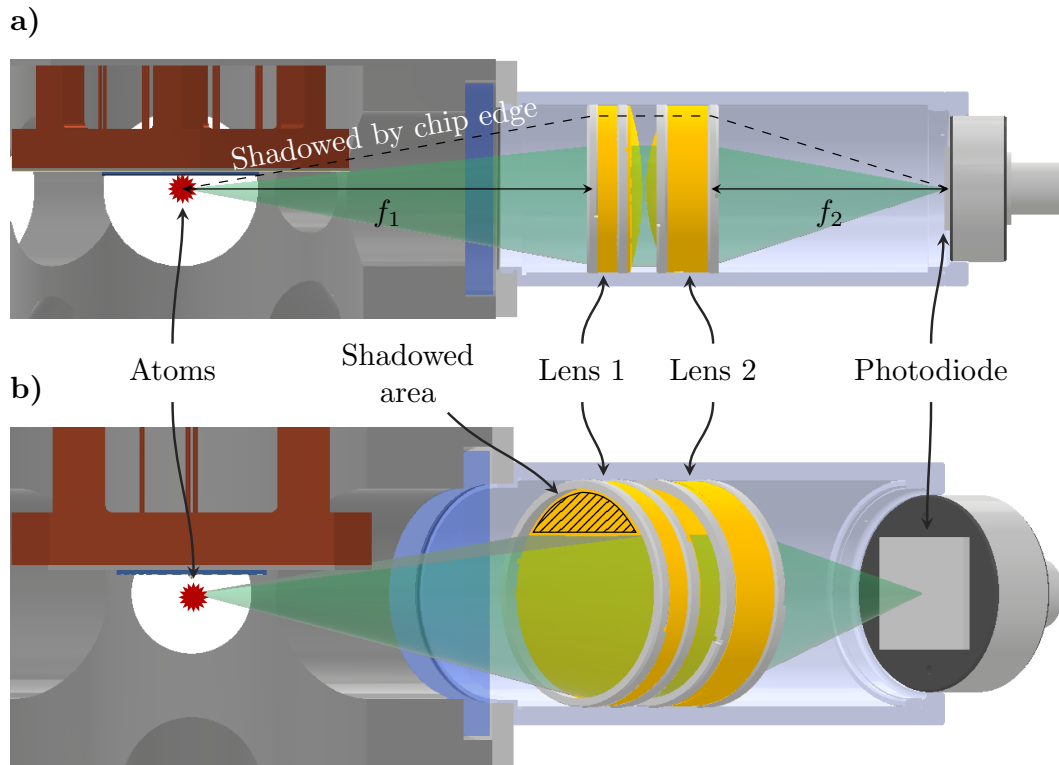
Figure 3.6: CAD of the Fluorescence Detection System using two lenses and a photodiode. **a)** Side-view: The first lens is focused on the position of the chamber center to collimate the emitted light. The second lens then focuses it on a large-area photodiode. Parts of the emitted light are clipped at the chip edge. **b)** Rotated view showing the clipped part of the emitted light on the first lens which reduces the effective solid angle from which light is gathered. Depending on the height of the atomic cloud the shadowed area may change.

using two lenses and a photodiode. The first lens [Thorlabs AC300-080-B] is positioned to have its focus on the center of the vacuum chamber to collimate the emitted light. A second lens [Thorlabs AC300-050-B] then focuses it on a $(10 \times 10)\,\mathrm{mm}^2$ square photodiode [Hamamatsu S5107] with a photosensitivity $S = 0.57\,\mathrm{A/W}$ at $\lambda = 780\,\mathrm{nm}$ as stated by the manufacturer. The photodiode is then connected to a transimpedance amplifier [FEMTO DLPCA-200-S] with a variable gain where $G = 1 \times 10^5\,\mathrm{V/A}$ is typically used for MOT loading.

The solid angle of the detection system is calculated by

$$\mathrm{d}\Omega = \frac{A}{d^2} \tag{3.11}$$

where A is the illuminated area from which light is collected and d is the distance to the source. Close evaluation of the atom chip system in figure 3.6 shows that a part of the lens area is shadowed by the chip edge reducing the effectively illuminated area. This effect depends on the height of the emission above the chip surface: While emissions from heights above 6.6 mm would fully reach the first lens, closer emission heights may

drastically reduce the effective area. In the extreme example of emission directly from the chip surface, an area of about $189\,\mathrm{mm^2}$ on the lens is shadowed which corresponds to about $30\,\%$ of the full area. However, for typical MOT loading, the cloud is positioned about $3\,\mathrm{mm}$ above the surface which shadows only $13\,\%$ of the lens area leading to an increased atom number observation of about $15\,\%$ in comparison to the full solid angle. Nevertheless, all atom numbers reported in this work that are derived from fluorescence detection are calculated based on the full solid angle neglecting the shadowed area and thus giving the most conservative estimate.

For the estimation of the scattering rate, I have assumed resonant scattering since the MOT modifies the resonance condition during operation to keep atoms in resonance by design. For the MOT loading, a power $P \approx 100\,\mathrm{mW}$ is used which is distributed among the tophat beam area of $5\,\mathrm{cm^2}$ so that $I \approx 20\,\mathrm{mW/cm^2} \gg I_s$. With theses assumptions, the scattering rate is close to its maximum value of

$$R_{\mathrm{sc}} \approx \frac{\Gamma}{2} \tag{3.12}$$

which yields the lowest conversion factor and is thus the most conservative value to state. Given the estimations from above and a lens positioning uncertainty of $1\,\mathrm{mm}$, the conversion factor

$$\eta_{\mathrm{FD}} = \frac{1}{G \cdot S \cdot \frac{\mathrm{d}\Omega}{4\pi} \cdot R_{\mathrm{sc}} \cdot h\nu} = \left(4.92^{+0.65}_{-0.07}\right) \times 10^8 \ \mathrm{atoms/V} \tag{3.13}$$

is calculated. Here, the error with positive sign is mostly dominated by the shadowed area uncertainty and the error with negative sign arises from the scaling of the solid angle $\mathrm{d}\Omega = A/d^2$ due to the lens positioning uncertainty in d. For atom number conversions, the nominal value is taken in the following.

3.5.2 Absorption detection

Spatial information of the atomic cloud can be crucial when it comes to optimizing the experiment. For example, the temperature of an ensemble is determined by evaluating the size evolution of the cloud. Therefore, it is important to be able to "take photographs" of the atoms.

In an absorption detection system, light is sent through the vacuum chamber onto a camera (see figure 3.7a). When the light frequency is set to the atomic transition frequency it will be absorbed by the atoms and subsequently re-emitted isotropically. This leaves a shadow of the atomic cloud in the image of the beam. When two images are taken - one with and one without atoms - the difference of the two shows the pure absorption signal of the atoms. The image can then be evaluated for properties such as density, size and atom number.

Imaging Hardware

In general, there are multiple design solutions for such an imaging system. A particularly interesting one is the two-lens system as depicted in figure 3.7a. It consists of two convex lenses with focal lengths f_1 and f_2 that are separated in a $f_1 - (f_1 + f_2) - f_2$ configuration. When the object (i.e. the atomic cloud) is placed in the focal plane of the first lens, it is imaged in the focal plane of the second lens with a magnification $M = f_2/f_1$. A charge-coupled device (CCD) camera [Grasshopper3 USB3 GS3-U3-15S5M-C] in this plane then records the image. What is particularly interesting about the design is the intermediate focus point between the lenses. When an aperture is placed here, it blocks light from off-axis incidents but lets on-axis light pass through which filters the image from unwanted stray light. Two of such absorption detection systems have been built for the atom chip test facility:

The first system features two identical lenses with $f_1 = f_2 = 75\,\text{mm}$ [Edmund Optics #49-373] and a design magnification $M_1 = f_2/f_1 = 1$. Its field of view is thus identical to the size of the CCD sensor which is $8.93\,\text{mm} \times 6.66\,\text{mm}$. This is a reasonable trade-off between field of view and required imaging resolution. The second system is de-magnifying in order to capture a larger field of view. This eases temperature determination of the atomic ensembles as longer times of flight can be observed. The lenses are chosen with focal lengths $f_1 = 75\,\text{mm}$ [Edmund Optics #49-373] and $f_2 = 38\,\text{mm}$ [Edmund Optics #49-791] for a design magnification $M_2 \approx 0.51$, similar to the sketch in figure 3.7a.

The magnifications have been verified experimentally recording the center of mass motion of free-falling atoms. By comparing the recorded trajectory $(x(t), y(t))$ on an image to a re-scaled parabola

$$\begin{pmatrix} x(t) \\ y(t) \end{pmatrix} = M \cdot \left(\frac{1}{2}\, g \begin{pmatrix} \sin(\theta) \\ \cos(\theta) \end{pmatrix} t^2 + \begin{pmatrix} v_x \\ v_y \end{pmatrix} t + \begin{pmatrix} x_0 \\ y_0 \end{pmatrix} \right) \tag{3.14}$$

with a projection of gravity onto the image under an angle θ the magnifications have been determined to $M_1 = 0.991$ and $M_2 = 0.479$ respectively.

a)

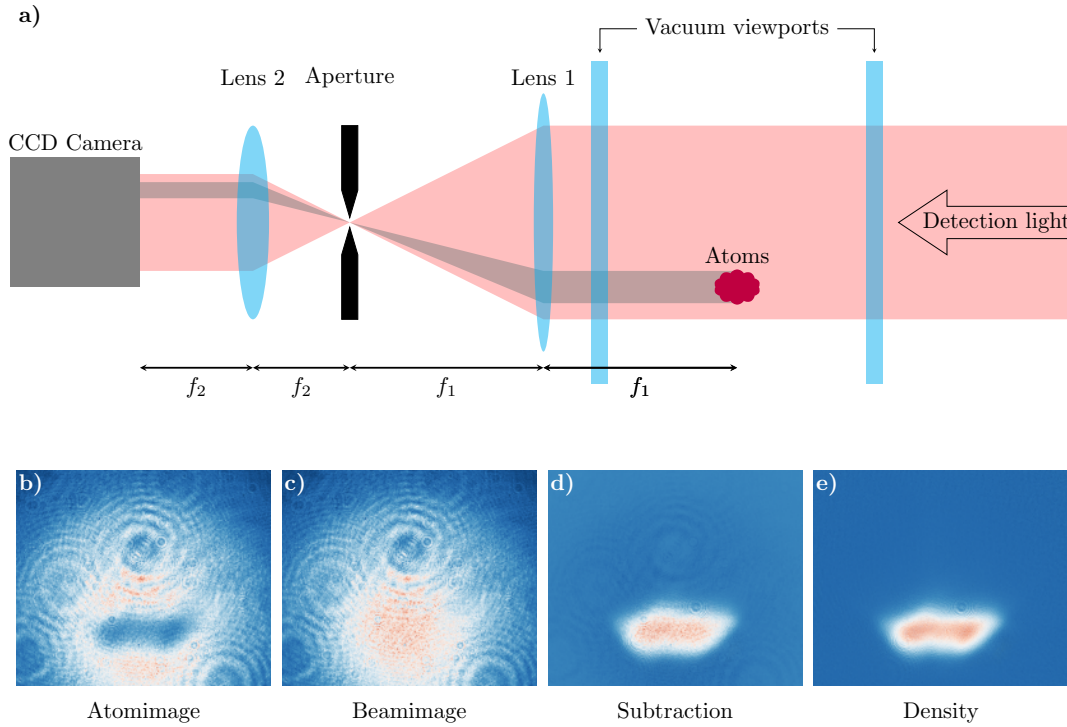| Atomimage | Beamimage | Subtraction | Density |

Figure 3.7: Schematic overview of the absorption detection system. **a)** (Near-) resonant detection light (red) is sent through the atomic cloud (purple) leaving a shadow (grey) as the atoms absorb the light. The shadow is then imaged onto a charge-coupled device (CCD) camera in a $f_1 - (f_1 + f_2) - f_2$ configuration with a magnification $M = f_2/f_1$. An aperture in the intermediate focal plane filters light from off-axis sources that could potentially disturb the imaging. The drawing sketches a magnification of $M = 0.5$. When two images are taken - one with the atoms (**b)**) and one without (**c)**) - the difference of them (**d)**) shows only the signal of the atoms which is used to calculate the optical density (**e)**).

Image Acquisition

In total, three images need to be taken for the absorption imaging technique: First, an image of the atomic cloud absorbing from a (near) resonant probe beam leaving a shadow in the image ("atomimage"). Second, an identical image of the detection beam after the atoms have left the imaging area ("beamimage"). In practice, this image is taken 250 ms after the first image. Third, an image without atoms or probe light which is subtracted from both images to account for independent background light ("background image"). Subtracting the atomimage from the beamimage then reproduces the pure absorption signal of the atoms. Example images of this procedure are shown in figure 3.7 b) - d).

For each image acquisition, the CCD camera is configured for an exposure time of 110 µs which is started by an external trigger signal sent by the computer control system (see section 3.6). During this time the sensor is exposed to a 50 µs light pulse which is generated by switching an acousto-optical modulator in the laser system. This time has intentionally been chosen shorter than the actual camera exposure time to get a well-defined exposure

time and mitigate potential timing jitter which would lead to different image intensities if the time periods do not overlap completely. The 2D-MOT laser is used for the detection since there is plenty of time to adjust the light frequency between the loading and detection phase of the experiment. After passing through a polarization-maintaining optical fiber, the light is right circularly polarized by a quarter wave plate before it is collimated to a beam diameter of 15 mm. The collimation has been verified using a shearing interferometer. For the detection process, a quantization field of $|\vec{B}_{\mathrm{det}}| = 6.2\,\mathrm{G}$ is applied along the light axis in the vacuum chamber.

Image Evaluation

The image evaluation of the absorption detection is largely based on [74] as implemented by [75]: Briefly, the idea is to calculate the density of the atomic sample through Lambert-Beer's law [74]

$$\frac{\mathrm{d}I}{\mathrm{d}z} = -n(x,y,z)\,\sigma_c\,I \tag{3.15}$$

by inferring how much intensity I has been absorbed through the atomic density $n(x,y,z)$ with the cross-section

$$\sigma_c = \frac{\sigma_0}{1 + I/I_{\mathrm{sat}} + 4\delta^2/\Gamma^2} \tag{3.16}$$

where

$$\sigma_0 = \frac{\hbar\omega}{I_{\mathrm{sat}}}\frac{\Gamma}{2} \tag{3.17}$$

is the resonant scattering cross-section. Integration of equation 3.15 along z gives

$$\left(1 + 4\frac{\delta^2}{\Gamma^2}\right)\ln(I) + \frac{I}{I_{\mathrm{sat}}} + c_1 = -\sigma_0\,\tilde{n}(x,y) + c_2 \tag{3.18}$$

where c_1 and c_2 are integration constants and

$$\tilde{n}(x,y) \equiv \int n(x,y,z)\,\mathrm{d}z \tag{3.19}$$

is the integrated column density along the detection axis perpendicular to the CCD sensor. Evaluation for the atom- and beamimage with respective local pixel intensities I_a and I_b gives a set of two equations

$$\text{Atomimage:} \quad \left(1 + 4\frac{\delta^2}{\Gamma^2}\right)\ln(I_a) + \frac{I_a}{I_{\mathrm{sat}}} + c_1 = -\sigma_0\tilde{n}(x,y) + c_2 \tag{3.20}$$

$$\text{Beamimage:} \quad \left(1 + 4\frac{\delta^2}{\Gamma^2}\right)\ln(I_b) + \frac{I_b}{I_{\mathrm{sat}}} + c_1 = c_2 \tag{3.21}$$

where for the beamimage $\tilde{n}(x,y) = 0$. Together these simplify to

$$\left(1 + 4\frac{\delta^2}{\Gamma^2}\right)\ln\frac{I_b}{I_a} + \frac{I_b - I_a}{I_{\text{sat}}} = \sigma_0\,\tilde{n}(x,y) \tag{3.22}$$

so that the atomic density can be calculated by evaluating the intensities I_a and I_b of the images. For every pixel ij on the CCD camera, the intensity is the incident power P_{ij} per pixel area A

$$I_{ij} = \frac{P_{ij}}{A} \tag{3.23}$$

where the power is the total energy $\hbar\omega$ deposited by N_{ij} photons during the exposure time t_{exp}

$$P_{ij} = N_{ij}\frac{\hbar\omega}{t_{\text{exp}}} \tag{3.24}$$

and the effective area of a pixel is

$$A = \left(\frac{d_p}{M}\right)^2 \tag{3.25}$$

where d_p is the pixel size and M is the magnification of the detection system. Photons are converted on the sensor with the quantum efficiency q_E into electrons e^- where each electron is in turn converted into a read-out digital count c_{ij} with a gain g:

$$N_{ij} = \frac{g}{q_E}c_{ij}. \tag{3.26}$$

Combining these equations, the conversion is calculated by

$$I_{ij} = \frac{\hbar\omega\,g\,M^2}{q_E\,t_{\text{exp}}\,d_p^2}\,c_{ij} \tag{3.27}$$

for each pixel ij. The relevant camera parameters are listed in appendix A.1 for the used camera [`Pointgrey Grasshopper USB3 GS3-U3-15S5M`]. With this information, the atomic density is calculated for a set of atom- and beamimage. Fitting a two-dimensional function to the density, e.g. a 2D-Gaussian, can then be used to determine the size and atom number. In practice, these fits are resource intensive and take a long time which is why in everyday usage often the integrated density along a row or column is used with a much faster 1D-fit.

3.6 Experimental Control

Running a quantum optical experiment requires to control a multitude of experimental parameters such as electric currents, light frequencies and RF-signals with precise timing. A modern physics experiment is thus controlled by a computer to allow for complex parameter

changes and to guarantee repeatability. An experimental sequence consists of multiple sets of parameters that are executed after another for a predefined amount of time. In this experiment, the sequence is programmed with a graphical user interface on a control computer running LabVIEW[1] and uploaded to the executing hardware (see figure 3.8). Next, the sequence is simultaneously started across all devices with a common start trigger ensuring synchronized execution.

Two compact TBus electronic stacks [76] are available to control the laser system and the currents during the experiment. These have been developed in the institute for the experimental control of droptower [14] and sounding rocket [13, 15] experiments. Therefore, they resemble the use-case scenario of real missions very closely and ensure the transferability of results. The TBus laser stack consists of current drivers for the lasers, direct digital synthesis (DDS) frequency generators and a frequency control card for laser frequency stabilization. The TBus current stack houses four bipolar current drivers [16] for the 2D-, X-, Y- and Z-coil respectively, two unipolar chip current drivers [16] for the atom chip and a shutter driver for the laser system. The currents in the coil current drivers are limited to $\pm 5\,\text{A}$ and for the chip drivers to $10\,\text{A}$. Every driver has been individually optimized for its specific load to minimize switching times which are typically on the order of $0.5 - 2\,\text{ms}$, depending on the load and requested current. Every current driver is able to output linear ramps and jumped signals. For the atom chip, an intermediary chip protection board [76] is used as an additional measure to protect the atom chip from overcurrents in case of current driver failure. It provides in-line fuses, current measurements and an automatic timed shutoff to prevent overheating of the atom chip.

A realtime computer with a field programmable gate array (FPGA) `[NI PCIe 7851R]` controls 96 digital in- and output channels and each 8 analog-in and -outputs[2] . It triggers the image acquisition in the absorption detection and records the fluorescence detection signal. Furthermore, it can provide timed output signals that correspond to exact times in the experimental sequence for debugging.

During the experimental run, monitoring data is gathered by the computer control system, e.g. the read-out currents, supply voltages and laser lock frequencies. This data can later be used to verify the experimental sequence which greatly helps in debugging.

Finally, the experimental detection data, e.g., acquired images or recorded data traces, are transferred to the control computer, where it is stored on a hard drive.

---

1   The LabVIEW program has been developed and refined in the group by many generations of PhD students. I am thankful to all previous contributors and proud to have improved and extended the functionality myself.
2   Most of the FPGA channels are barely used and hardly necessary since almost all functionality is covered by the TBus electronics. The realtime FPGA is just convenient to have for flexibility and future developments.
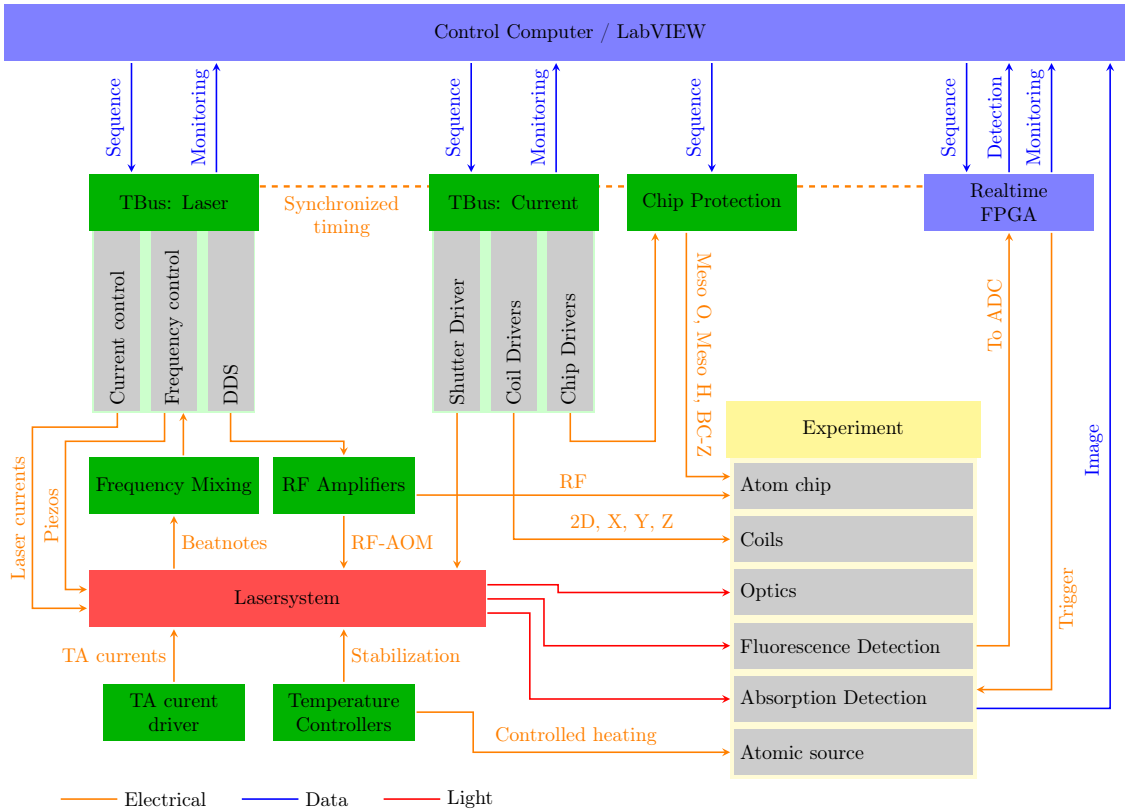
Figure 3.8: Diagram of the computer control system and peripheral electronics. A control computer sends the programmed experimental sequence to two TBus control electronic stacks, a chip protection board and a real-time computer with an FPGA. Once the upload is complete, the sequence is started with a synchronized trigger. During the experiment, the control electronics follows the pre-programmed steps while monitoring data is acquired by the control computer. Finally, the data of the fluorescence and absorption detection is transferred to the control computer, concluding the experiment.

CHAPTER 4

Experimental results

This chapter describes the experimental results acquired with the grating atom chip described in section 2.3. First, the design and characterization of a top hat beam expander is shown that is used to illuminate the grating in order to achieve a large volume where balanced laser cooling may be achieved. Afterwards, the results of the magneto-optical trapping, sub-Doppler cooling, state preparation and magnetic trapping are presented. The chapter ends with characterizations on evaporative cooling and the gauging of the external bias coils around the chamber using RF-spectroscopy on atoms released from the magnetic trap.

4.1 Grating illumination

As it was pointed out in section 2.1.1, balanced laser cooling is achieved when the intensity-weighted wave vectors of all involved laser beams cancel each other. Since the diffracted secondary beams are derived from the incoming beam, their intensity depends on the spatial illumination profile. For a Gaussian incoming beam, this would mean that the strong central part needs to be compensated by the sum of all secondary beams which are derived from the weaker intensities in the outer radial parts. Intensity balance can therefore only be achieved for a single point on the central axis since any deviation in height would always have an intensity mismatch. Specifically, this is also true for any radial displacement as different radial intensities from the secondary beams would contribute to the radial light balance. At the same time, the alignment between the center of the beam and the center of the grating would be crucial. These issues persists with any incoming beam profile that does not feature translational symmetry.

A large volume of balanced laser intensities can therefore only be achieved with a homogeneous grating illumination as the balance equation effectively compares different spatial regions of the incoming beam. Therefore, a compact tophat beam expander was designed, constructed and characterized to illuminate the grating.

4.1.1 Design of the tophat beam expander

A typical laser beam as commonly applied in cold atom experiments is of a Gaussian shape which conveniently exits optical fibers. In order to illuminate the full gating area with a flat intensity profile, one needs to both expand the beam spatially and redistribute the power in the beam. A compact tophat beam expander was designed for this task making use of laser line lenses [Edmund Optics LASER LINE GEN 45 DEG UNMTD]. These are specifically designed to refract light in a particular way to redistribute the power in the beam into a

line. Using refractive instead of diffractive elements for beam shaping is expected to have a low influence on the polarization of the light.

The full design of the tophat beam expander is shown in figure 4.1. Briefly, a collimated Gaussian beam from a commercial fiber coupler [`Schäfter + Kirchhoff 60FC-4-A4.5S-02`] is sent through a quarter wave plate to adjust the polarization of the beam. The beam diameter of 0.8 mm is matched to the design width of the laser line lenses. They are made with cylindrical symmetry and act only in one direction. After passing through such a lens, the light diverges with an angle of 45° which is reduced in the design by a strong convex lens [`Thorlabs LA1951-B, N-BK7 Plano-Convex Lens, ∅1", f = 25.4 mm`] close by. In order to achieve a tophat beam in two dimensions, two perpendicular cylindrical laser line lenses are placed directly after another. This creates two distinct focal points in the perpendicular directions which is accounted for by a cylindrical convex lens [`Thorlabs LJ1695RM-B, N-BK7 Mounted Plano-Convex Round Cyl Lens, ∅1", f = 50 mm`]. Finally, a convex lens [`Edmund Optics #47-390, ∅30 mm, f = 120 mm`] limits the output beam expansion over a reasonable distance where the grating will be placed.

The beam expander design has been realized using only commercial off-the-shelf components which were placed in a lens tube to be able to adjust the lens positions. In total, the expander is just 16 cm long which is much shorter than typical commercial counterparts. In the future, one may want to shorten the expander even further for increased stability and reduced weight. This seems easily possible by manufacturing a dedicated "2D laser line lens" to remove the extra cylindrical lens. Furthermore, the spacing around the quarter wave plate may be reduced which was added for convenience of adjusting the polarization continuously in an easy-to-use commercial mount.

4.1.2 Intensity profile characterization

After adjustment of the optics, the beam profile was characterized 10 cm behind the expander where the grating is placed in the experiment (see figure 4.1). This turned out to be non-trivial, as typical beam cameras are not large enough to cover the full size of the beam. Therefore, 30 images were recorded with a slight overlap between the individual images using a translation stage. The overall image was then recovered by stitching the individual images together using a Fourier-shift algorithm [77]. The analysis of the full beam profile (figure 4.2) shows a rectangular plateau of homogeneous intensity with a size of about 20 mm × 20 mm which is able to cover the entire area of the grating. The plateau contains about 77 % of the overall power and the occurrence of intensity values is of a Gaussian distribution with a standard deviation of $\sigma_g = 0.25$ around the normalized mean intensity. This means, that about 67 % of the intensity values lie within ±25 % around the mean intensity. Compared to a widened Gaussian beam where only the central part would be taken, this is much more power efficient. This profile is used to illuminate the grating in the experiment as presented in the following.
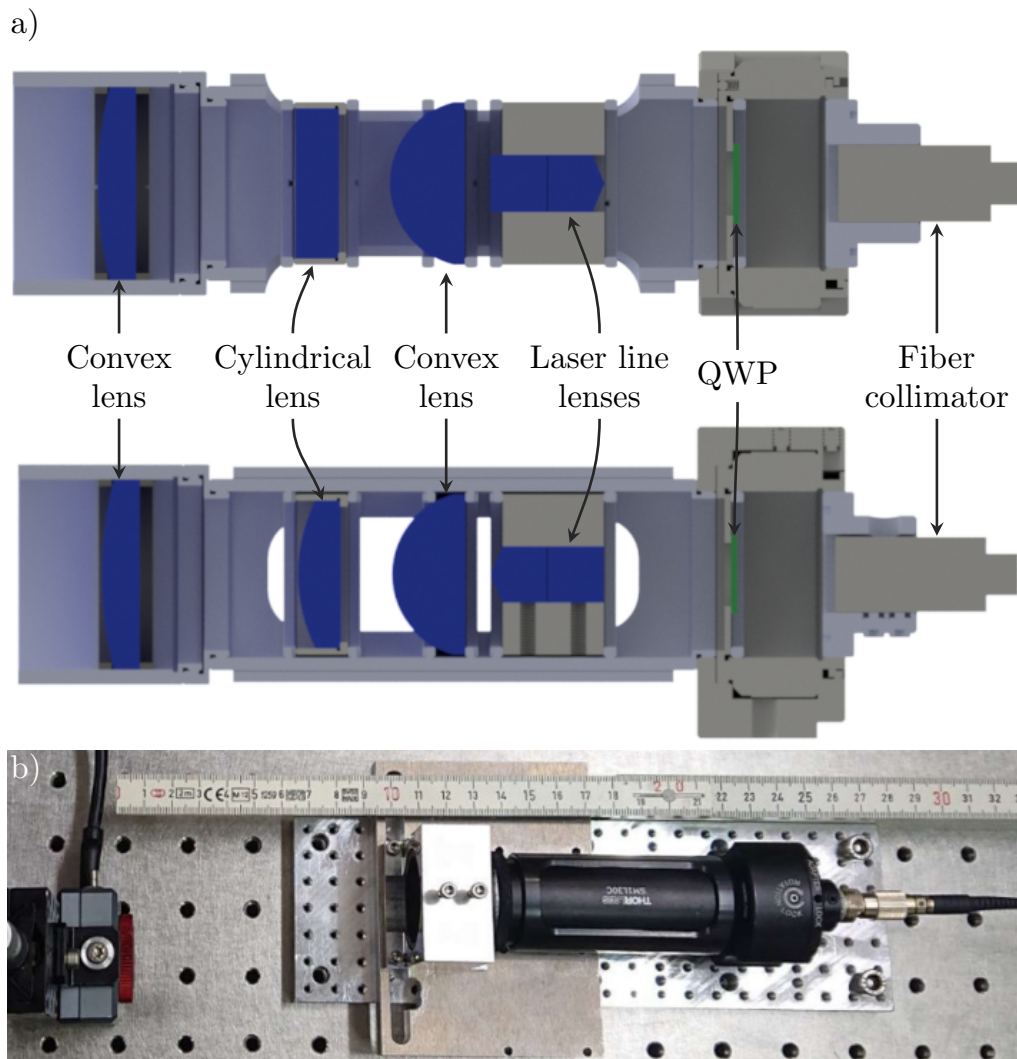
Figure 4.1: CAD model and photograph of the tophat beam expander. **a)** Two perpendicular sectional views through the CAD model of the tophat beam expander. From right to left: A polarization-maintaining optical fiber transmits light into a commercial fiber collimator where it is collimated with a beam diameter of 0.8 mm, matched to the design width of the laser line lenses. After transmitting through a quarter waveplate (green), it is sent through two cylindrical laser line lenses that are placed perpendicularly after another. They each redistribute the power in their respective direction while keeping the other axis unchanged. After the laser line lenses, the beam is divergent with an angle of 45° and has two separate foci in the perpendicular directions. A convex lens limits the initial strong divergence and a cylindrical lens accounts for the distinct foci before an output convex lens finally collimates the beam. This way, a rectangular beam profile with a central plateau of homogeneous intensity is created (see figure 4.2). **b)** Assembled beam expander set up for beam characterization with a translation stage 10 cm away which is where the grating will be placed in the experiment. The beam expander is about 16 cm long.
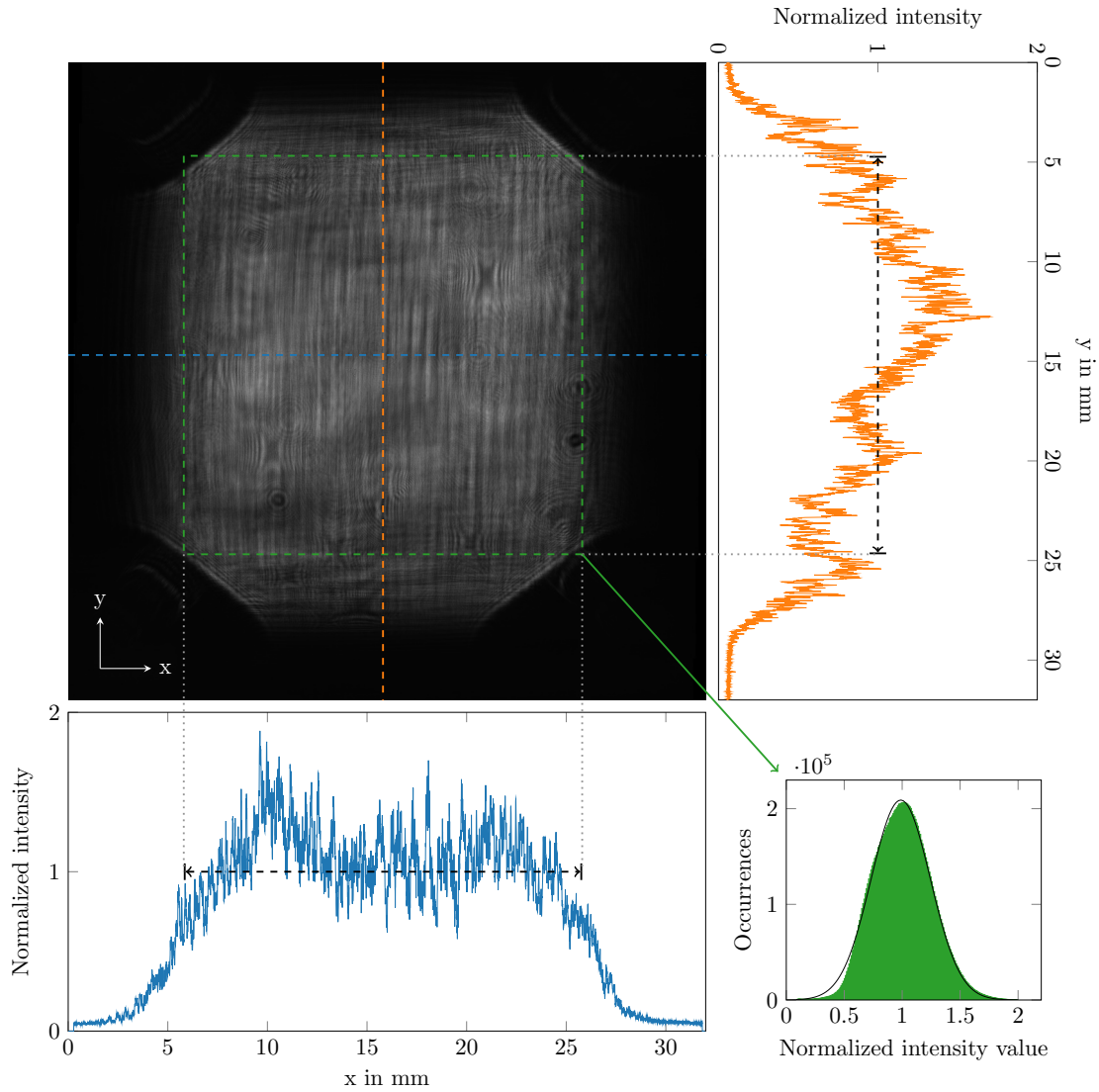
Figure 4.2: Beam profile characterization of the tophat beam expander. 30 individual beam images have been recorded with a translation stage and were stitched together into a single image using a Fourier-shift algorithm [77]. The image analysis shows a central plateau with $20\,\text{mm} \times 20\,\text{mm}$ size of homogeneous intensity (green dashed square) that is used to illuminate the full area of the grating. Two cuts along the indicated dashed lines show an exemplary profile along the x and y direction. A statistical analysis of the plateau shows an approximately Gaussian distributed occurrence of intensity values around the mean intensity with a standard deviation of $\sigma_g = 0.25$.

4.1.3 Polarization adjustment

The polarization of light can be fully described using the Stokes parameters [78] which is a normalized set of parameters (S_1, S_2, S_3) indicating the relative amounts of intensity in various polarization components. While the parameters S_1 and S_2 describe the proportion of light in linear polarization, S_3 indicates the amount of circular polarization.

The polarization of the tophat beam has been characterized with a commercial polarization analyzer [Schäfter+Kirchhoff SK010PA] by rotating the quarter waveplate with respect to the fixed optical fiber emitting linear polarized light (figure 4.3). As the waveplate is rotated, the polarization can be continuously changed between left- and right-circular $(S_3 = \pm 1)$ indicating the low influence of the optical components in the expander. This is a distinct advantage of using refractive rather than diffractive optical elements to create the tophat shape as these typically affect the polarization state.

Experimentally, the optimum polarization was found to be exactly right circular.
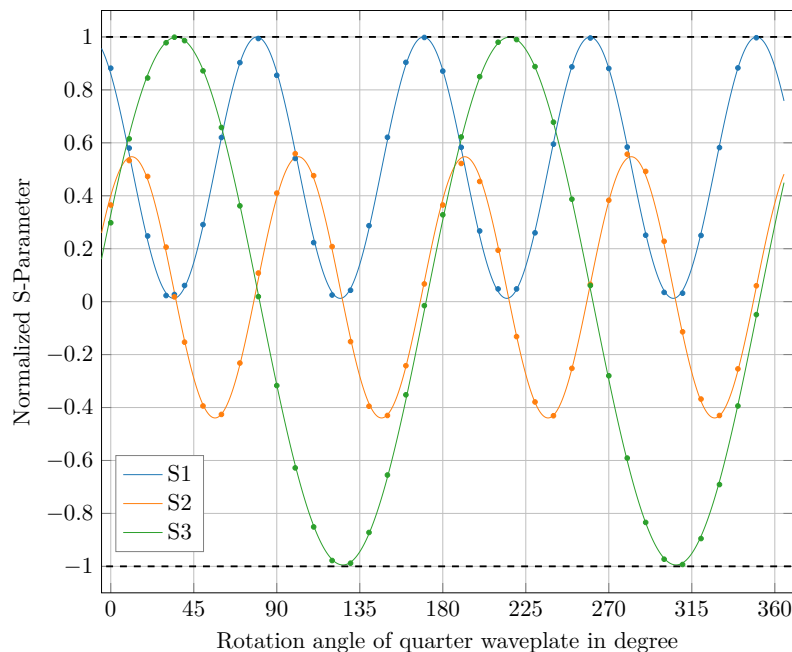
Figure 4.3: Polarization characterization of the tophat beam expander recording the Stokes parameters with a commercial polarization analyzer. As the quarter waveplate in the expander is rotated, the output polarization can be adjusted continuously between fully left $(S_3 = -1)$ and fully right circular $(S_3 = +1)$. Lines show sinusoidal fits to the data.

4.2 Magneto-optical trapping with the grating atom chip

With the beam expander set up, loading of atoms can be started from the 2D$^+$-MOT. For the 3D-gMOT to work, the grating is illuminated with circular polarized light and the upright magnetic quadrupole field is turned on. As detailed in section 2.2.3, the magnetic field is generated by the combination of a wire loop beneath the grating ("meso-O" wire) and an external perpendicular bias field generated from the Z-coil. Here, the bias field in Z-direction compensates the field of the wire loop at some height above the grating which is where the magnetic field zero locates[1]. By changing the currents in both structures, not only the position of the magnetic field zero is adjusted but also the gradient of the field. In general, stronger currents I_O in the wire loop will lead to stronger gradients. However, if the coil current is not suitably adjusted, the zero position is moved as well. Therefore, a multi-dimensional scan of the gMOT loading was performed adjusting the currents

Fig. 4.4: View into the vacuum chamber towards the end of gMOT loading. The fluorescence of about 1×10^9 atoms is visible above the center of the grating. White lines outline the three grating sections.

in the wire loop and Z-coil (see figure 4.5). For every current combination, the gMOT was loaded for 1 s at a fixed detuning while recording the fluorescence of the atoms[2] (see figure 4.4). The sequence begins with a 100 ms recording of background light during which the 2D$^+$-MOT and the light in the chamber are already turned on but the atom chip fields are still offline. This way, no atoms are trapped and the baseline signal is found which is subtracted from the fluorescence signal before it is converted into atom number using equation 3.9. The measurement was repeated for detunings in the range of $\delta_{3D} = -1.8\,\Gamma...-2.3\,\Gamma$. Magnetic field simulations (see Appendix A.3.2) provide the values for the gradient and position of the magnetic field minimum.

Evaluating the data, optimum loading was found when the magnetic field zero is located about 2.7 mm above the grating surface. This coincides with the design height of the cold atomic beam from the 2D$^+$-MOT and hints towards a necessity to match the magnetic field minimum with the height of the incoming atomic beam.

In terms of the magnetic field gradient, a plateau with gradients between 28 G/cm and 32 G/cm was observed where more than 1×10^9 atoms are loaded within 1 s. Similar results were observed for detunings δ_{3D} between $-1.8\,\Gamma$ and $-2.3\,\Gamma$. The maximum atom number was found to be 1.1×10^9 after 1 s of loading with $I_O = 8.1\,A$, $I_z = -4.7\,A$, and $\delta_{3D} = -2.1\,\Gamma$.

---

1   The minimum can be moved around within the area of the wire loop by applying additional external fields in X- and Y-direction respectively. The orientation of the quadrupole is not significantly changed by this.

2   I have restricted myself to MOT loading times of maximum 1 s as typical metrological applications prioritize experimental repetition rate where long MOT loading is not feasible. Furthermore, this causes excessive heating of the atom chip which would require complimentary cool-down phases. The MOT is typically not fully saturated after 1 s but begins to do so. Full saturation is typically reached after $2 - 3$ s.
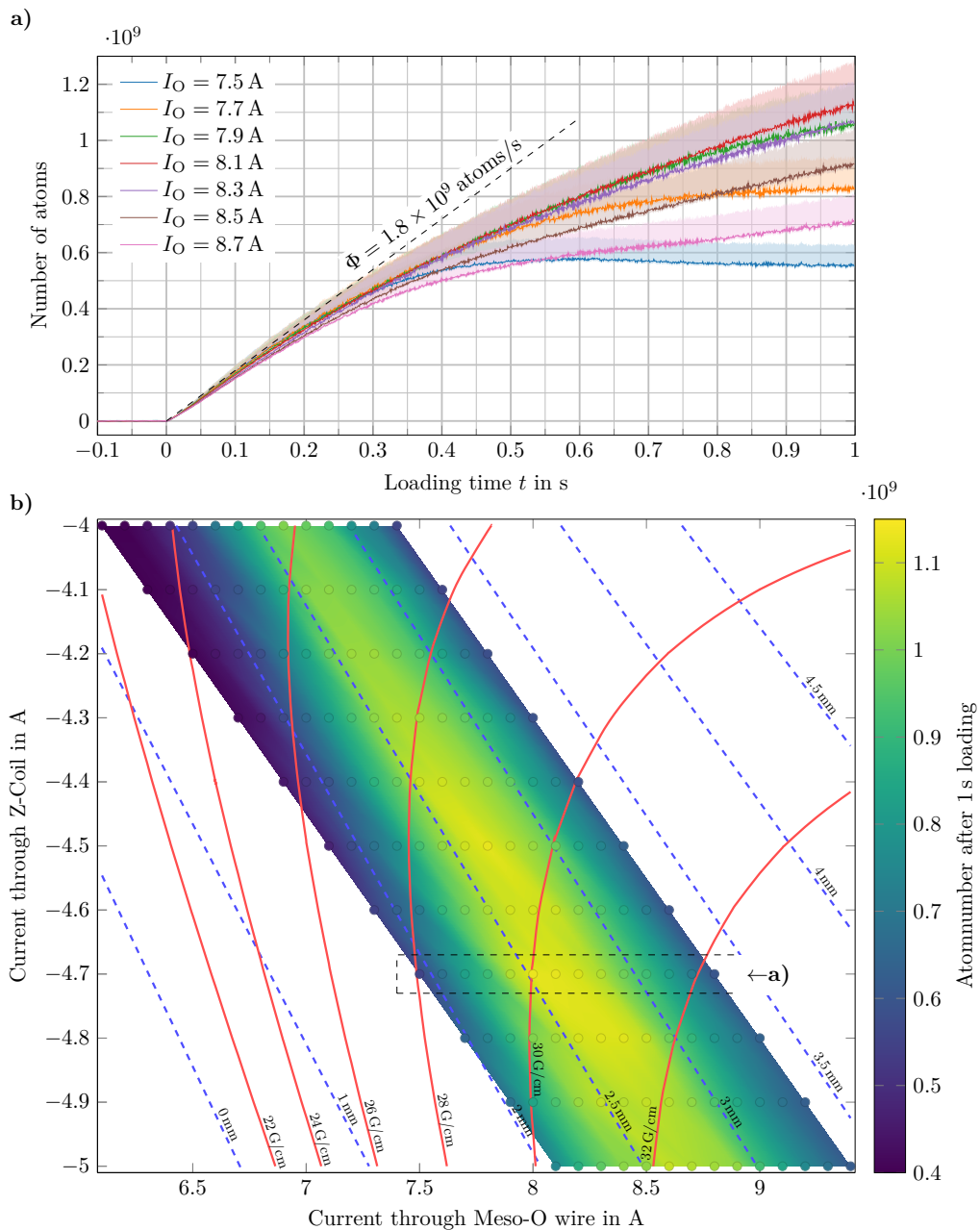
Figure 4.5: Loading of the gMOT. **a)** Exemplary loading curves of the 3D gMOT with $\delta_{3D} = -2.1\,\Gamma$ and $I_z = -4.7\,A$ for a loading duration of 1 s . The atom number is measured using fluorescence detection as described in section 3.5.1 with corresponding uncertainty bands. After a constant initial flux of $\Phi = 1.8 \times 10^9\,\text{atoms/s}$, the atom number saturates towards different levels depending on the applied current I_O. A broader investigation in **b)** shows more current combinations which adjust the position of the quadrupole zero and the field gradient at the same time. Measured data points are circled in grey. The dashed blue contour lines indicate the height of the minimum above the grating surface and solid red lines show the magnetic field gradient which are both calculated from magnetic field simulations (see Appendix A.3). Ideal loading is achieved for heights of about 2.7 mm which corresponds to the height of the incoming atomic beam from the 2D$^+$-MOT. The dashed box highlights data points shown in a). Outside the shaded areas, the gMOT loading rate was found to be low.

4.3 Sub-Doppler cooling

After the magneto-optical trap, the temperature of the cloud is about $T = 1\,\mathrm{mK}$. While this is a lot colder than room temperature, the corresponding kinetic energy is still too large to allow for efficient magnetic trapping and further optical cooling has to be employed.

Traditional sub-Doppler cooling relies on optical pumping in the complex lattice structure spanned by all beams overlapping in the optical molasses configuration. Atoms moving through such a field are exposed to spatially varying light shifts and as such they undergo periodic variations of their energy levels. When the light fields apply the optical pumping correctly, atoms tend to climb a potential hill and are pumped back into the valley thus undergoing a Sisyphus effect. In every such cycle, energy is taken out of the system which cools it. These configurations appear traditionally in 1D-configurations with either perpendicular linear polarization lin $\perp$ lin or opposite helical polarization $\sigma^+ - \sigma^-$. While none of these configurations directly map on the complex lattice structure of the grating MOT, still similar sub-Doppler features arise [52]. They identically require to null external magnetic fields, reduction of light intensity and further red-detuning of the cooling light.

4.3.1 Magnetic field compensation

As it was pointed out above, the magnetic field needs to be compensated for the sub-Doppler cooling to work efficiently. This is done by applying external bias fields from three perpendicular bias coils around the vacuum chamber. However, in the experimental realization it was found that dynamic magnetic fields are created when the current of the wire loop is switched off. Specifically, the optimum applied magnetic field to null the total field was found to be time-dependent, mostly in Z-direction (perpendicular to the atom chip surface). This is thought to be caused by eddy currents circulating in the atom chip mount which generate a field in Z-direction. Even though some slits were placed in the chip mount, these are obviously not sufficient to suppress them completely. Nevertheless, the effect was characterized using the atoms as a probe for the magnetic field.

Eddy current characterization

The eddy currents can be characterized by compensating their generated field after different shutoff times. Assuming sub-Doppler cooling works best when the total magnetic field is nulled, the atoms themselves can act as a probe. To measure this, the atoms are cooled in a $1\,\mathrm{ms}$ short molasses configuration. As the dynamic field disturbs this process, the cooling becomes inefficient and the temperature remains high. By applying an additional external compensation field during this short duration, the eddy current magnetic field is compensated and the cooling becomes more efficient. Therefore, the strength of the field is found when the temperature of the cloud is minimal (figure 4.6a)[1]. By applying this routine for different shutoff times, the time-dependency is tracked (figure 4.6b). The shutoff times have been evaluated by ramping off the magnetic field linearly for durations between $5\,\mathrm{ms}$ and $23\,\mathrm{ms}$. Indeed, for every time a minimizing field is found. By taking

---

[1] Every data point in figure 4.6a is the result of a time-of-flight measurement for that specific shutoff time and compensation current. In total, 7810 data point were taken with the experiment running continuously for about $14.5\,\mathrm{h}$ over night.

these results together, it was found that the dynamic magnetic field decays exponentially with two components as $B(t) \propto a_1 e^{-t/\tau_1} + a_2 e^{-t/\tau_1}$. The associated time constants are $\tau_1 = 2.69\,\text{ms}$ and $\tau_2 = 13.33\,\text{ms}$ respectively. This behavior is typical for eddy currents which begin with a strong decay followed by slower exponential decline [79]. With these insights, the sub-Doppler cooling phase is performed.
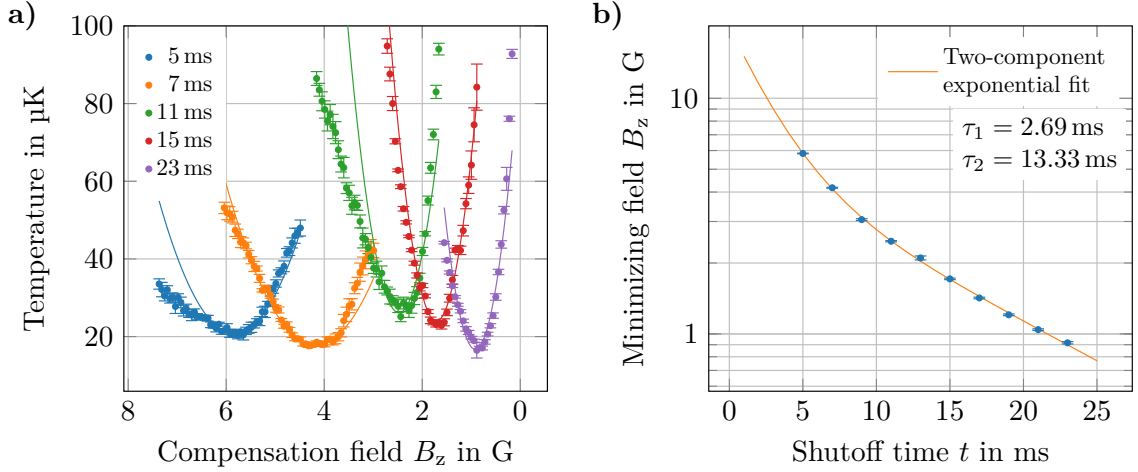

Figure 4.6: Shutoff characterization of the MOT magnetic field. When the MOT currents are ramped off, a dynamic magnetic field environment is created. **a)** The dynamic field is characterized by applying compensation fields during a 1 ms short molasses cooling step with different shut-off times $t = 5...23\,\text{ms}$, where exemplary datasets are shown here. When the dynamic field is compensated, the temperature is minimal and the average magnetic field during that time is found. **b)** Evaluation of the minima found in a) show that the dynamic magnetic field decays exponentially in two stages with associated time constants $\tau_1 = 2.69\,\text{ms}$ and $\tau_2 = 13.33\,\text{ms}$ respectively.

4.3.2 Cooling routine

The presence of extended dynamic fields from switching necessitates a prolonged waiting time for the fields to decay. Therefore, the chip currents are not switched directly but are ramped down linearly over a duration of $18\,\text{ms}$ to $(I_\text{O}, I_\text{z}) = (0.9, -0.2)\,\text{A}$ which corresponds to a vertical magnetic field gradient of $B'_z = 1.4\,\text{G/cm}$. Meanwhile, the cooling light is detuned further to $\delta_{3\text{D}} = -6.5\,\Gamma$. In a second step, the gradient is held constant for $3\,\text{ms}$ and the light detuning is linearly increased further to $\delta_{3\text{D}} = -9.8\,\Gamma$. For the actual sub-Doppler cooling phase, the magnetic field has to be compensated. To avoid atom light interaction during magnetic field switching, the light is switched off completely for $1\,\text{ms}$ by switching the radio frequency applied to an acousto-optical modulator to an off-resonant value. While the light is off, the chip current is turned off and the bias fields for magnetic field compensation are set. Afterwards, the atoms expand in the optical molasses configuration where the final optical cooling process takes place for $4\,\text{ms}$. During this time the light intensity is ramped down linearly from $24.0\,\text{mW/cm}^2$ to $0.74\,\text{mW/cm}^2$ and the detuning is linearly increased further to $\delta_{3\text{D}} = -25.6\,\Gamma$.

To evaluate the success of the cooling scheme, the temperature has to be determined.
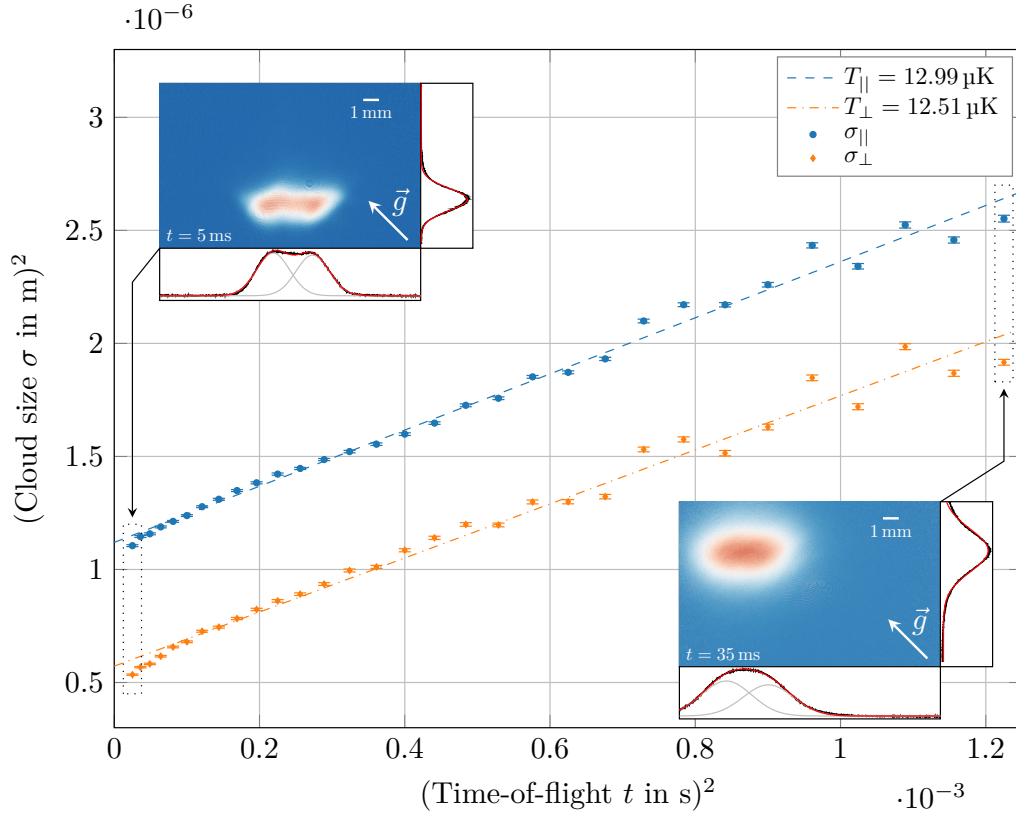
Figure 4.7: Temperature determination after sub-Doppler cooling. The atoms are released into free-fall and the size is recorded in the direction parallel ($\sigma_{||}$) and perpendicular ($\sigma_\perp$) to the grating after different times of flight. The inset images show absorption images at the beginning (top left) and end (bottom right) of the time of flight. Due to the non-Gaussian spatial distribution in the direction parallel to the grating, a single Gauss fit is not suitable. Instead, a fit with two adjacent Gaussians with identical σ is used which resembles the cloud shape very well. From the size evolution, the temperature $T = 12.75\,\mu$K is determined following equation 4.2.

This can easily be done by tracking the cloud expansion in a time-of-flight measurement thanks to the absorption detection system (see section 3.5.2). After time of flight, the Maxwell-Boltzmann velocity distribution of the atoms is mapped on the spatial distribution. Fitting a Gaussian envelope with width σ to the cloud after different times of flight t allows to deduce the size evolution

$$\sigma(t) = \sqrt{\sigma_0^2 + \sigma_v^2 t^2} \tag{4.1}$$

$$\iff \sigma^2(t) = \sigma_0^2 + \frac{k_B T}{m} t^2 \tag{4.2}$$

which depends on the temperature T. An exemplary series is shown in figure 4.7 where a temperature of about $13\,\mu$K was recorded with an average atom number of 4.7×10^8. As
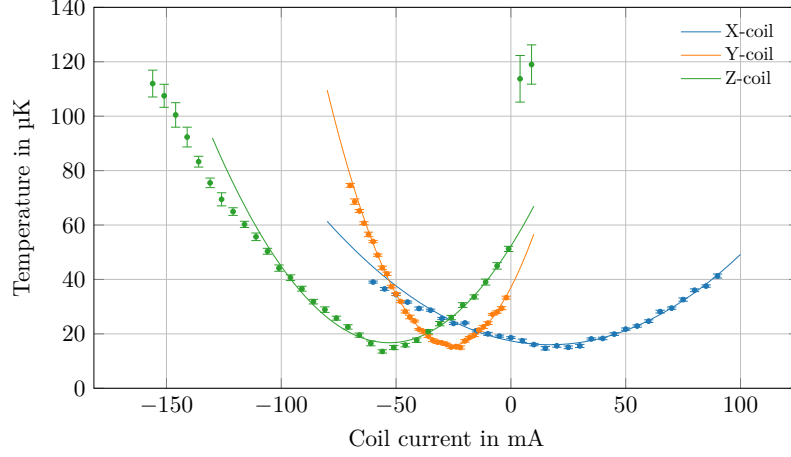
Figure 4.8: Determination of the compensation fields for sub-Doppler cooling. Magnetic fields applied during optical molasses compensate background fields which result in more efficient laser cooling that yields lower temperatures. The minimizing currents are found as $I_x = 16.9\,\text{mA}$, $I_y = -25.8\,\text{mA}$, $I_z = -52.9\,\text{mA}$ which can be converted into the magnetic field strengths $B_x = 52.4\,\text{mG}$, $B_y = -233.9\,\text{mG}$, $B_z = -293.1\,\text{mG}$ using the conversion factors of table 4.1.

it can be seen from the false-color inset images, the horizontal size of the cloud (parallel to the grating) is widened and does not constitute a Gaussian shape. This asymmetry in shape has been observed previously for grating-MOTs and stems from the different spring constants in the light force so that the shape becomes oblate for this diffraction angle [50]. Consequently, also the temperature was observed to be different in the perpendicular directions [19, 21, 50] though this effect is not visible here. This could be explained by higher atom number and densities which cause significant reabsorption of light that effectively mix the spatial directions. In addition, the cooling and trapping seems to distribute the atoms in a horizontal slab which is not point-like.

Fitting a single Gaussian envelope to this shape would greatly underestimate the temperature as the initial sizes would be overestimated in the fit. Instead, fitting two separate Gaussians with identical σ next to each other approximates the cloud shape very well (see inset images in figure 4.7). Since the temperature information lies within the size *evolution* σ_v, it can still be extracted with more consistent results.

The coil currents for the compensation of magnetic fields have been scanned to minimize the final cloud temperature. For every coil, the current is varied and the temperature is determined by a time-of-flight measurement (see figure 4.8). As a result, the compensation currents of $I_x = 16.9\,\text{mA}$, $I_y = -25.8\,\text{mA}$ and $I_z = -52.9\,\text{mA}$ are found to minimize the temperature of the cloud. These convert to the magnetic field strengths $B_x = 52.4\,\text{mG}$, $B_y = -233.9\,\text{mG}$, $B_z = -293.1\,\text{mG}$ using the results of the coil gauging measurement which is summarized in table 4.1.

4.4 Optical state preparation

After sub-Doppler cooling, the atoms are cold enough to be trapped in the magnetic trap. However, this relies on the atom being in the correct magnetic substate such as $|F = 1, m_F = -1\rangle$, $|F = 2, m_F = +1\rangle$ and $|F = 2, m_F = +2\rangle$ for ^{87}Rb, whereas the last one couples the strongest to magnetic fields. These states are low-field seeking, meaning that their energy is lowest in the minimum of a magnetic field. This property makes it possible to confine them in a magnetic field minimum and therefore trap them [44].

During the previous optical cooling sequence the atoms underwent various steps of optical pumping in combination with spontaneous emission and therefore the magnetic substates m_F are randomly distributed. Atoms not in the states mentioned above will instead be anti-trapped and are expelled from the trap with the exception of the $m_F = 0$ states which do not couple to magnetic fields to first order. Transferring atoms in the $|F = 2, m_F = +2\rangle$ state will therefore increase the yield of magnetic trapping.

A common method used to prepare the magnetic substate is optical pumping with circularly polarized light as illustrated in figure 4.9. Whenever an atom absorbs from the light field, it is transferred into the excited state changing its substate by $\Delta m_F = +1$. In the following spontaneous emission, the atom may decay back within three channels with $\Delta m_F = -1, 0, +1$. Whenever $\Delta m_F = 0$ or $\Delta m_F = +1$ is realized, which is more probable than $\Delta m_F = -1$, the optical pumping has advanced and the cycle begins anew until all atoms reach $|F = 2, m_F = +2\rangle$.

In comparison to laser cooling, where the $|F = 2\rangle \rightarrow |F' = 3\rangle$ transition is used, the optical state preparation operates on the $|F = 2\rangle \rightarrow |F' = 2\rangle$ transition. This is because the transition becomes dark once the atoms have reached $|F = 2, m_F = +2\rangle$ since no $|F' = 2, m_{F'} = +3\rangle$ excited state exists. This prevents excessive heating and acceleration of the cloud as the atom-light interaction is stopped once the final state is reached.

In the experimental realization, a light pulse is generated by switching the frequency of a detuned acousto-optical modulator to the correct modulation frequency for a set amount of time. This changes the beam deflection during the pulse so that light couples into a polarization-maintaining single-mode fiber. After the fiber, the light passes a quarter waveplate shifting the polarization from linear to circular in order to drive only σ_+ transitions. This requires the light to be shined in exactly parallel along a magnetic field as any residual projection $\vec{k} \cdot \vec{B} \neq k \cdot B$ would drive π transitions ($\Delta m_F = 0$) which would not be dark towards the final state. Therefore, the gMOT collimator is not suited for the task as the diffracted secondary beams provide no parallel beams. Instead, the detection light is used which also provides circularly polarized light and the magnetic field can be aligned accordingly by the external bias coils. The parameters for optical pumping were scanned to optimize the number of atoms transferred into a subsequent magnetic trap. A magnetic field of 4.96 G has been applied along the light propagation axis which was found to work well in previous experiments [62, 80]. Scanning the light frequency (figure 4.10a) reveals a singular maximum in the transferred number of atoms for a blue detuning of 7.1 MHz towards the calculated $|F = 2, m_F = 0\rangle \rightarrow |F' = 2, m_{F'} = 0\rangle$ transition. Here, a factor of ≈ 2.1 more atoms are transferred into the magnetic trap as compared to the off-resonant case in which no significant pumping is applied.

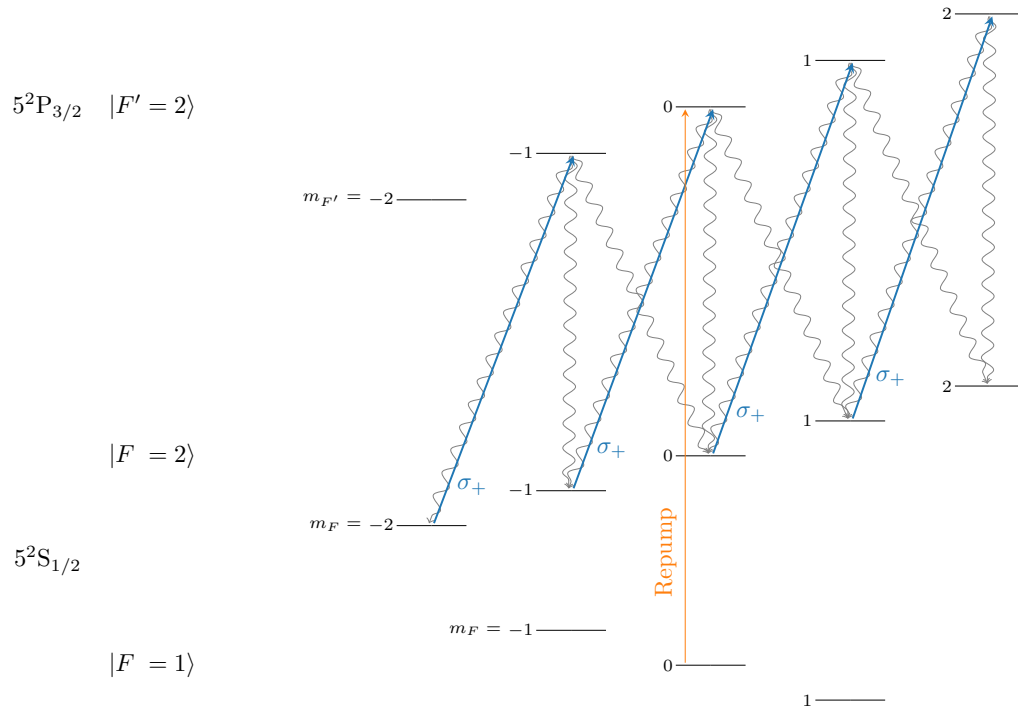**Figure 4.9:** Schematic of optical pumping on the $|5^2S_{1/2}F = 2\rangle \to |5^2P_{3/2}F = 2\rangle$ transition in ^{87}Rb with circular polarized light driving σ_+ transitions (blue). Vertical displacement of the states corresponds to energy level shifts (not to scale) due to the Zeeman effect by an applied magnetic field. The light drives optical transitions with $\Delta m_F = +1$ from where the atom may decay back into magnetic substates with $\Delta m_F = 0, \pm 1$. Whenever $\Delta m_F \neq -1$ is realized, the pumping advances until all atoms have accumulated in the $|F = 2, m_F = +2\rangle$ state which is dark to this transition. Repump light (orange) transfers back any atoms that have decayed into the $|F = 1\rangle$ manifold for which not all possible transitions are shown.

For the pulse duration and intensity, a plateau is observed after either sufficient intensity or sufficient pulse duration was applied (figure 4.10b). Higher intensities or longer pulses do not increase the number of transferred atoms anymore which is a clear indication that the atom-light interaction stops and the scheme is implemented well. To shorten the sequence, the pulse duration is kept at $\tau = 400\,\mu\text{s}$ with intensities above $1\,\text{mW/cm}^2$.
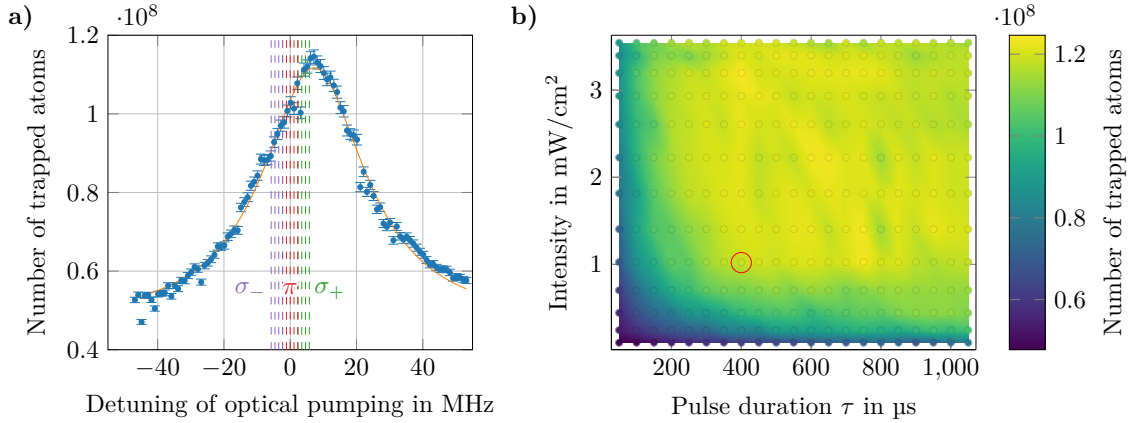
Figure 4.10: Measurement of parameters in the optical state preparation. **a)** The detuning of the pumping light is scanned around the $|5^2S_{1/2}F = 2\rangle \rightarrow |5^2P_{3/2}F = 2\rangle$ transition and the population in the subsequent magnetic trap is observed. Pumping with a detuning of $+7.1\,\text{MHz}$ yields the highest gain enhancing the atomnumber by a factor ≈ 2.1. Calculated transition frequencies for σ_- (purple), π (red) and σ_+ (green) transitions are shown as dashed lines. **b)** Variation of pulse duration and light intensity shows a broad saturation plateau once enough intensity has been applied for a sufficient time. Further increase in either intensity or time keeps the number of atoms constant indicating that all atoms have accumulated in $|F = 2, m_F = +2\rangle$ and atom-light interaction is stopped. The red circle indicates the final point of operation at $\tau = 400\,\mu\text{s}$ with intensities above $1\,\text{mW/cm}^2$. All measurements have been performed with a magnetic field of $4.96\,\text{G}$.

4.5 Magnetic trapping

With the atoms' internal state prepared, magnetic trapping is performed. The trap is formed by using the mesoscopic H-wires together with the outermost Z-structure on the Base-Chip in combination with an external bias field (see section 2.2.2). While the currents in the mesoscopic wires and the Base-Chip are operated at their maximum permissible value of $10\,\text{A}$ and $5\,\text{A}$ respectively, the external fields are used to steer the position and depth of the trap.

Briefly, the field in Y-direction sets the position of the magnetic field minimum in terms of distance from the central wire. This affects mostly the trap depth and trap frequency in the strong axes where closer positions cause deeper confinement with higher trap frequencies (see figure 4.12). Applying a field in Z-direction then rotates the minimum around the central wire on a circular trajectory so that together they determine the location of the field minimum. This way, a Ioffe-Pritchard type magnetic chip trap is formed with a natural non-zero magnetic field component in the minimum which points in X-direction. This so-called *trap bottom field* is caused by the parallel currents in the outside regions of the Z/H-wires and can be modified by applying an external field in X-direction. By changing the direction of the applied field, the trap bottom can be either lowered or increased. Lowering it transforms the trap towards a quadrupole trap with steeper curvatures thus increasing the trap frequency and trap depth. Increasing it flattens out the curvature and therefore lowers the trap frequency while also limiting the trap depth. Overall, a non-zero
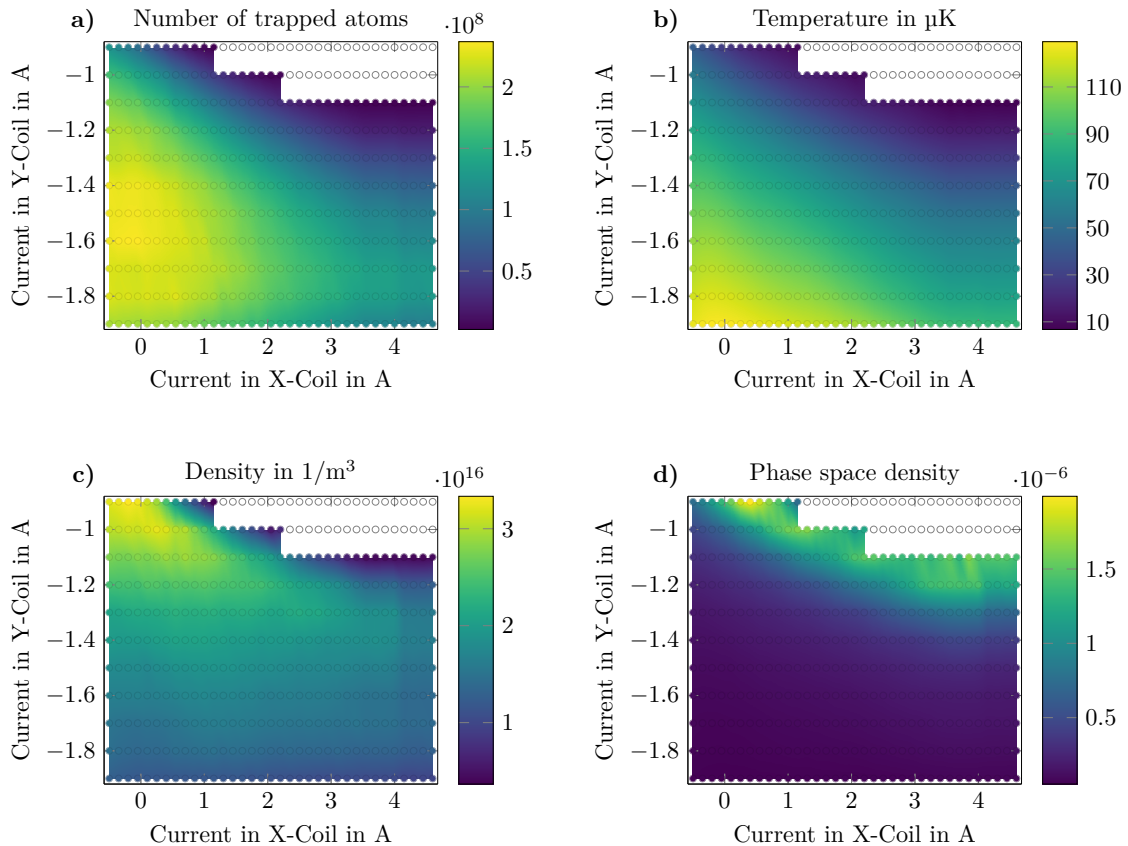
Figure 4.11: Measurement of the transfer of atoms into the magnetic trap for various external fields applied through the X- and Y-coils. While stronger currents in the Y-coil mostly form closer and stronger traps, the current in the X-coil determines mostly the trap bottom. For shallow traps (low I_y), an elevated trap bottom (medium to high I_x) lowers the trap depth until no atoms can be trapped anymore (white shaded areas). The traps are loaded after optical state preparation and the atoms are held 150 ms for thermalization before they are released into a time of flight measurement to determine the temperature. The maximum number of atoms (**a**)) transferred is 2.4×10^8 for a steep trap though the temperature (**b**)) increases. In contrast, higher densities (**c**)) and phase space densities (**d**)) are achieved for shallower traps with the highest phase space density of 1.8×10^{-6}. Figure 4.12 shows the magnetic field simulation of the corresponding magnetic traps.

trap bottom is preferable to avoid Majorana losses [81], but excessive values reduce trap frequency and depth. The X-field therefore plays an important role in shaping the magnetic trap.

The influence of the external fields in X- and Y-direction has been studied for the transfer of atoms into the magnetic trap (figure 4.11) with corresponding magnetic trap simulations[1] (figure 4.12). After optical state preparation, the respective trap is switched

---

1 For details about the magnetic field simulations see Appendix A.3.
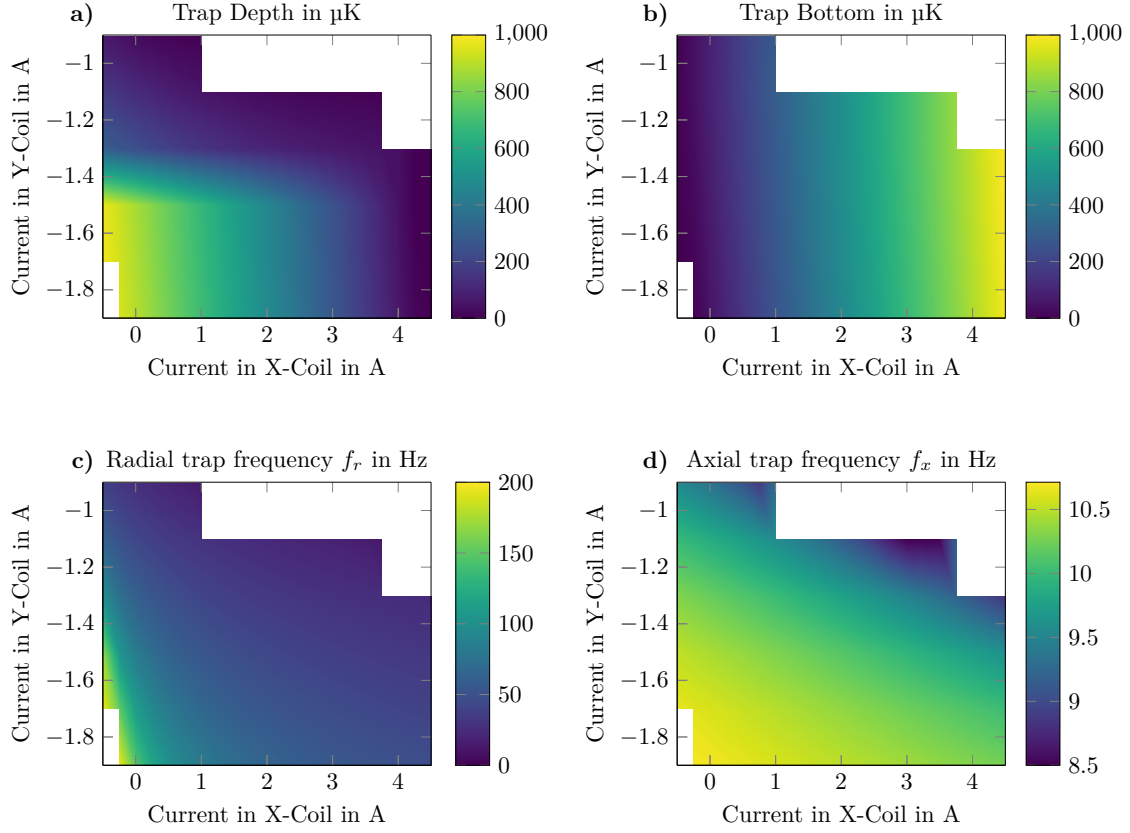
Figure 4.12: Simulation of the magnetic trap properties applied in figure 4.11. For every current combination, the magnetic field minimum is found, in which the Eigensystem of the trap is determined. The trap is analyzed in terms of trap depth **a)**, trap bottom **b)** and trap frequencies in the radial **c)** and axial **d)** direction. The trap depth and -frequency increase with larger $|I_y|$ which is counteracted by lifting the trap bottom by increasing I_x. While the trap frequency in the radial direction f_r can be strongly tuned using the bias fields, the axial frequency f_x is mostly unaffected staying around $10\,\mathrm{Hz}$. White shaded areas indicate parameter combinations where either no minimum could be found due to vanishing trap depth (top-right corner) or the trap is not harmonic anymore, i.e. is in the quadrupole regime where the trap frequency has no meaning (bottom-left corner). For details regarding the simulation see appendix A.3.

on and the atoms are held in it for $150\,\mathrm{ms}$ to rethermalize. Afterwards, they are released to record a time-of-flight series from which the temperature T, atom number N and sizes σ_y, σ_z are deduced. These values are taken to calculate the density

$$n \equiv \frac{N}{V} = \frac{N}{(2\pi)^{3/2}\,\sigma_x \sigma_y \sigma_z} \tag{4.3}$$

and phase space density

$$\text{PSD} = n\Lambda^3 = n\left(\hbar\sqrt{\frac{2\pi}{mk_\text{B}T}}\right)^3 \tag{4.4}$$

where Λ is the thermal de Broglie wavelength. Here, σ_x is aligned along the detection axis and can not be observed experimentally. It is therefore determined from the harmonic oscillator length $\sigma_x = \frac{1}{2\pi f_x}\sqrt{\frac{k_\text{B}T}{m}}$ with the simulated axial trap frequency f_x.

While the maximum number of transferred atoms peaks at 2.4×10^8 for traps with strong confinement, the corresponding temperature is high and therefore the phase space density remains low. In contrast, the highest phase space densities around 1.8×10^{-6} are achieved for shallower traps although containing less atoms ($\sim 1 \times 10^8$). This is plausible as optimum mode matching is achieved when the phase space density of the molasses-cooled ensemble is maintained during the transfer into the magnetic trap [14]. Assuming a normally distributed ensemble with sizes σ_i and temperature T, the optimum trap frequencies f_i of the magnetic trap in direction $i = \text{x,y,z}$ are [14]

$$f_i = \frac{1}{2\pi\sigma_i}\sqrt{\frac{k_\text{B}T}{m}} \tag{4.5}$$

where m is the mass of the atom. Given the size and temperature found for sub-Doppler cooling in section 4.3, the optimum trap frequencies would be

$$(f_\text{x}, f_\text{y}, f_\text{z}) = (5.2, 5.2, 7.5)\,\text{Hz}, \tag{4.6}$$

which is unfeasible under the influence of gravity. These traps would be extremely shallow and trap only a small amount of atoms. Aiming towards evaporative cooling, a trade-off needs to be made between high initial phase space density and a reasonable number of atoms. Finally, the evaporation efficiency will decide if it is more efficient to start either with a high phase space density and low number of atoms or to evaporatively cool a larger number of atoms towards a high phase space density.

4.6 Magnetic trap lifetime

Once the atoms are trapped magnetically, they can not be held indefinitely as the *lifetime* of the trap is finite. Residual background atoms interact with the walls of the vacuum chamber and therefore have the energy scale of room temperature. Consequently, inelastic collisions will transfer sufficient kinetic energy onto an atom to leave the trap. This sets bounds for the experimental time available since the atoms will naturally disappear from the trap. Targeting evaporative cooling, the lifetime is therefore the natural timescale available.

The lifetime was analyzed for the magnetic traps investigated above. After state preparation, the trap was loaded and held for varying times t_hold at the end of which the atom number N was observed. Fitting an exponential decay model

$$N(t) = N_0 \cdot \exp\left(-t_\text{hold}/\tau\right) \tag{4.7}$$
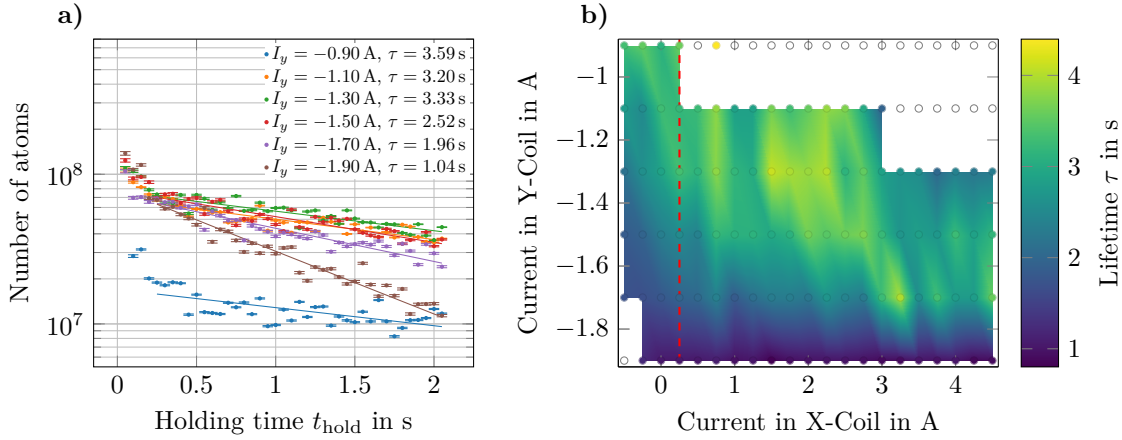
Figure 4.13:   Lifetime measurements of the magnetic trap. **a)** Atoms were held in the investigated magnetic trap for increasing durations t_{hold} during which the total number of atoms N declines exponentially. Fitting an exponential decay model $N(t) = N_0 \cdot \exp\left(-t_{\mathrm{hold}}/\tau\right)$ extracts the lifetime τ. The fits are restricted to start from $t_{\mathrm{hold}} = 250\,\mathrm{ms}$ to wait for the initial dynamics to settle. These exemplary datasets are taken with $I_x = 0.25\,\mathrm{A}$ as indicated by the red dashed line in **b)**. Overall, the lifetime is fairly constant around $3\,\mathrm{s}$ however for stronger Y-currents (closer and tighter traps), the lifetime decreases to less than $1\,\mathrm{s}$.

to the recorded curve, the lifetime τ is extracted (see figure 4.13). The fits are restricted to only start from $t_{\mathrm{hold}} = 250\,\mathrm{ms}$ to wait for the initial dynamics to settle where weakly bound atoms still leave the trap. It was found that in general the lifetime is fairly constant around $3\,\mathrm{s}$ though for stronger Y-currents (closer and tighter traps), the lifetime decreases to less than $1\,\mathrm{s}$.

Overall, these lifetimes are similar to what has been observed in comparable atom chip systems, though on an absolute scale they are not great. This demands comparably fast experimental times when working with the magnetic trap.

4.7 Evaporative cooling

Evaporative cooling relies on selectively removing atoms with above-average energies from the trap. Upon atom-atom collisions, the energy in the ensemble is redistributed and it rethermalizes to a lower temperature. For magnetic traps, the removal mechanism is conveniently achieved by applying a radio frequency (RF) field that couples the m_F states with each other to transfer atoms from a trapped to an untrapped magnetic substate which is expelled from the trap. By changing the radio frequency of the field, different energy levels can be addressed where higher frequencies are resonant to regions with stronger magnetic fields due to the Zeeman effect. These regions are occupied by atoms with higher energies. This way, the RF field limits the occupied energy levels up to a cut-off energy which is often referred to in multiples η of the thermal energy $k_{\mathrm{B}}T$, i.e. $\eta k_{\mathrm{B}}T$. This so-called truncation parameter η determines the fraction of atoms that is removed from the trap. As the process goes on and the temperature decreases, also the frequency of the RF field has to be reduced in order to keep η constant.

A crucial process in this procedure is the rethermalization through elastic collisions: As atoms with higher energies are removed from the trap, there is no occupation of these energies until collisions recreate the far end of the Maxwell-Boltzmann distribution. Studies have found, that about five collisions per atom are necessary until the velocity distribution is indistinguishable from thermal equilibrium [82–84]. Therefore, the process depends on the elastic collision rate Γ_{el} of atoms in the trap which is proportional to the number of atoms N, the product of trap frequencies $\omega_x \omega_y \omega_z$ and anti-proportional to the temperature T (cf. equation 1.4).

However, not all collisions are beneficial: As discussed in the previous section, background gas collisions may randomly remove atoms from the trap occurring with a rate $\Gamma_{bg} = \tau^{-1}$. The expelled atoms have a random energy and thus do not contribute to cooling thus lowering the phase space density. In addition, 3-body collisions may lead to loss of atoms. These occur mostly in regions with higher densities and are therefore predominantly found in the center of the trap where low-energy atoms gather. This is fundamentally different to background gas losses, as atoms with energies below the average energy are lost which opposes the cooling process and has to be avoided at all cost. Luckily, these occur mostly at higher densities $\sim 1 \times 10^{14}\,\mathrm{cm}^{-3}$ [85] late in the cooling process and can be avoided by appropriate trap decompression [14]. In the beginning of evaporative cooling, the three-body losses Γ_{3b} can usually be neglected.

In addition to these effects, atoms may also leave the trap if they undergo Majorana spin flips to an untrapped magnetic substate happening at a rate Γ_m. This can occur, when the magnetic moment of the atom which processes at the Lamor frequency $\omega_L = \mu B/\hbar$ is unable to follow the instantaneous angular frequency of the trap [86] which generally happens for vanishing magnetic fields. Therefore, a non-zero trap bottom field has to be maintained to avoid these losses. In practice, a value of $B \approx 0.5\,\mathrm{G}$ is used to make sure it is above Earth's magnetic field under all orientations.

Overall, the ratio between intended elastic collisions and unwanted lossy collisions

$$R = \frac{\Gamma_{el}}{\Gamma_{loss}} = \frac{\Gamma_{el}}{\Gamma_{bg} + \Gamma_{3b} + \Gamma_m} \tag{4.8}$$

has to be considered [14, 42]. When appropriate measures are taken, the three-body collision rate Γ_{3b} and Majorana losses Γ_m can be neglected and the collisional ratio becomes

$$R \approx \frac{\Gamma_{el}}{\Gamma_{bg}} = \Gamma_{el} \cdot \tau = \frac{8\sqrt{2}a^2 m}{\pi k_B} \frac{N\bar{\omega}^3}{T} \cdot \tau. \tag{4.9}$$

In general, one wants this ratio to be as high as possible to maximize the elastic collision rate while having minimal losses. If all parameters can be chosen freely, then maximizing the trap frequencies while maintaining high atom number, low temperature and long lifetimes is key to increase R. The value of R has been calculated in figure 4.14 a) for the investigated parameter space of the previous sections, taking into account the measured values of N, T, τ and simulated values $\bar{\omega}$. It becomes maximal for a relatively tight trap around $I_y = -1.9\,\mathrm{A}$ with a minimal permissible trap bottom field reaching $R = 136$.
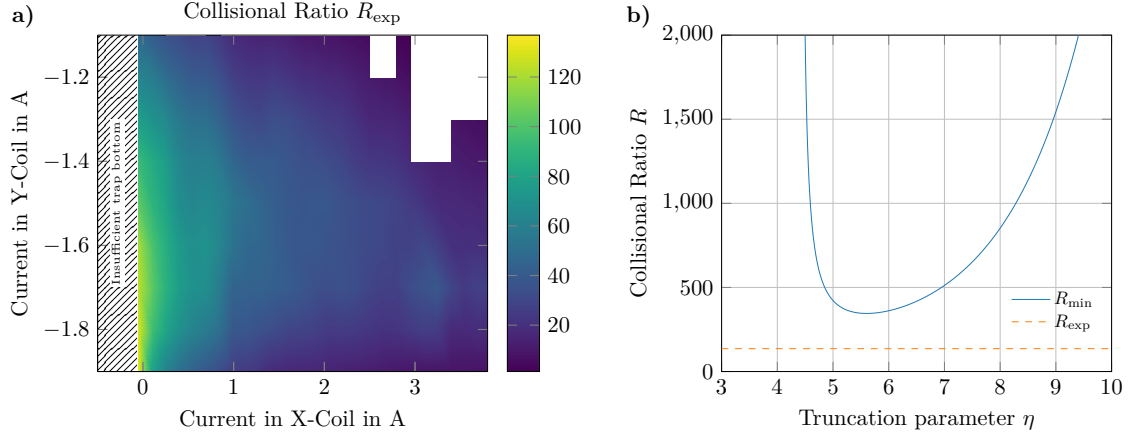
Figure 4.14: Determination of the collisional ratio R as the ratio of intended elastic to lossy collisions. **a)** Neglecting other loss mechanisms, the collisional ratio is calculated as $R = \Gamma_{\mathrm{el}} * \tau$ as an upper bound using equation 4.9 for the characterization results gathered in the previous sections. Taking into account a minimum required trap bottom field for evaporative cooling of $0.5\,\mathrm{G}$, the maximum achievable collision ratio is limited to about 136. **b)** Plot of the minimum required value R_{min} (equation 4.10) depending on the choice of the truncation parameter η during evaporative cooling as presented in [14]. The experimentally achievable value lies well below the minimum required collisional ratio.

While $\bar{\omega}$ and τ are generally constant for a given trap, N and T naturally do change over the course of the evaporative cooling sequence and thus R may increase or decrease depending on the evaporation efficiency, i.e. the reduction of temperature T per loss in atom number N. When R decreases, the cooling becomes less efficient and ultimately stops. A criterion to work with is therefore the requirement for R to increase or remain constant over the duration of the cooling sequence. This is the case for

$$R \geq R_{\mathrm{min}} = \frac{\lambda(\eta)}{\alpha(\eta) - 1} \tag{4.10}$$

where $\lambda(\eta)$ is the ratio between the time constant of the evaporation and the elastic collision time and $\alpha(\eta)$ is the ratio between a change in temperature and change in atom number [14]. Both quantities depend only on the truncation parameter η and expressions for them can be derived from incomplete Gamma functions [14, 42, 87]. The minimum required collisional ratio has been plotted in figure 4.14 b) over the truncation parameter. Unfortunately, the experimentally measured value lies well below the minimum required curve. It is therefore to be expected that the evaporative cooling will not work well in the available parameter space which is mostly prohibited by insufficient lifetime τ and low trapping frequencies $\bar{\omega}$. Nevertheless, I attempted evaporative cooling in this setup.

4.7.1 Evaporative cooling implementation

In the experimental implementation of evaporative cooling, the atoms are directly captured in the trap of highest R since lengthy transfer sequences between various magnetic traps was found to be ineffective in the presence of low lifetimes. This configuration uses $I_H = 10\,A$, $I_{BC\text{-}Z} = 5\,A$, $I_x = -200\,mA$, $I_y = -1.9\,A$ and $I_z = -50.9\,mA$ to generate a trap bottom field of $465\,mG$ at a trap depth of $672\,\mu K$ and trap frequencies of $(\omega_x, \omega_y, \omega_z) = 2\pi\,(10.7, 205, 206)\,Hz$ (all simulated values).

The direct loading excites oscillations in the trap since its position is closer to the chip than the atomic cloud. An initial holding time of $51.1\,ms$ is used to allow for some of the initial dynamics to settle before a radio frequency field is applied to decouple atoms. As the radio frequency is swept towards lower values, atoms are removed from the trap and colder temperatures, smaller sizes, higher densities as well as higher phase space densities should be observed. A time of flight measurement with $t_{TOF} = 1 \ldots 9\,ms$ was taken for every frequency ramp to determine the temperature. Compared to the molasses-cooled cloud, the temperature is strongly increased due to the trap compression which leads to a significant cloud expansion even after these short times of flight. Together with the deforming trap excitations along the direction perpendicular to the chip (vertical direction in figure 4.15a), temperature estimation becomes difficult. Therefore, the temperature is estimated from the 1D expansion behavior parallel to the chip surface (horizontal direction in figure 4.15a) which is mostly unaffected.

First evaporation ramp

Figure 4.15 shows this procedure where the radio frequency starts at $12\,MHz$ and is swept to the indicated target frequency $f_t = 12 \ldots 6\,MHz$ over a duration of $70\,ms$ where it is held for an additional $20\,ms$. Starting from $f_t \approx 10\,MHz$, atoms are removed from the trap and both the temperature and the size decrease initially. Meanwhile, the density and phase space density begin to increase. At $f_t \approx 9\,MHz$, the temperature shows a minimum where also the phase space density increases to a maximum. This increase in phase space density is a clear indication of evaporative cooling though the following increase in temperature is untypical (see below). The evaporation efficiency is defined as

$$\gamma \equiv -\frac{d\log(PSD)}{d\log(N)} = -\frac{\log(PSD) - \log(PSD_0)}{\log(N) - \log(N_0)} = -\frac{\log(PSD/PSD_0)}{\log(N/N_0)} \tag{4.11}$$

which is the gain in phase space density (PSD) per atom loss N. Positive values indicate a net gain in phase space density while negative values mean an effective loss. To calculate the derivative in a numeric approximation, one needs to define the reference values PSD_0 and N_0: For this data set, these have been calculated as the mean values $PSD_0 = \langle PSD \rangle$ and $N_0 = \langle N \rangle$ in the frequency range $f_t = 10.5 - 12\,MHz$ where no removal of atoms was observed. Therefore, the error bars in figure 4.15f are relatively large as $\log(N/N_0) \to 0$ when the atom number fluctuates. Nevertheless, γ is positive around $f_t = 9\,MHz$.

Second evaporation ramp

Following the previous optimum, a subsequent evaporation ramp was applied (figure 4.16). Starting from $9\,MHz$, the target sweep frequency was scanned towards $6\,MHz$ but this
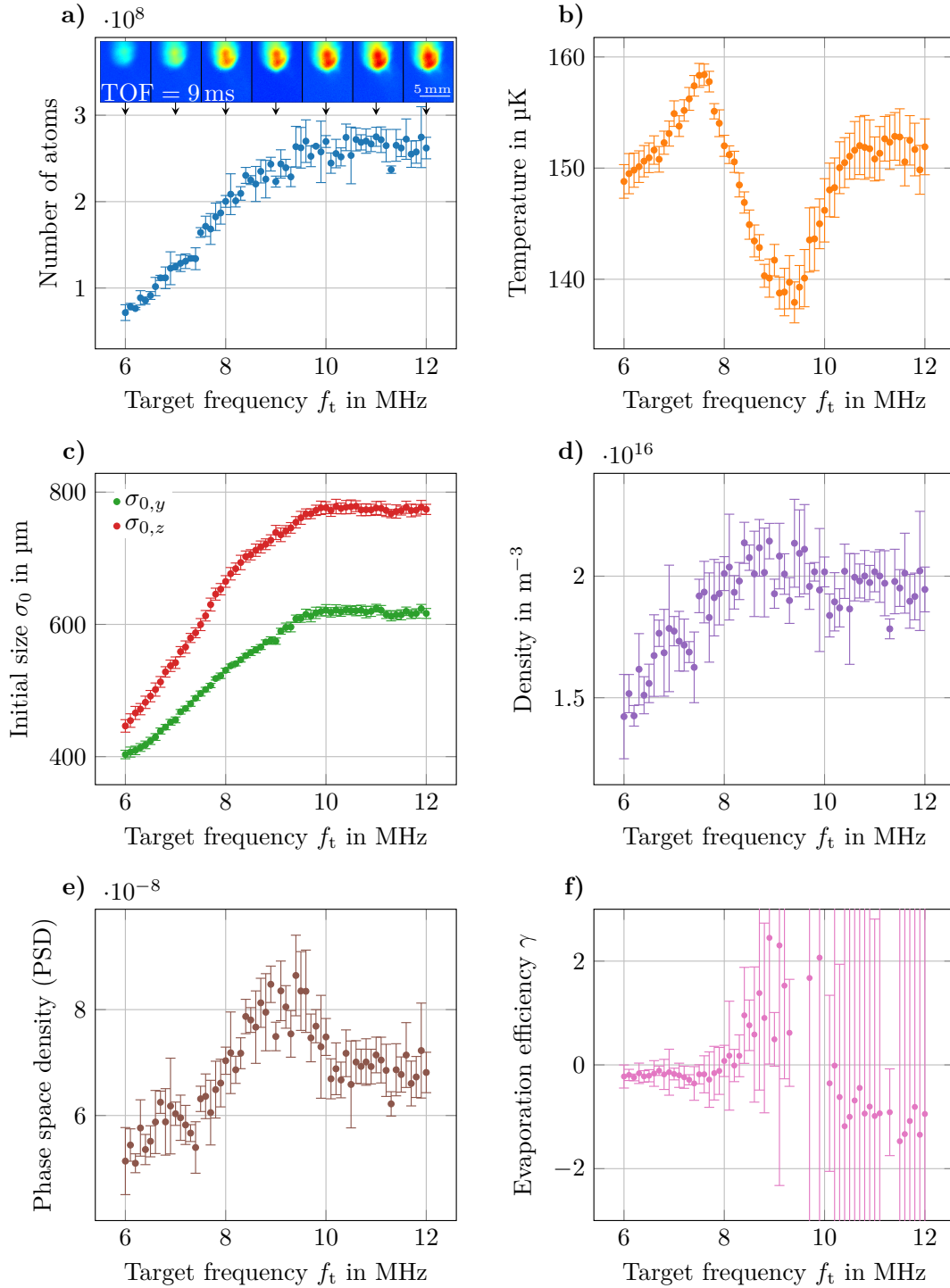
Figure 4.15: Evaporative cooling in a trap with the highest available trap frequencies $(\omega_x, \omega_y, \omega_z) = 2\pi (10.7, 205, 206)$ Hz at $I_y = -1.9$ A. After a holding time of 51.1 ms, the radio frequency is swept from 12 MHz to the target frequency f_t over a duration of 70 ms where it is held for an additional 20 ms. As the frequency approaches the occupational energy around 10 MHz, atoms are removed from the trap (**a)**) and the temperature (**b)**) and initial size (**c)**) drop. Around $f_t = 9$ MHz, the density (**d)**) and phase space density (**e)**) increase which demonstrates evaporative cooling. However, the evaporation efficiency (**f)**) is relatively low around $\gamma \approx +1$ where the mean atom number and phase space density of the first 15 data points $(10.5 - 12$ MHz) was taken as a reference. Here, the error is mostly dominated by fluctuations in the atom number.
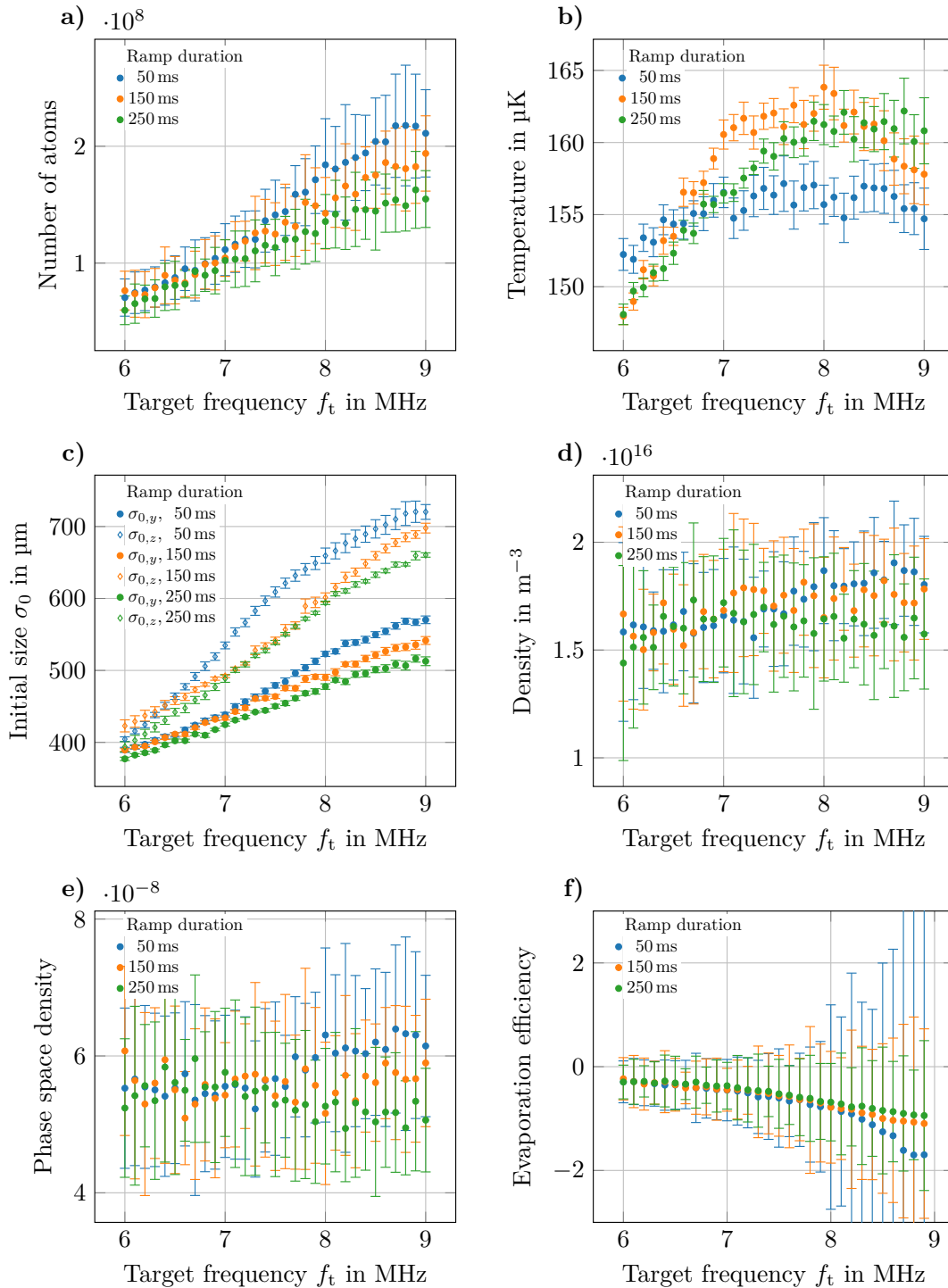
Figure 4.16: Following the first evaporative cooling ramp (figure 4.15), this subsequent ramp continues to sweep the radio frequency from 9 MHz to f_t where also the ramp duration is varied between $50 - 250$ ms. The initial atom number (**a)**) drops further due to the extended overall ramp duration in the presence of the non-negligible lifetime of the trap. As the frequency is swept, the temperature (**b)**) decreases only for lower f_t values as previously observed. Even though the size (**c)**) decreases, the density (**d)**) and phase space density (**e)**) do not increase and the evaporation efficiency (**f)**) stays negative with respect to the previous ramp.

time the sweep duration was adjusted between $50 - 250\,\mathrm{ms}$ as an additional parameter. Notably, the trap lifetime diminishes the atom number for longer sweep times (4.16a) and the temperature is increased (4.16b). This is easily observed in the first data point ($f_\mathrm{t} = 9\,\mathrm{MHz}$) which effectively acts as an additional holding time since the frequency is not adjusted over the course of the ramp. While further removal of atoms does decrease the temperature as previously observed, the corresponding (phase space) density does not increase significantly and the evaporation efficiency stays negative with respect to the previous frequency ramp. In comparison to the first ramp, where about $15\,\mathrm{\mu K}$ temperature reduction was observed at marginal atom loss, the cooling efficiency seems to be much lower here. This could be caused from insufficient replenishment of the truncated energy distribution and/or a combination with sources of heating.

Heating observation

The sudden temperature increase in the frequency ramp is an untypical behavior in evaporative cooling and is not to be expected from the theoretical model. A likely candidate to explain this feature is the prevalence of a smaller secondary cloud which overlays with the main cloud. This is slightly suggested by the absorption images (inset in figure 4.15a) though the shape is also strongly affected by trap oscillations. It may exist either from the beginning or is created during the evaporative cooling which could happen if the decoupling mechanism $|F = 2,m_F = +2\rangle \rightarrow |F = 2,m_F = +1\rangle \rightarrow |F = 2,m_F = 0\rangle \rightarrow |F = 2,m_F = -1\rangle \rightarrow |F = 2,m_F = -2\rangle$ is incomplete and leaves atoms in $|F = 2,m_F = +1\rangle$. In this case, the decoupled atoms would remain as a hot bath for the primary cloud since their average energy is higher. In the beginning of the cooling, the expansion of the secondary cloud would remain hidden within the primary cloud size. As the cooling goes on, the outer cloud is successively cooled and the overall expansion behavior shifts to become dominated by the hotter inner cloud which results in an observed higher temperature. Once the RF-knife reaches lower frequencies, also the inner cloud is evaporatively cooled which explains the final temperature drop after the maximum. In the second ramp this behavior is also visible for all ramp durations. This secondary cloud may lead to an overestimation of the temperature though the cooling efficiency is also low at lower radio frequencies.

As an alternative approach, one might try to use microwave evaporation which decouples $|F = 2,m_F = +2\rangle$ into the anti-trapped $|F = 1,m_F = +1\rangle$ state though this requires a tunable frequency source at $f \approx 6.8\,\mathrm{GHz}$ which was not readily available at the experiment. Further investigations are required on this matter.

Conclusion

In conclusion, minor evaporative cooling was observed, though the efficiency seems to drop rapidly. The secondary evaporation ramp could not reduce the temperature significantly so that the phase space density would rise. Even in the presence of additional heating sources, the cooling seems to be very low which would be explained by vanishing re-thermalization due to insufficient elastic collisions and low lifetimes. The setup simply lacks the ability to generate high frequency magnetic traps which is not surprising given that the topmost atom chip layer has been replaced by a simple grating substrate without electrical circuits.

These results underline the necessity to build an atom chip featuring both the wires for

high-frequency magnetic traps *and* a nano structure suitable for magneto-optical trapping. Further developments to manufacture such chips are detailed in the Outlook (chapter 5).

4.8 Coil calibration using RF spectroscopy

Good knowledge of the experimental setup is vital to model experimental observations in a computer simulation. When working with atom chips, experimental investigations are often accompanied by magnetic field simulations due to the complexity of how the total magnetic field is generated. Typically, one field component is generated by the chip fields while the other one is generated by external coils. While the chip has well-defined structures known to good accuracy, the external fields are generated by pairs of Helmholtz-coils that are mounted around the chamber. Inaccuracies in winding number, position uncertainties or tilts will affect the amount of magnetic field generated by the coils. A coil calibration of the current-to-field transfer function helps to match the simulations well with experimental observations.

Measuring the field of the coil assembly in the final setup with a classical magnetic field sensor is intrinsically difficult because it is hard to place it in the center of the vacuum chamber with good position accuracy. Luckily, the atoms themselves are an excellent magnetic field probe. Using radio frequency (RF) spectroscopy on magnetically sensitive Zeeman states, the transition frequency between neighboring m_F states can be determined in dependence of the applied magnetic field.

The routine works as follows: The atoms are prepared into the $|F = 2, m_F = +2\rangle$ state and are trapped magnetically as described in the previous sections. After some holding time they are released and the external coil field is applied. At this point, the atoms are still in the $|F = 2, m_F = +2\rangle$ state. A RF pulse with frequency f_{RF} is applied to couple $|F = 2, m_F = +2\rangle \leftrightarrow |F = 2, m_F = +1\rangle$ transferring atoms between the states. After the interaction, the atoms still overlap spatially. In order to detect the relative population amplitude, a magnetic gradient field is applied by the atom chip exerting a differential magnetic force. After some time of flight, they separate and the relative amplitudes are found using absorption imaging. The field-dependent resonance frequency is then found by scanning f_{RF}. This frequency can be converted into magnetic field strength using the well-known Zeeman splitting of $g_F \mu_B / h \approx 700 \, \text{kHz/G}$ for ^{87}Rb. This way, the magnetic field that was present during the RF coupling can be determined. Repeating this for different currents in the coil, the coil factor in terms of generated field per applied current can be measured.

These measurements have been performed for all three coil pairs in positive and negative current direction (figure 4.17) and are summarized in table 4.1. Good agreement is found between the measured coil factor and previously modeled coils in the magnetic field simulation. In addition, the linear fit of the individual measurements provides the intersection points of the positive and negative diagonal where the magnetic field vanishes for the axis respectively. Calculating the field values for these currents, the total magnetic field $|B| = \sqrt{\sum_i B_i^2} \approx 487 \, \text{mG}$ is measured close to Earth's magnetic field of $494 \, \text{mG}$ as indicated by the German national metrology institute (Physikalisch-Technische Bundesanstalt, PTB) [88] which is located about $50 \, \text{km}$ away. The comparison to the field values found for

sub-Doppler cooling in section 4.3.1 $(B_x,B_y,B_z) = (52.4,-233.9,-293.1)\,\mathrm{mG}$ shows a good agreement in X- and Y-direction with a field deviation of $\Delta B_x = 16.4\,\mathrm{mG}$ and $\Delta B_y = 5.4\,\mathrm{mG}$ respectively. However, in Z-direction the deviation is more significant with $\Delta B_z 125.7\,\mathrm{mG}$ which indicates residual dynamic magnetic fields. This means that the sub-Doppler cooling is still operated in a phase where the background field changes which may diminish the cooling efficiency. Suppression of eddy currents may therefore play a vital role in attaining a greater experimental control over the atomic cloud to achieve lower temperatures and higher (phase space) densities.

Table 4.1: Result of the bias coil magnetic field characterization using positive and negative currents. The values were obtained using RF spectroscopy on magnetically sensitive Zeeman states (section 4.8). Magnetic field simulations predict the coil strength well. The intersections of the linear fits in figure 4.17 provide the compensation currents and the corresponding compensation fields needed to null the background field.

| Coil | Coil Factor in G/A | | | | Compensation | Compensation |
	Positive	Negative	**Mean**	Simulation	Current I_i in mA	Field B_i in mG
X	3.099	3.102	**3.101**	3.122	22.2	68.9
Y	9.058	9.071	**9.065**	9.106	-26.4	-239.4
Z	5.526	5.554	**5.540**	5.666	-75.6	-419.0
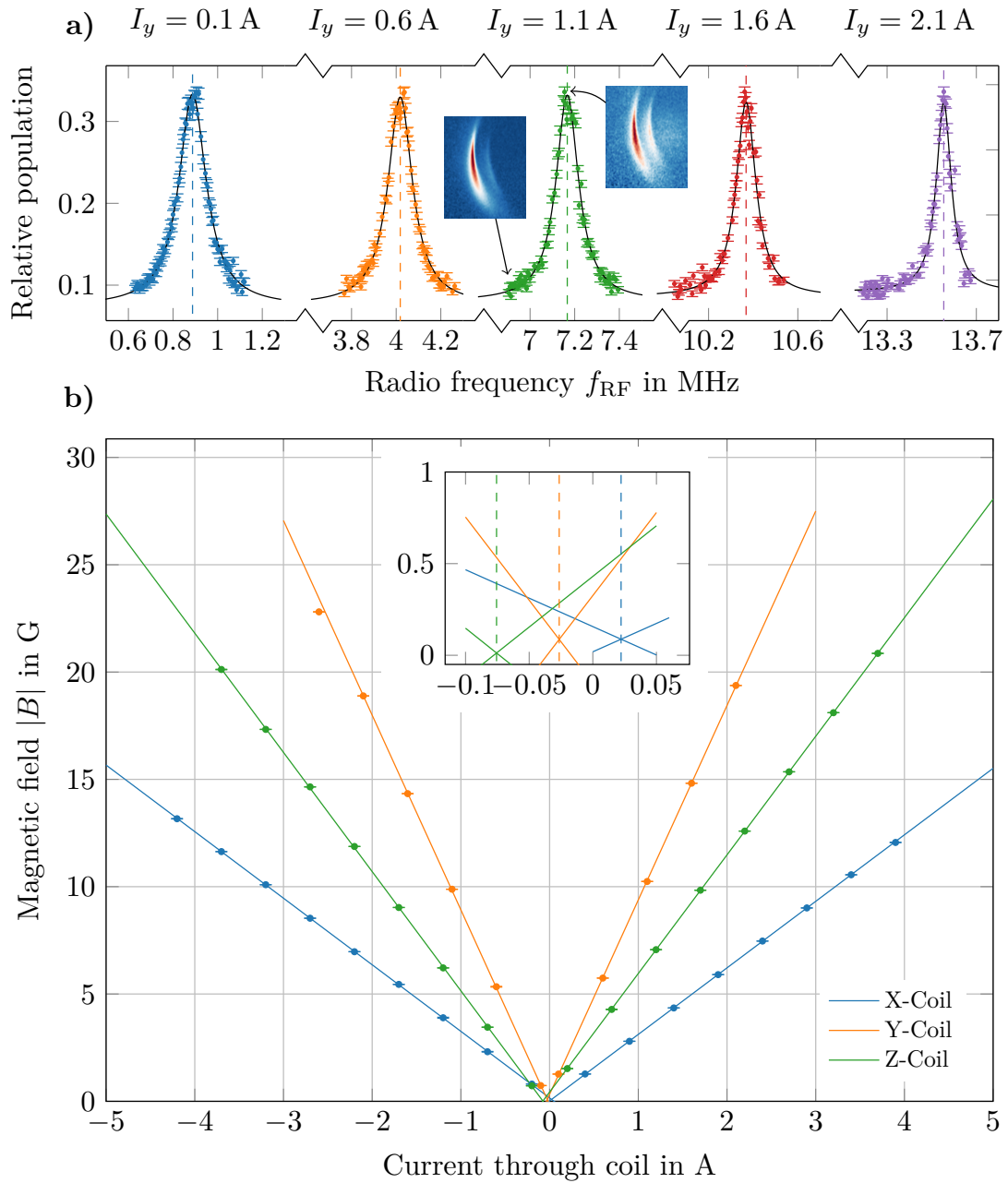
Figure 4.17: Bias coil characterization with radio frequency spectroscopy. An atomic ensemble of ^{87}Rb in the magnetically sensitive substate $|F = 2, m_F = +2\rangle$ is brought into the coil field. A radio frequency pulse couples the states $|F = 2, m_F = +2\rangle \leftrightarrow |F = 2, m_F = +1\rangle$ which are subsequently spatially separated in a magnetic gradient field. After time of flight, the relative amplitude between the states is read out using absorption imaging to find the field-dependent transition frequency. **a)** Exemplary resonance curves for the Y-Coil with positive current direction. The resonances are fitted using a Lorentzian line shape from which the magnetic field is calculated with the well-known Zeeman-splitting $g_F \mu_{\mathrm{B}}/h \approx 700\,\mathrm{kHz/G}$. **b)** A linear fit determines the coil factor in units of field per current as summarized in table 4.1. Inset: The intersections of the linear fits determine the current where the magnetic field is nulled for the respective direction of the coil.

CHAPTER 5

The future of atom chips

The previous pages have shown the combination of a single-beam grating magneto-optical trap with an atom chip. A large number of atoms could be trapped initially from a $2D^+$-MOT, they were laser cooled to low temperatures of $13\,\mu K$ and a significant fraction was transferred into a large-volume magnetic chip trap concluding the purpose of the investigated chip. Significant evaporative cooling towards quantum degeneracy was not possible since the elastic collision rate was too small in comparison to the lifetime of the magnetic trap which was to be expected from the design. Naturally, the next steps is thus to realize an atom chip that features a grating surface *and* wires for high frequency magnetic trapping to realize a single-beam atom chip BEC source.

5.1 Single-beam BEC atom chip

Merging the nano structure with wires for high frequency magnetic trapping is an engineering challenge. Our group has teamed up with the Institute of Micro Production Technology (IMPT) of our university to investigate the manufacturing of these chips. In our group's conventional atom chips, $10\,\mu m$ high wires were grown on a substrate and covered with a thin layer of epoxy to level the surface and hold a reflective transfer coating for a mirror-MOT. In comparison to the wires, the required nano structures are much smaller with a period of about $1\,\mu m$ and a depth of $\lambda/4 \approx 195\,nm$. They are commonly manufactured using electron-beam or laser lithography and thus require a flat surface to be applied. Consequently, the wires are blocking the surface and have to be embedded into the substrate.

Our concept relies on etched and isolated trenches in a silicon substrate into which the wires are grown. In a second step, any overgrown material is polished away to create a flat surface onto which the nano structure can be applied. Alternatively, this flat surface can also be used as the basis for a direct optical mirror coating that does not require glue to be applied. In addition to the planarized surface, the atom chip can also be improved in further aspects:

On the one hand, eddy currents played a major role in the shutdown sequence of the currents from the MOT phase. This lead to a complex sequence of light and current adjustments in
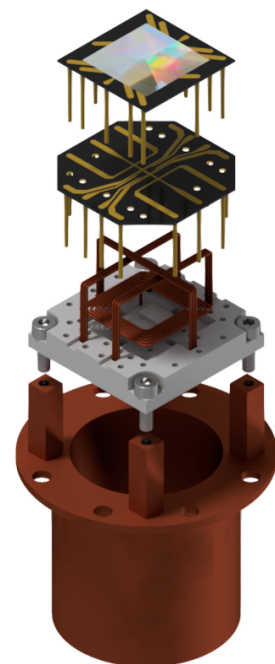
Fig. 5.1: Explosion view of the multi-layer single-beam BEC atom chip with an integrated nano structure on top.
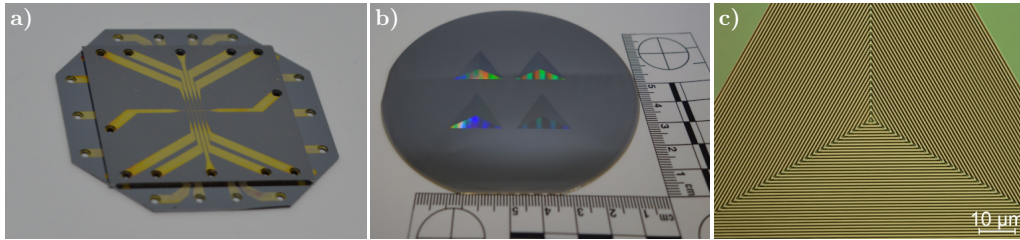
Figure 5.2: First results on atom chip and grating manufacturing by IMPT. **a)** Base- and Science Chips are bonded with transient liquid phase diffusion bonding. From here on, a grating or mirror coating can be applied. **b)** First results on grating manufacturing on a plain wafer. Four gratings have been manufactured side by side to calibrate the machines. **c)** Scanning electron microscopy image of the center of a manufactured grating. Image courtesy of IMPT.

which a large percentage of up to 60 % of the atoms are lost and the atomic cloud expands unnecessarily. This loss of (phase space) density can be regained via evaporative cooling later, but this comes at the cost of atom number and time which ultimately corresponds to a reduced signal-to-noise ratio and lower flux. **Suppression of eddy currents** thus helps to regain control over the magnetic fields and eases the laser cooling. This can be achieved by carefully placing slits in the copper mount to limit the extent of induced currents. However, they may not fully suppress them and limit heat distribution as well as mechanical stability. An alternative approach is to use electrically non-conducting materials for the chip mount such as ceramics with high thermal conductivity, e.g., [Shapal™]. These would completely suppress any eddy currents and feature full mechanical stability.

On the other hand, also the vacuum quality could be improved. Currently, the chip components are glued together using an UHV compatible epoxy [Epotek H77] which still has non-vanishing outgassing properties. This is suspected to lead to a locally high particle flow around the chip which diminishes the lifetime of the magnetic trap. **Avoiding all epoxies** in the atom chip assembly will thus improve vacuum quality and extend the lifetime of the magnetic trap which will ultimately yield more atoms in the BEC and lead to a higher flux. Instead of glue, mechanical clamping and bonding techniques can be used. In transient liquid phase diffusion bonding [89], two metallized surfaces are bonded together by diffusion of an intermediate metal layer. In particular, Gold and Indium provide an excellent combination [89] with a low process temperature around 200 °C. As such, the bonding surfaces can be covered in Gold while an Indium foil is used as an intermediate layer. First manufacturing results of IMPT show promising results on the diffusion bonding of two manufactured chips as well as on the manufacturing of nano structures (figure 5.2).

Taking into account these considerations, I have designed a next-generation atom chip which features embedded wires and an integrated nano structure as the top-most layer (figure 5.1). The mesoscopic wires are clamped into a ceramic mount and the chip layers are bonded together. With the outlined improvements above, a single-beam BEC atom chip can be realized with perspectives to reach an unprecedented high flux of ultra-cold quantum degenerate atomic ensembles.

5.2 Miniaturized BEC source

With the new single-beam BEC atom chip at hand, new possibilities for a compact and transportable BEC source will open up. The reduced requirements on optical access, number of optical components and alignment simplicity will allow to develop drastically miniaturized vacuum system concepts. The vacuum chamber requires only a single optical port opposite to the grating for atomic trapping and all additional ports are available for the scientific application. Shrinking the vacuum chamber will then benefit many of the subsystems:

- The surrounding bias coils will generate stronger fields for the same current requiring less power.
- The first lens in the detection system will need to have its focus at the center of the vacuum chamber. Reducing the chamber diameter thus allows to make use of shorter focal lengths with higher numerical apertures for better and smaller imaging systems.
- The outgassing of the vacuum chamber is in principle determined by the choice of materials, the inside surface area and the pumping speed. When proper materials are chosen, smaller vacuum chambers require smaller pumps which are also lighter.
- The science case will typically require a well-defined magnetic field environment. Consequently, a bulky magnetic shield is needed which will directly scale with the chamber dimensions.

As the atom chip part of the vacuum system is reduced in size, also the atomic source should be simplified. While a $2\mathrm{D}^{(+)}$-gMOT with a pushing beam has already been demonstrated [18], the implementation lacked adjustable power ratios between the pusher- and retarder beam which turned out to be a crucial parameter to adjust the flux. Adapting the $2\mathrm{D}^+$-MOT of this work to a $2\mathrm{D}^+$-gMOT thus seems to be a straightforward approach to further simplify the system. Overall, these steps will lead to a drastically miniaturized high-flux BEC source.

5.3 Extension to atom interferometry

While the miniaturized source would already be useful on its own to many fields of physics, the extension with atom interferometry opens up new possibilities for it to be used as a quantum sensor. A major drawback in replacing the mirror surface of the atom chip with a grating is that it is no more possible to retro-reflect interferometry light of the same wavelength as the zero order is suppressed by design. Several other options could be employed to complement the gMOT with atom interferometry:

One possibility would be to operate the interferometry on a perpendicular axis ignoring the grating features. The major challenge in this approach is that the atoms are quite close to the atom chip and the interferometry light would typically clip on the chip edge which gives rise to additional phase imprints due to diffraction of the light field [13, 91]. This can be circumvented by transporting the atoms to a sufficient distance which is possible with only minor trap excitations but this may be time-consuming and requires a high degree of experimental control [92].
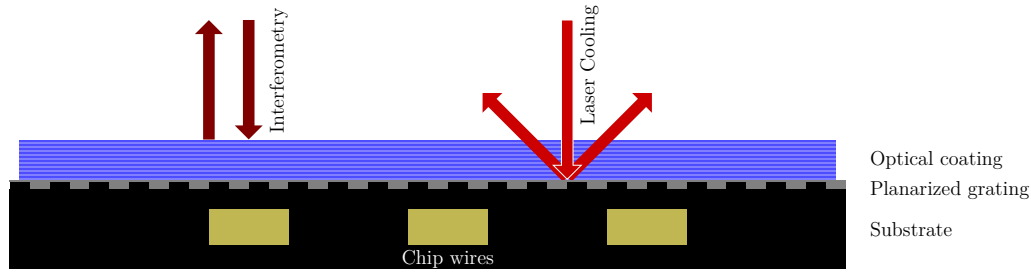
Figure 5.3:　Extension of the grating setup for atom interferometry using a wavelength-selective optical coating. The grating structure is planarized with a transparent thin-film onto which an optical coating is applied. The coating transmits the cooling light at the incident and deflection angle while it reflects the interferometry light before reaching the grating. For Rubidium, this could be cooling light at $\lambda_{D2} \approx 780\,\text{nm}$ and interferometry light at $\lambda_{D1} \approx 795\,\text{nm}$ though other wavelength combinations are possible. The substrate holding the structure may already contain atom chip wires to generate magnetic fields though this is not necessarily required depending on the application. This method has been filed as a patent [90].

If you limit yourself to the overlap volume of the diffracted light orders of the grating, one could apply atom interferometry using the different diffraction orders of the grating [93]. Interestingly, this directly provides effective light vectors in all spatial directions though the multitude of possible transitions in the presence of not well defined polarizations (cf. section 2.4, appendix A.1) may make it difficult to address the intended transitions correctly. Furthermore, the atoms would quickly drop out of the overlap volume in the presence of velocities or accelerations which limits the overall achievable interferometry time. Nevertheless, this may be an interesting approach for short interferometry times in a high-bandwidth measurement application.

To circumvent the issue of reflecting the interferometry light off the grating, we have developed a method in which the functionalities of laser cooling and atom interferometry are split into different wavelengths. The grating is covered with an optical coating which transmits the cooling light and reflects the interferometry light as depicted in figure 5.3. The grating surface is first planarized with a thin transparent optical layer such as Spin-on-glass and coated with a specialized distributed Bragg reflector. This optical coating is made such that it transmits the cooling light at perpendicular incidence so that it reaches the grating where it is deflected and again transmitted through the coating. In contrast, the interferometry light does not penetrate through the optical coating and is reflected instead. For Rubidium, this could be implemented using cooling light at $\lambda_{D2} \approx 780\,\text{nm}$ and interferometry light at $\lambda_{D1} \approx 795\,\text{nm}$ though other elements and wavelength combinations are possible with proper choice of the optical coating. This wavelength combination would be well suited as both wavelengths could be transmitted through the same optics which keeps the setup simple. This way, an atom interferometer can be realized which applies the light for both laser cooling and interferometry on a single axis. We have filed this method as a patent [90] to realize a compact quantum sensor.

5.4 Future applications on ground and in space

On ground, quantum sensors are currently investigated within the scope of the Collaborative Research Center 1464: TerraQ [94], where transportable quantum sensors are developed and used for geodetic measurements [63]. These may provide important insights in local mass transportation phenomena such as groundwater variations, saltwater intrusion or vulcanology. Implementing schemes such as an atom chip fountain gravimeter [95] with the coated grating (figure 5.3) would then allow to measure accelerations with a compact and transportable device which could be used to span networks of quantum sensors.

The inertial sensitivity of atom interferometry may also be exploited to serve as a reference in Quantum Navigation [96]. Classical inertial measurement units (IMU) contain accelerometers and gyroscopes which suffer from spurious long-term drifts that accumulate into a position error over time. Combining the short-term performance of IMUs with the long-term stability of atom interferometers may then be used to combine the best of both worlds into a novel hybrid quantum inertial sensor.

The Bose-Einstein Condensate and Cold Atom Laboratory (BECCAL) [97] is a NASA-DLR collaboration to bring a multi-user cold atom facility on board of the International Space Station (ISS) advancing the capabilities of the current Cold Atom Laboratory (CAL) [67, 98]. It will allow to conduct quantum-optical experiments using BECs of Rubidium and Potassium with higher repetition rates than previously possible to gather datasets with higher statistical relevance. It will add additional features such as painted optical potentials, rotation compensation and additional coils to address Feshbach resonances. This will allow to perform a wider range of quantum-optical experiments with extended experimental possibilities.

The European Commission has funded a pathfinder preparation mission for a cold atom interferometer in orbit for quantum accelerometry (CARIOQA-PMP) [99, 100] to increase the technical readiness level of the involved critical components. The goal of the activity is to pave the way for a future space mission for Earth observation based on quantum gravimetry with ultra-cold atoms. With the improved accuracy through atom interferometery it is expected to gain better understanding of mass transports on Earth as caused by, e.g. melting ice due to climate change or droughts due to extensive ground water withdrawal.

With the gained insights into atom interferometry on long timescales in space it will be possible to launch more demanding missions to test the Universality of Free Fall [11, 31, 101], detect Gravitational Waves [34–39] or search for ultra-light dark matter [36].

Although it is still planned to use the established mirror atom chip technology in the space missions of the near future, they may be replaced in the next generation of missions by the nano-structured chip once the single-beam BEC source has been demonstrated and the performance is verified. This will significantly reduce the deployment complexity and pave the way for quantum technologies on ground and in space.

Bibliography

1. GEORGI, HOWARD and SHELDON L GLASHOW: "Unity of all elementary-particle forces." *Physical Review Letters* (1974), vol. 32(8): p. 438 (cit. on p. c).

2. TOUBOUL, PIERRE, GILLES MÉTRIS, MANUEL RODRIGUES, YVES ANDRÉ, QUENTIN BAGHI, JOEL BERGÉ, DAMIEN BOULANGER, STEFANIE BREMER, RATANA CHHUN, BRUNO CHRISTOPHE, et al.: "Space test of the equivalence principle: first results of the MICROSCOPE mission." *Classical and Quantum Gravity* (2019), vol. 36(22): p. 225006 (cit. on p. c).

3. WILLIAMS, JAMES G, SLAVA G TURYSHEV, and DALE H BOGGS: "Lunar laser ranging tests of the equivalence principle." *Classical and Quantum Gravity* (2012), vol. 29(18): p. 184004 (cit. on p. c).

4. SCHLAMMINGER, STEPHAN, K-Y CHOI, TODD A WAGNER, JENS H GUNDLACH, and ERIC G ADELBERGER: "Test of the equivalence principle using a rotating torsion balance." *Physical Review Letters* (2008), vol. 100(4): p. 041101 (cit. on p. c).

5. ASENBAUM, PETER, CHRIS OVERSTREET, MINJEONG KIM, JOSEPH CURTI, and MARK A. KASEVICH: "Atom-Interferometric Test of the Equivalence Principle at the 10^{-12} Level." *Phys. Rev. Lett.* (19 Nov. 2020), vol. 125: p. 191101. DOI: 10.1103/PhysRevLett.125.191101 (cit. on p. c).

6. ALBERS, HENNING, ALEXANDER HERBST, LOGAN L RICHARDSON, HENDRIK HEINE, DIPANKAR NATH, JONAS HARTWIG, CHRISTIAN SCHUBERT, CHRISTIAN VOGT, MARIAN WOLTMANN, CLAUS LÄMMERZAHL, SVEN HERRMANN, WOLFGANG ERTMER, ERNST M. RASEL, and DENNIS SCHLIPPERT: "Quantum test of the Universality of Free Fall using rubidium and potassium." *The European Physical Journal D* (2020), vol. 74(7): pp. 1–9. DOI: 10.1140/epjd/e2020-10132-6 (cit. on p. c).

7. HARTWIG, JONAS, SVEN ABEND, CHRISTIAN SCHUBERT, DENNIS SCHLIPPERT, HOLGER AHLERS, KATERINE POSSO-TRUJILLO, NACEUR GAALOUL, WOLFGANG ERTMER, and ERNST MARIA RASEL: "Testing the universality of free fall with rubidium and ytterbium in a very large baseline atom interferometer." *New Journal of Physics* (2015), vol. 17(3): p. 035011 (cit. on p. c).

8. DAMOUR, THIBAULT: "Theoretical aspects of the equivalence principle." *Classical and Quantum Gravity* (2012), vol. 29(18): p. 184001 (cit. on p. c).

9. WILLIAMS, JASON, SHENG-WEY CHIOW, NAN YU, and HOLGER MÜLLER: "Quantum test of the equivalence principle and space-time aboard the International Space Station." *New Journal of Physics* (2016), vol. 18(2): p. 025018 (cit. on p. c).

10. WOLF, PETER, LUC BLANCHET, KAI BONGS, PHILIPPE BOUYER, BAPTISTE BATTE-
    LIER, ANDREA BERTOLDI, CLAUS BRAXMAIER, LISA WÖRNER, DAVIDE CALONICO,
    PIERRE FAYET, et al.: "Exploring the Foundations of the Physical Universe with
    Space Tests of the Equivalence Principle." (2019), vol. (cit. on p. c).

11. AGUILERA, DN, HOLGER AHLERS, BAPTISTE BATTELIER, AHMAD BAWAMIA,
    ANDREA BERTOLDI, R BONDARESCU, KAI BONGS, PHILIPPE BOUYER, CLAUS
    BRAXMAIER, LUIGI CACCIAPUOTI, et al.: "STE-QUESTtest of the universality of
    free fall using cold atom interferometry." *Classical and Quantum Gravity* (2014), vol.
    31(11): p. 115010 (cit. on pp. c, 1, 81).

12. HENSEL, T, S LORIANI, C SCHUBERT, F FITZEK, S ABEND, H AHLERS, J-N SIEMSS,
    K HAMMERER, EM RASEL, and N GAALOUL: "Inertial sensing with quantum gases:
    a comparative performance study of condensed versus thermal sources for atom
    interferometry." *The European Physical Journal D* (2021), vol. 75(3): pp. 1–13 (cit. on
    pp. c, 1).

13. LACHMANN, MAIKE D, HOLGER AHLERS, DENNIS BECKER, ALINE N DINKELAKER,
    JENS GROSSE, ORTWIN HELLMIG, HAUKE MÜNTINGA, VLADIMIR SCHKOLNIK,
    STEPHAN T SEIDEL, THIJS WENDRICH, et al.: "Ultracold atom interferometry in
    space." *Nature communications* (2021), vol. 12(1): pp. 1–6 (cit. on pp. c, 47, 79).

14. RUDOLPH, JAN, WALDEMAR HERR, CHRISTOPH GRZESCHIK, TAMMO STERNKE,
    ALEXANDER GROTE, MANUEL POPP, DENNIS BECKER, HAUKE MÜNTINGA, HOL-
    GER AHLERS, ACHIM PETERS, et al.: "A high-flux BEC source for mobile atom
    interferometers." *New Journal of Physics* (2015), vol. 17(6): p. 065001 (cit. on pp. c,
    3, 15, 29, 33, 47, 65, 67, 68).

15. BECKER, DENNIS, MAIKE D LACHMANN, STEPHAN T SEIDEL, HOLGER AHLERS,
    ALINE N DINKELAKER, JENS GROSSE, ORTWIN HELLMIG, HAUKE MÜNTINGA,
    VLADIMIR SCHKOLNIK, THIJS WENDRICH, et al.: "Space-borne Bose–Einstein con-
    densation for precision interferometry." *Nature* (2018), vol. 562(7727): pp. 391–395
    (cit. on pp. c, 3, 15, 16, 29, 33, 47).

16. POPP, MANUEL ANDRÉ: "Compact, low-noise current drivers for quantum sensors
    with atom chips." PhD thesis. Hannover: Institutionelles Repositorium der Leibniz
    Universität Hannover, 2018 (cit. on pp. c, 32, 47).

17. BARTOSCH, WOLFGANG: "The electronic and experimental setup of the MAIUS-2
    and MAIUS-3 sounding rocket missions." PhD thesis. Hannover: Institutionelles
    Repositorium der Leibniz Universität Hannover, 2021 (cit. on p. c).

18. IMHOF, ERIC, BENJAMIN K STUHL, BRIAN KASCH, BETHANY KROESE, SPENCER E
    OLSON, and MATTHEW B SQUIRES: "Two-dimensional grating magneto-optical
    trap." *Physical Review A* (2017), vol. 96(3): p. 033636 (cit. on pp. c, 4, 6, 79).

19. Nshii, CC, Matthieu Vangeleyn, Joseph P Cotter, Paul F Griffin, EA Hinds, Charles N Ironside, Patrick See, AG Sinclair, Erling Riis, and Aidan S Arnold: "A surface-patterned chip as a strong source of ultracold atoms for quantum technologies." *Nature nanotechnology* (2013), vol. 8(5): pp. 321–324 (cit. on pp. c, 4, 7, 14, 19, 59).

20. McGilligan, James P, Paul F Griffin, Rachel Elvin, Stuart J Ingleby, Erling Riis, and Aidan S Arnold: "Grating chips for quantum technologies." *Scientific reports* (2017), vol. 7(1): pp. 1–7 (cit. on pp. c, 4).

21. Bondza, Saskia, Christian Lisdat, Stefanie Kroker, and Tobias Leopold: "Two-color grating magneto-optical trap for narrow-line laser cooling." *arXiv preprint arXiv:2112.08833* (2021), vol. (cit. on pp. c, 4, 59).

22. Barker, DS, EB Norrgard, NN Klimov, JA Fedchak, J Scherschligt, and S Eckel: "Single-beam Zeeman slower and magneto-optical trap using a nanofabricated grating." *Physical Review Applied* (2019), vol. 11(6): p. 064023 (cit. on p. c).

23. Lewis, Ben, Rachel Elvin, Aidan S Arnold, Erling Riis, and Paul F Griffin: "A grating-chip atomic fountain." *Applied Physics Letters* (2022), vol. 121(16): p. 164001 (cit. on p. c).

24. Anderson, Mike H, Jason R Ensher, Michael R Matthews, Carl E Wieman, and Eric A Cornell: "Observation of Bose-Einstein condensation in a dilute atomic vapor." *science* (1995), vol. 269(5221): pp. 198–201 (cit. on p. 1).

25. Davis, Kendall B, M-O Mewes, Michael R Andrews, Nicolaas J van Druten, Dallin S Durfee, DM Kurn, and Wolfgang Ketterle: "Bose-Einstein condensation in a gas of sodium atoms." *Physical review letters* (1995), vol. 75(22): p. 3969 (cit. on p. 1).

26. Bloch, Immanuel, Jean Dalibard, and Wilhelm Zwerger: "Many-body physics with ultracold gases." *Reviews of modern physics* (2008), vol. 80(3): p. 885 (cit. on p. 1).

27. Lee, Patrick A, Naoto Nagaosa, and Xiao-Gang Wen: "Doping a Mott insulator: Physics of high-temperature superconductivity." *Reviews of modern physics* (2006), vol. 78(1): p. 17 (cit. on p. 1).

28. Le Hur, Karyn and T Maurice Rice: "Superconductivity close to the Mott state: From condensed-matter systems to superfluidity in optical lattices." *Annals of Physics* (2009), vol. 324(7): pp. 1452–1515 (cit. on p. 1).

29. Kovachy, Tim, Jason M Hogan, Alex Sugarbaker, Susannah M Dickerson, Christine A Donnelly, Chris Overstreet, and Mark A Kasevich: "Matter wave lensing to picokelvin temperatures." *Physical review letters* (2015), vol. 114(14): p. 143004 (cit. on p. 1).

30. Deppner, Christian, Waldemar Herr, Merle Cornelius, Peter Stromberger, Tammo Sternke, Christoph Grzeschik, Alexander Grote, Jan Rudolph, Sven Herrmann, Markus Krutzik, et al.: "Collective-mode enhanced matter-wave optics." *Physical Review Letters* (2021), vol. 127(10): p. 100401 (cit. on p. 1).

31. BATTELIER, BAPTISTE, JOËL BERGÉ, ANDREA BERTOLDI, LUC BLANCHET, KAI
     BONGS, PHILIPPE BOUYER, CLAUS BRAXMAIER, DAVIDE CALONICO, PIERRE FAYET,
     NACEUR GAALOUL, et al.: "Exploring the foundations of the physical universe with
     space tests of the equivalence principle." *Experimental Astronomy* (2021), vol. 51(3):
     pp. 1695–1736 (cit. on pp. 1, 81).

32. TRIMECHE, AZER, BAPTISTE BATTELIER, DENNIS BECKER, ANDREA BERTOLDI,
     PHILIPPE BOUYER, CLAUS BRAXMAIER, ERIC CHARRON, ROBIN CORGIER, MERLE
     CORNELIUS, KARIM DOUCH, et al.: "Concept study and preliminary design of a cold
     atom interferometer for space gravity gradiometry." *Classical and Quantum Gravity*
     (2019), vol. 36(21): p. 215004 (cit. on p. 1).

33. LÉVÈQUE, T, C FALLET, M MANDEA, R BIANCALE, JM LEMOINE, S TARDIVEL,
     S DELAVAULT, A PIQUEREAU, S BOURGOGNE, F PEREIRA DOS SANTOS, et al.:
     "Gravity field mapping using laser-coupled quantum accelerometers in space." *Journal
     of Geodesy* (2021), vol. 95(1): pp. 1–19 (cit. on p. 1).

34. DELVA, PACOME and ERNST RASEL: "Matter wave interferometry and gravitational
     waves." *Journal of Modern Optics* (2009), vol. 56(18-19): pp. 1999–2004 (cit. on
     pp. 1, 81).

35. HOGAN, JASON M, DAVID MS JOHNSON, SUSANNAH DICKERSON, TIM KOVACHY,
     ALEX SUGARBAKER, SHENG-WEY CHIOW, PETER W GRAHAM, MARK A KASEVICH,
     BABAK SAIF, SURJEET RAJENDRAN, et al.: "An atomic gravitational wave interfero-
     metric sensor in low earth orbit (AGIS-LEO)." *General Relativity and Gravitation*
     (2011), vol. 43(7): pp. 1953–2009 (cit. on pp. 1, 81).

36. ABOU EL-NEAJ, YOUSEF, CRISTIANO ALPIGIANI, SANA AMAIRI-PYKA, HENRIQUE
     ARAÚJO, ANTUN BALA, ANGELO BASSI, LARS BATHE-PETERS, BAPTISTE BATTE-
     LIER, ALEKSANDAR BELI, ELLIOT BENTINE, et al.: "AEDGE: atomic experiment
     for dark matter and gravity exploration in space." *EPJ Quantum Technology* (2020),
     vol. 7(1): pp. 1–27 (cit. on pp. 1, 81).

37. LORIANI, S, D SCHLIPPERT, C SCHUBERT, S ABEND, H AHLERS, WOLFGANG
     ERTMER, J RUDOLPH, JM HOGAN, MA KASEVICH, EM RASEL, et al.: "Atomic
     source selection in space-borne gravitational wave detection." *New Journal of Physics*
     (2019), vol. 21(6): p. 063030 (cit. on pp. 1, 81).

38. CANUEL, BENJAMIN, SVEN ABEND, PAU AMARO-SEOANE, FRANCESCA BADARACCO,
     QUENTIN BEAUFILS, ANDREA BERTOLDI, KAI BONGS, PHILIPPE BOUYER, CLAUS
     BRAXMAIER, WALID CHAIBI, et al.: "ELGARa European laboratory for gravitation
     and atom-interferometric research." *Classical and Quantum Gravity* (2020), vol.
     37(22): p. 225017 (cit. on pp. 1, 81).

39. BADURINA, L, E BENTINE, DIEGO BLAS, K BONGS, D BORTOLETTO, T BOWCOCK,
     K BRIDGES, W BOWDEN, O BUCHMUELLER, C BURRAGE, et al.: "AION: an atom
     interferometer observatory and network." *Journal of Cosmology and Astroparticle
     Physics* (2020), vol. 2020(05): p. 011 (cit. on pp. 1, 81).

40. CHAUDHURI, SAPTARISHI, SANJUKTA ROY, and C. S. UNNIKRISHNAN: "Realization of an intense cold Rb atomic beam based on a two-dimensional magneto-optical trap: Experiments and comparison with simulations." *Phys. Rev. A* (2 Aug. 2006), vol. 74: p. 023406. DOI: 10.1103/PhysRevA.74.023406 (cit. on pp. 2, 33, 34, 38).

41. CHAUDHURI, SAPTARISHI, SANJUKTA ROY, and CS UNNIKRISHNAN: "Evaporative cooling of atoms to quantum degeneracy in an optical dipole trap." *Journal of Physics: Conference Series*. Vol. 80. 1. IOP Publishing. 2007: p. 012036 (cit. on p. 2).

42. KETTERLE, WOLFGANG and NJ VAN DRUTEN: "Evaporative cooling of trapped atoms." *Advances in atomic, molecular, and optical physics* (1996), vol. 37: pp. 181–236 (cit. on pp. 2, 67, 68).

43. REICHEL, JAKOB: "Microchip traps and Bose–Einstein condensation." *Applied Physics B* (2002), vol. 74(6): pp. 469–487 (cit. on pp. 3, 10, 11).

44. PÉREZ-RIOS, J and AS SANZ: "How does a magnetic trap work?" *American Journal of Physics* (2013), vol. 81(11): pp. 836–843 (cit. on pp. 3, 60).

45. POLLOCK, SAMUEL, JP COTTER, ATHANASIOS LALIOTIS, and EA HINDS: "Integrated magneto-optical traps on a chip using silicon pyramid structures." *Optics Express* (2009), vol. 17(16): pp. 14109–14114 (cit. on pp. 4, 5).

46. RAVENHALL, SEAN, BENJAMIN YUEN, and CHRIS FOOT: "A high-flux, adjustable, compact cold-atom source." *arXiv preprint arXiv:2102.00251* (2021), vol. (cit. on p. 4).

47. POLLOCK, SAMUEL, JP COTTER, ATHANASIOS LALIOTIS, FERNANDO RAMIREZ-MARTINEZ, and EA HINDS: "Characteristics of integrated magneto-optical traps for atom chips." *New Journal of Physics* (2011), vol. 13(4): p. 043029 (cit. on pp. 4, 5).

48. VANGELEYN, MATTHIEU, PAUL F GRIFFIN, ERLING RIIS, and AIDAN S ARNOLD: "Single-laser, one beam, tetrahedral magneto-optical trap." *Optics express* (2009), vol. 17(16): pp. 13601–13608 (cit. on pp. 4, 5).

49. BODART, QUENTIN, SÉBASTIEN MERLET, NICOLA MALOSSI, F PEREIRA DOS SANTOS, PHILIPPE BOUYER, and ARNAUD LANDRAGIN: "A cold atom pyramidal gravimeter with a single laser beam." *Applied Physics Letters* (2010), vol. 96(13): p. 134101 (cit. on p. 4).

50. MCGILLIGAN, JAMES P, PAUL F GRIFFIN, ERLING RIIS, and AIDAN S ARNOLD: "Phase-space properties of magneto-optical traps utilising micro-fabricated gratings." *Optics express* (2015), vol. 23(7): pp. 8948–8959 (cit. on pp. 4, 14, 15, 59).

51. MCGILLIGAN, JAMES P, PAUL F GRIFFIN, ERLING RIIS, and AIDAN S ARNOLD: "Diffraction-grating characterization for cold-atom experiments." *JOSA B* (2016), vol. 33(6): pp. 1271–1277 (cit. on pp. 4, 7).

52. LEE, J, JA GROVER, LA OROZCO, and SL ROLSTON: "Sub-Doppler cooling of neutral atoms in a grating magneto-optical trap." *JOSA B* (2013), vol. 30(11): pp. 2869–2874 (cit. on pp. 4, 14, 56).

53. SITARAM, ANANYA, PK ELGEE, GRETCHEN K CAMPBELL, NN KLIMOV, S ECKEL, and DS BARKER: "Confinement of an alkaline-earth element in a grating magneto-optical trap." *Review of Scientific Instruments* (2020), vol. 91(10): p. 103202 (cit. on p. 4).

54. KIM, JA, KI LEE, HR NOH, W JHE, and M OHTSU: "Atom trap in an axicon mirror." *Optics letters* (1997), vol. 22(2): pp. 117–119 (cit. on p. 5).

55. LEE, KI, JA KIM, HR NOH, and W JHE: "Single-beam atom trap in a pyramidal and conical hollow mirror." *Optics letters* (1996), vol. 21(15): pp. 1177–1179 (cit. on p. 5).

56. BURROW, OLIVER S, ROBERT J FASANO, WESLEY BRAND, MICHAEL W WRIGHT, WENBO LI, ANDREW D LUDLOW, ERLING RIIS, PAUL F GRIFFIN, and AIDAN S ARNOLD: "Optimal binary gratings for multi-wavelength magneto-optical traps." *arXiv preprint arXiv:2306.17080* (2023), vol. (cit. on p. 6).

57. COTTER, JP, JP MCGILLIGAN, PF GRIFFIN, IM RABEY, K DOCHERTY, E RIIS, AS ARNOLD, and EA HINDS: "Design and fabrication of diffractive atom chips for laser cooling and trapping." *Applied Physics B* (2016), vol. 122(6): p. 172 (cit. on pp. 7, 19).

58. REICHEL, JAKOB and VLADAN VULETIC: *Atom chips.* John Wiley & Sons, 2011 (cit. on p. 11).

59. CHUANG, HO-CHIAO, CHUNG-WEN WENG, and HSIANG-FU LI: "Design, microfabrication and characterization of planarized multilayer atom chips with enhanced heat dissipation." *Journal of Micromechanics and Microengineering* (2011), vol. 21(12): p. 125009 (cit. on p. 11).

60. HÄNSEL, WOLFGANG: "Magnetische Mikrofallen für Rubidiumatome." PhD thesis. Ludwig-Maximilians-Universität München., 2000 (cit. on p. 13).

61. FOOT, CHRISTOPHER J et al.: *Atomic physics.* Vol. 7. Oxford University Press, 2005 (cit. on pp. 12, 21).

62. SAHELGOZIN, MARAL: "Design and construction of a transportable quantum gravimeter and realization of an atom-chip magnetic trap." PhD thesis. Hannover: Institutionelles Repositorium der Leibniz Universität Hannover, 2019 (cit. on pp. 15, 35, 60).

63. HEINE, NINA, JONAS MATTHIAS, MARAL SAHELGOZIN, WALDEMAR HERR, SVEN ABEND, LUDGER TIMMEN, JÜRGEN MÜLLER, and ERNST MARIA RASEL: "A transportable quantum gravimeter employing delta-kick collimated Bose–Einstein condensates." *The European Physical Journal D* (2020), vol. 74(8): pp. 1–8 (cit. on pp. 15, 16, 33, 81).

64. *EPO-TEK H77 Thermally Conductive Epoxy Datasheet.* URL: https://www.epotek.com/docs/en/Datasheet/H77.pdf (visited on 06/21/2023) (cit. on pp. 17, 18).

65. *EPO-TEK H21D Electrically Conductive Silver Epoxy Datasheet.* URL: https://www.epotek.com/docs/en/Datasheet/H21D.pdf (visited on 06/21/2023) (cit. on p. 18).

66. LINDQUIST, K, M STEPHENS, and C WIEMAN: "Experimental and theoretical study of the vapor-cell Zeeman optical trap." *Physical Review A* (1992), vol. 46(7): p. 4082 (cit. on p. 22).

67. AVELINE, DAVID C, JASON R WILLIAMS, ETHAN R ELLIOTT, CHELSEA DUTENHOF-FER, JAMES R KELLOGG, JAMES M KOHEL, NORMAN E LAY, KAMAL OUDRHIRI, ROBERT F SHOTWELL, NAN YU, et al.: "Observation of Bose–Einstein condensates in an Earth-orbiting research lab." *Nature* (2020), vol. 582(7811): pp. 193–197 (cit. on pp. 29, 81).

68. FEDCHAK, JAMES A, JULIA K SCHERSCHLIGT, SEFER AVDIAJ, DANIEL S BARKER, STEPHEN P ECKEL, BEN BOWERS, SCOTT OCONNELL, and PERRY HENDERSON: "Outgassing rate comparison of seven geometrically similar vacuum chambers of different materials and heat treatments." *Journal of Vacuum Science & Technology B, Nanotechnology and Microelectronics: Materials, Processing, Measurement, and Phenomena* (2021), vol. 39(2): p. 024201 (cit. on p. 30).

69. MATSUSHITA, TERUO: *Electricity and magnetism: new formulation by introduction of superconductivity.* Springer Science & Business Media, 2013 (cit. on p. 32).

70. BECKER, DENNIS: "Demonstration einer neuartigen kompakten chip-basierten Quelle kalter Atome." MA thesis. Hannover: Gottfried Wilhelm Leibniz Universität Hannover, 2011 (cit. on p. 35).

71. GONIDEC, MELANIE SUSANNE LE: "Setup and characterization of a laser system for the manipulation of 87Rb atoms for an atom chip teststand." MA thesis. Leibniz Universität Hannover, 2018 (cit. on p. 38).

72. OBERRÖHRMANN, JONAS: "Aufteilung und Leistungsstabilisierung von Laserlicht für den Betrieb einer magneto-optischen Falle." Bachelor's thesis. 2020 (cit. on pp. 38, 39).

73. MCCARRON, DJ, SA KING, and SL CORNISH: "Modulation transfer spectroscopy in atomic rubidium." *Measurement science and technology* (2008), vol. 19(10): p. 105601 (cit. on p. 38).

74. REINAUDI, G, T LAHAYE, Z WANG, and D GUÉRY-ODELIN: "Strong saturation absorption imaging of dense clouds of ultracold atoms." *Optics letters* (2007), vol. 32(21): pp. 3143–3145 (cit. on p. 45).

75. MÜNTINGA, HAUKE: "Matter-wave Interferometry for space-borne Inertial Sensors." PhD thesis. Universität Bremen, 2019 (cit. on p. 45).

76. WENDRICH, THIJS. Stackable control electronics developed by the electronics team under the lead of Dr. Thijs Wendrich in the group of Ernst M. Rasel at Leibniz Universität Hannover, Institut für Quantenoptik. (cit. on p. 47).

77. Preibisch, Stephan, Stephan Saalfeld, and Pavel Tomancak: "Globally optimal stitching of tiled 3D microscopic image acquisitions." *Bioinformatics* (2009), vol. 25(11): pp. 1463–1465 (cit. on pp. 50, 52).

78. Meschede, Dieter: *Optik, Licht und Laser.* Springer-Verlag, 2009 (cit. on pp. 53, 98).

79. Bean, CP, RW DeBlois, and LB Nesbitt: "Eddy-current method for measuring the resistivity of metals." *Journal of Applied Physics* (1959), vol. 30(12): pp. 1976–1980 (cit. on p. 57).

80. Matthias, Jonas: "Magnetic trapping for an atom-chip-based gravimeter." PhD thesis. Hannover: Institutionelles Repositorium der Leibniz Universität Hannover, 2020 (cit. on p. 60).

81. Petrich, Wolfgang, Michael H Anderson, Jason R Ensher, and Eric A Cornell: "Stable, tightly confining magnetic trap for evaporative cooling of neutral atoms." *Physical Review Letters* (1995), vol. 74(17): p. 3352 (cit. on p. 63).

82. Davis, Kendall B, M-O Mewes, and Wolfgang Ketterle: "An analytical model for evaporative cooling of atoms." *Applied Physics B* (1995), vol. 60(2): pp. 155–159 (cit. on p. 67).

83. Snoke, DW and JP Wolfe: "Population dynamics of a Bose gas near saturation." *Physical Review B* (1989), vol. 39(7): p. 4030 (cit. on p. 67).

84. Snoke, DW, WW Rühle, Y-C Lu, and E Bauser: "Evolution of a nonthermal electron energy distribution in GaAs." *Physical Review B* (1992), vol. 45(19): p. 10979 (cit. on p. 67).

85. Söding, J, D Guéry-Odelin, P Desbiolles, F Chevy, H Inamori, and J Dalibard: "Three-body decay of a rubidium Bose–Einstein condensate." *Applied physics B* (1999), vol. 69(4): pp. 257–261 (cit. on p. 67).

86. Migdall, Alan L, John V Prodan, William D Phillips, Thomas H Bergeman, and Harold J Metcalf: "First observation of magnetically trapped neutral atoms." *Physical Review Letters* (1985), vol. 54(24): p. 2596 (cit. on p. 67).

87. Luiten, OJ, MW Reynolds, and JTM Walraven: "Kinetic theory of the evaporative cooling of a trapped gas." *Physical Review A* (1996), vol. 53(1): p. 381 (cit. on p. 68).

88. *Messung des Erdmagnetfeldes in der PTB.* url: https://www.ptb.de/cms/nc/ptb/fachabteilungen/abt2/fb-25/ag-251/live-daten-erdmagnetfeldmessung.html (visited on 07/10/2020) (cit. on p. 73).

89. Lee, Chin C, Chen Y Wang, Goran Matijasevic, and Steve S Chan: "A new gold-indium eutectic bonding method." *MRS Online Proceedings Library* (1992), vol. 264(1): pp. 305–310 (cit. on p. 78).

90. RASEL, ERNST M., HENDRIK HEINE, WALDEMAR HERR, CHRISTIAN SCHUBERT, ALEXANDER KASSNER, and MARC C. WURZ: "Quantensensor und Verfahren zu dessen Herstellung." DE 10 2023 118 819.4. Deutsches Patent- und Markenamt, Patentanmeldung. 2023 (cit. on p. 80).

91. LACHMANN, MAIKE DIANA: "Materiewelleninterferenzen im Weltraum." (2020), vol. (cit. on p. 79).

92. CORGIER, ROBIN: "Engineered atomic states for precision interferometry." (2019), vol. (cit. on p. 79).

93. CHEINEY, PIERRICK, BAPTISTE GOURAUD, DAVID BRYNLE BARRET, BAPTISTE BATTELIER, and PHILIPPE BOUYER: "ATOMIC INTERFEROMETER WITH TWO-DIMENSIONAL DIFFRACTION NETWORK AND ATOMIC INTERFEROMETRY METHOD." EP 3 893 003 B1. 2022 (cit. on p. 80).

94. *SFB1464: TerraQ - Relativistische und quanten-basierte Geodäsie*. URL: https://www.terraq.uni-hannover.de/ (visited on 06/16/2023) (cit. on p. 81).

95. ABEND, SVEN, MARTINA GEBBE, MATTHIAS GERSEMANN, HOLGER AHLERS, HAUKE MÜNTINGA, ENNO GIESE, NACEUR GAALOUL, CHRISTIAN SCHUBERT, CLAUS LÄMMERZAHL, WOLFGANG ERTMER, et al.: "Atom-chip fountain gravimeter." *Physical review letters* (2016), vol. 117(20): p. 203003 (cit. on p. 81).

96. CHEINEY, PIERRICK, LAURIANE FOUCHÉ, SIMON TEMPLIER, FABIEN NAPOLITANO, BAPTISTE BATTELIER, PHILIPPE BOUYER, and BRYNLE BARRETT: "Navigation-compatible hybrid quantum accelerometer using a Kalman filter." *Physical Review Applied* (2018), vol. 10(3): p. 034030 (cit. on p. 81).

97. FRYE, KAI, SVEN ABEND, WOLFGANG BARTOSCH, AHMAD BAWAMIA, DENNIS BECKER, HOLGER BLUME, CLAUS BRAXMAIER, SHENG-WEY CHIOW, MAXIM A EFREMOV, WOLFGANG ERTMER, et al.: "The Bose-Einstein condensate and cold atom laboratory." *EPJ Quantum Technology* (2021), vol. 8(1): pp. 1–38 (cit. on p. 81).

98. CAROLLO, RYAN A, DAVID C AVELINE, BRENDAN RHYNO, SMITHA VISHVESH-WARA, COURTNEY LANNERT, JOSEPH D MURPHREE, ETHAN R ELLIOTT, JASON R WILLIAMS, ROBERT J THOMPSON, and NATHAN LUNDBLAD: "Observation of ultracold atomic bubbles in orbital microgravity." *Nature* (2022), vol. 606(7913): pp. 281–286 (cit. on p. 81).

99. LÉVÈQUE, T, C FALLET, J LEFEBVE, A PIQUEREAU, A GAUGUET, B BATTELIER, P BOUYER, N GAALOUL, M LACHMANN, B PIEST, et al.: "CARIOQA: Definition of a Quantum Pathfinder Mission." *arXiv preprint arXiv:2211.01215* (2022), vol. (cit. on p. 81).

100. *Cold Atom Rubidium Interferometer in Orbit for Quantum Accelerometry Pathfinder Mission Preparation*. URL: https://doi.org/10.3030/101081775 (visited on 06/09/2023) (cit. on p. 81).

101. LORIANI, SINA, CHRISTIAN SCHUBERT, DENNIS SCHLIPPERT, WOLFGANG ERTMER, FRANCK PEREIRA DOS SANTOS, ERNST MARIA RASEL, NACEUR GAALOUL, and PETER WOLF: "Resolution of the colocation problem in satellite quantum tests of the universality of free fall." *Physical Review D* (2020), vol. 102(12): p. 124043 (cit. on p. 81).

102. *Imaging Performance Specification Grasshopper3 USB3.* Version 17.2, Rev. 1/27/2017. FLIR. 2017 (cit. on p. 99).

103. *Technical Reference Grasshopper3 USB3.* Version 18, Rev. 1/26/2017. FLIR. 2017 (cit. on p. 99).

104. INC., WOLFRAM RESEARCH: *Mathematica, Version 13.1.* Champaign, IL, 2022 (cit. on p. 100).

105. HERR, WALDEMAR: "Eine kompakte Quelle quantenentarteter Gase hohen Flusses für die Atominterferometrie unter Schwerelosigkeit." PhD thesis. Hannover: Gottfried Wilhelm Leibniz Universität Hannover, 2013 (cit. on p. 100).

List of Figures

List of Tables

A Appendix

A.1 Polarization projection on quantization axis

Consider a light field with wave vector $\vec{k}$ propagating along the z-direction. Then the electric field of the light oscillates in the xy-plane as

$$\vec{E}(t) = \begin{pmatrix} E_x(t) \\ E_y(t) \\ 0 \end{pmatrix} = \frac{\tilde{E}}{\sqrt{2}}\, e^{i(\vec{k}\vec{r}-\omega t)} \begin{pmatrix} e^{i\psi_x} \\ e^{i\psi_y} \\ 0 \end{pmatrix} = \frac{\tilde{E}(t)}{\sqrt{2}} \begin{pmatrix} 1 \\ e^{i\xi} \\ 0 \end{pmatrix} \tag{A.1}$$

with a relative retardance phase $\xi = \psi_y - \psi_x$ between the x- and y component that determines the polarization of the light. An atom that is aligned along a magnetic field $\vec{B}$ which encloses an angle

$$\cos\phi = \frac{\vec{k}\cdot\vec{B}}{|\vec{k}||\vec{B}|} \tag{A.2}$$

with the light will perceive the light field in its frame as the projection of the field components on its own quantization axis so that the polarization vector appears as

$$\vec{E} = \frac{E_0}{\sqrt{2}} \begin{pmatrix} 1 \\ e^{i\xi}\cos\phi \\ e^{i\xi}\sin\phi \end{pmatrix}. \tag{A.3}$$

To find the possible transitions that the light may drive, one has to describe this field in the basis of the polarization unity vectors

$$\hat{e}_- = \frac{1}{\sqrt{2}} \begin{pmatrix} 1 \\ -i \\ 0 \end{pmatrix}, \quad \hat{e}_\pi = \begin{pmatrix} 0 \\ 0 \\ 1 \end{pmatrix}, \quad \hat{e}_+ = \frac{1}{\sqrt{2}} \begin{pmatrix} 1 \\ i \\ 0 \end{pmatrix} \tag{A.4}$$

with amplitudes E_-, E_π, E_+ before calculating the corresponding intensities. This requires to solve the equation system

$$\frac{E_0}{\sqrt{2}} \begin{pmatrix} 1 \\ e^{i\xi}\cos\phi \\ e^{i\xi}\sin\phi \end{pmatrix} = \frac{E_-}{\sqrt{2}} \begin{pmatrix} 1 \\ -i \\ 0 \end{pmatrix} + E_\pi \begin{pmatrix} 0 \\ 0 \\ 1 \end{pmatrix} + \frac{E_+}{\sqrt{2}} \begin{pmatrix} 1 \\ i \\ 0 \end{pmatrix} \tag{A.5}$$

which is solved by

$$E_- = \frac{E_0}{2}\left(1 + i\,e^{i\xi}\cos\phi\right), \tag{A.6}$$

$$E_\pi = \frac{E_0\,e^{i\xi}}{\sqrt{2}}\sin\phi, \tag{A.7}$$

$$E_+ = \frac{E_0}{2}\left(1 - i\,e^{i\xi}\cos\phi\right). \tag{A.8}$$

The relative strengths are found by calculating the corresponding intensities [78]

$$I = \frac{1}{2}\,c\,\varepsilon_0\,\mathrm{Re}\left[E^* \cdot E\right] \tag{A.9}$$

which yields

$$I_- = I_0\frac{1}{4}\mathrm{Re}\left[\left(1 + i\,e^{i\xi}\cos\phi\right)\left(1 - i\,e^{-i\xi}\cos\phi\right)\right] = I_0\frac{1 + \cos^2\phi - 2\sin\xi\cos\phi}{4} \tag{A.10}$$

$$I_\pi = I_0\frac{1}{2}\sin^2\phi \tag{A.11}$$

$$I_+ = I_0\frac{1}{4}\mathrm{Re}\left[\left(1 - i\,e^{i\xi}\cos\phi\right)\left(1 + i\,e^{-i\xi}\cos\phi\right)\right] = I_0\frac{1 + \cos^2\phi + 2\sin\xi\cos\phi}{4} \tag{A.12}$$

with the corresponding relative strengths $\alpha = I/I_0$

$$\alpha_{-1} = \frac{1 + \cos^2\phi - 2\sin\xi\cos\phi}{4} \tag{A.13}$$

$$\alpha_0 = \frac{1}{2}\sin^2\phi \tag{A.14}$$

$$\alpha_{+1} = \frac{1 + \cos^2\phi + 2\sin\xi\cos\phi}{4}. \tag{A.15}$$

A.2 Properties of the CCD camera for absorption imaging

Table A.1: Relevant technical specifications of the CCD camera [`Pointgrey Grasshopper USB3 GS3-U3-15S5M`] used for absorption imaging [102, 103].

Property	Value
Resolution	1384 x 1032
Megapixel	1.4 MP
Chroma	Mono
ADC	14 bits
Pixel size	$6.45\,\mu m$
Quantum efficiency at $780\,nm$	0.365
Saturation Capacity	$22856\ e^-$
Gain	$0.37\ e^-/\mathrm{ADU}$

A.3 Magnetic field simulations

The magnetic field simulations of this work are based on a computer program written in Wolfram Mathematica [104] developed in [105] where also a more detailed description can be found. Briefly, the idea is to approximate all current-carrying structures by strings of current for which the field is calculated using the law of Biot-Savart. The total magnetic field at any position is then found by adding up the magnetic field contributions of all strings using the superposition principle.

A.3.1 Structure Modeling

Each structure is approximated by infinitesimal thin strings of current from which the magnetic field is calculated through the law of Biot-Savart. While wires feature round cross-sections which can be well approximated by single strings, the chip structures are manufactured with rectangular cross-sections. Since the atoms are close to the chip, a single wire string in the center would not approximate the situation very well. Therefore, the chip structures are approximated by defining the left and right boundaries and interpolating additional polygon strings in between where each of the n strings would carry $1/n$ of the current. Here, $n = 4$ was used for which as error around $1\,\%$ can be estimated [105].

The modeled wire structures for this work are shown in figure A.1. Three circular pairs of coils around the vacuum chamber with radii of $(98, 84, 54)\,\mathrm{mm}$ in (x,y,z) direction are modeled through a polygon with 40 strings of current. The winding number $N_\mathrm{w} = (34, 85, 34)$ for the respective coil is taken into account by increasing the effective current $I_\mathrm{eff}(t) = N_w * I(t)$ through the coil respectively. All wires of the chip are incorporated in the model but only the outer Z-structure of the Basechip, the mesoscopic H-wires and the mesoscopic O-wire were used for the simulations of this work (figure A.1c).

A.3.2 Simulation of the quadrupole magnetic field

With the wire models of above, the total magnetic field can be calculated at any point in the full volume around the chip. The quadrupole field for the gMOT is characterized by its minimum position, quadrupole axes and gradient strengths. First of all, the local minimum $\vec{r}_0$ needs to be determined. This is realized in Mathematica by using the internal routine

```
1  FindMinimum[].
```

A good guess of the field minimum eases the algorithm's capability to find the correct position. One can then determine the local gradient by calculating the local Jacobian matrix

$$
\begin{pmatrix}
\frac{\partial B_x}{\partial x} & \frac{\partial B_x}{\partial y} & \frac{\partial B_x}{\partial z} \\
\frac{\partial B_y}{\partial x} & \frac{\partial B_y}{\partial y} & \frac{\partial B_y}{\partial z} \\
\frac{\partial B_z}{\partial x} & \frac{\partial B_z}{\partial y} & \frac{\partial B_z}{\partial z}
\end{pmatrix}
\tag{A.16}
$$

and find the eigenvectors $\vec{v}_i$ of the matrix which point in the direction of the main quadrupole axes. This was implemented in Mathematica using the internal routine

```
1  Eigensystem[]
```
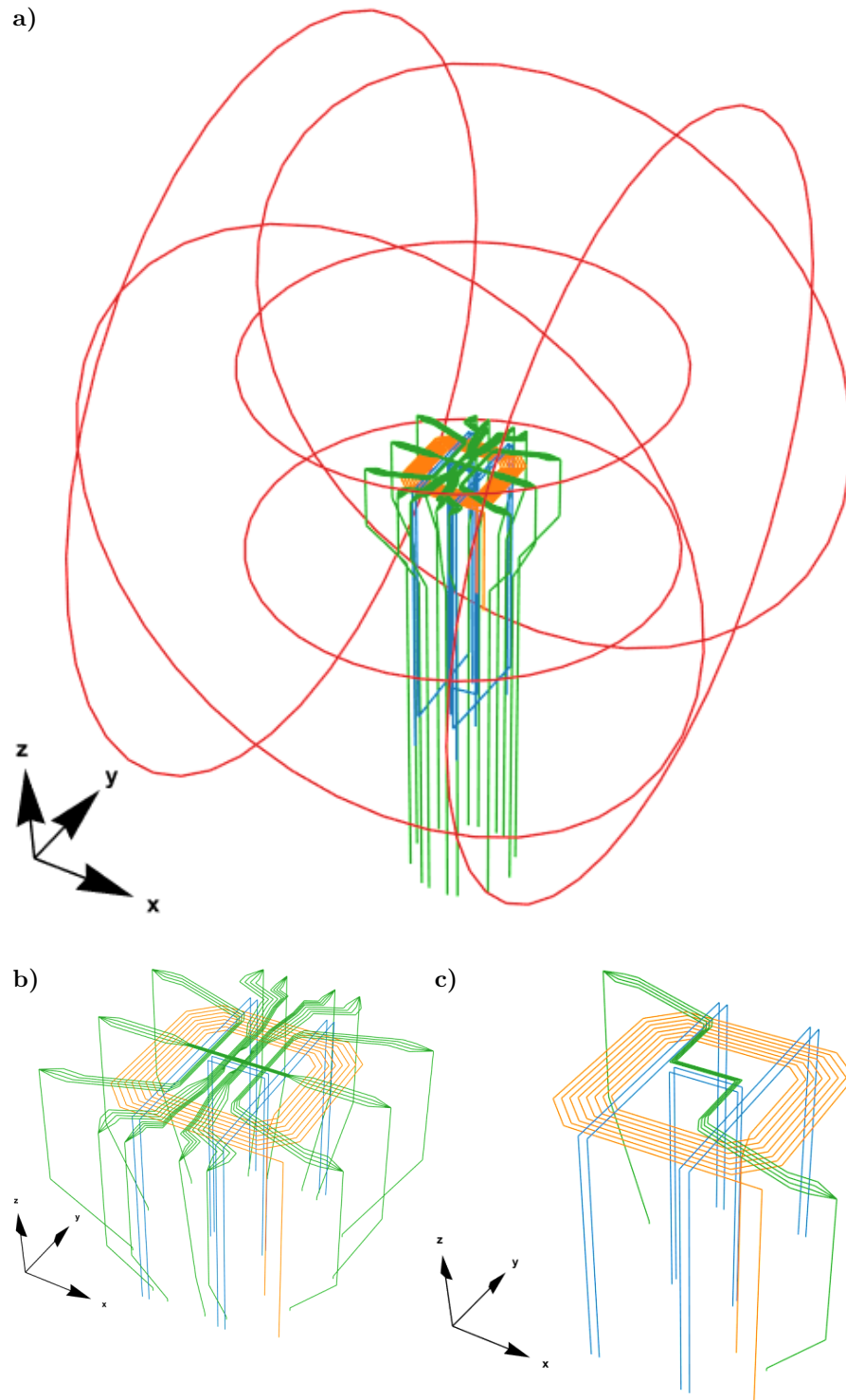
Figure A.1: Wire model for the magnetic field simulation with coils (red), mesoscopic O-wire (orange), mesoscopic H-wires (blue) and chip structures (green). **a)** Overview of the full model. **b)** Zoom-in into the chip. While the mesoscopic wires (H & O) are modeled by simple strings, the chip wires are approximated by four parallel wires to take the finite width into account. Each of the four chip strings carries only a quarter of the current. **c)** Chip structures relevant for the magnetic field simulations of this work. Only the outside Z-structure of the Basechip was used.

which calculates both the eigenvalues and eigenvectors. The field gradients along the eigenvectors are then calculated using

$$\left\| \frac{\vec{B}(\vec{r}_0) - \vec{B}(\vec{r}_0 + \varepsilon \vec{v}_i)}{\varepsilon} \right\| \tag{A.17}$$

for small values $\varepsilon \approx 1 \times 10^{-10}$ where $\| \, . \, \|$ is the norm of the vector.

A.3.3 Simulation of magnetic traps

For the magnetic traps, the gravitational potential has to be taken into account as well. The potential

$$V(\vec{r}) = \mu_{\mathrm{B}} g_F m_F \sqrt{\vec{B}(\vec{r}) \cdot \vec{B}(\vec{r})} - m\vec{g} \cdot \vec{r} \tag{A.18}$$

contains the contributions of the magnetic field through the Zeeeman effect and the gravitational potential through the local gravitational acceleration vector $\vec{g}$. Properties such as eigenaxes or trap frequencies are determined in the potential minimum where the harmonic approximation holds. It is again found using the internal routine

```
1  FindMinimum[]
```

in Mathematica. The trap frequencies can be calculated by deriving the eigensystem of the Hessian matrix

$$\begin{pmatrix} \frac{\partial^2 V}{\partial x \partial x} & \frac{\partial^2 V}{\partial x \partial y} & \frac{\partial^2 V}{\partial x \partial z} \\ \frac{\partial^2 V}{\partial y \partial x} & \frac{\partial^2 V}{\partial y \partial y} & \frac{\partial^2 V}{\partial y \partial z} \\ \frac{\partial^2 V}{\partial z \partial x} & \frac{\partial^2 V}{\partial z \partial y} & \frac{\partial^2 V}{\partial z \partial z} \end{pmatrix} \tag{A.19}$$

at the position of the minimum which contains the second order derivatives of the potential. In the coordinate system of the eigenvectors, the matrix becomes diagonal and the eigenvectors $\vec{v}_i$ point along the eigenaxes of the potential. The eigenvalues λ_i then simply correspond to the second order derivative of the potential along the direction $\vec{v}_i$ so that the trap frequency is calculated by

$$\omega_i = \sqrt{\frac{\lambda_i}{m}} \tag{A.20}$$

in accordance to the harmonic oscillator potential $V = \frac{1}{2}m\omega^2 x^2$ with $\omega = \sqrt{\frac{1}{m}\frac{\mathrm{d}^2 V}{\mathrm{d}x^2}}$. The magnetic traps are then evaluated around their minimum in the direction of their eigenaxes

$$V(\vec{r}_0 + \alpha * \vec{v}_i) \tag{A.21}$$

with a scaling factor α to find a local maximum in the respective directions i which will limit the trap. The trap depth is then the difference between the limiting trap potential V_i among all eigenaxes i and the trap bottom. It is typically limited along the axis of gravity

and stated in thermal units, i.e. by dividing the potential by the Boltzmann constant k_B. The trap bottom is calculated by simpliy evaluating the potential in the minimum $V(\vec{r}_0)$.

Publications

Scientific publications

1. CHRIST, MARC, ALEXANDER KASSNER, ROBERT SMOL, AHMAD BAWAMIA, **Hendrik Heine**, WALDEMAR HERR, ACHIM PETERS, MARC CHRISTOPHER WURZ, ERNST MARIA RASEL, ANDREAS WICHT, et al.: "Integrated atomic quantum technologies in demanding environments: development and qualification of miniaturized optical setups and integration technologies for UHV and space operation." *CEAS Space Journal* (2019), vol. 11(4): pp. 561–566. DOI: 10.1007/s12567-019-00252-0.

2. ALBERS, HENNING, ALEXANDER HERBST, LOGAN L RICHARDSON, **Hendrik Heine**, DIPANKAR NATH, JONAS HARTWIG, CHRISTIAN SCHUBERT, CHRISTIAN VOGT, MARIAN WOLTMANN, CLAUS LÄMMERZAHL, SVEN HERRMANN, WOLFGANG ERTMER, ERNST M. RASEL, and DENNIS SCHLIPPERT: "Quantum test of the Universality of Free Fall using rubidium and potassium." *The European Physical Journal D* (2020), vol. 74(7): pp. 1–9. DOI: 10.1140/epjd/e2020-10132-6.

3. ABEND, SVEN, BAPTISTE ALLARD, AIDAN S. ARNOLD, TICIJANA BAN, LIAM BARRY, BAPTISTE BATTELIER, AHMAD BAWAMIA, QUENTIN BEAUFILS, SIMON BERNON, ANDREA BERTOLDI, ALEXIS BONNIN, PHILIPPE BOUYER, ALEXANDRE BRESSON, OLIVER S. BURROW, BENJAMIN CANUEL, BRUNO DESRUELLE, GIANNIS DROUGAKIS, RENÉ FORSBERG, NACEUR GAALOUL, ALEXANDRE GAUGUET, MATTHIAS GERSEMANN, PAUL F. GRIFFIN, **Hendrik Heine**, et al.: "Technology roadmap for cold-atoms based quantum inertial sensor in space." *AVS Quantum Science* (2023), vol. 5(1): p. 019201. DOI: 10.1116/5.0098119.

Patents

1. KASSNER, ALEXANDER, MARC C. WURZ, ERNST M. RASEL, WALDEMAR HERR, and **Hendrik Heine**: "Mikrotechnologisch hergestellte Leiterbahnanordnung und Herstellungsverfahren." EP 4 247 131 A1. Europäische Patentanmeldung. 2022.

2. RASEL, ERNST M., **Hendrik Heine**, WALDEMAR HERR, CHRISTIAN SCHUBERT, ALEXANDER KASSNER, and MARC C. WURZ: "Quantensensor und Verfahren zu dessen Herstellung." DE 10 2023 118 819.4. Deutsches Patent- und Markenamt, Patentanmeldung. 2023.

Submissions to international conferences

1. **Heine, Hendrik**, Alexandros Papakonstantinou, Melanie Le Gonidec, Alexander Kassner, Mathias Rechel, Marc C. Wurz, Waldemar Herr, Wolfgang Ertmer, and Ernst M. Rasel: "Next generation atom chips for compact and transportable quantum sensors." Poster presented at: Young Atom Opticians conference, Paris, France. July 2017.

2. **Heine, Hendrik**, Joseph Muchovo, Aaditya Mishra, Christian Schubert, Waldemar Herr, and Ernst M. Rasel: "Single-beam laser cooling and magnetic trapping using a nano-structured atom chip." Presentation at the 53rd Annual Meeting of the APS Division of Atomic, Molecular and Optical Physics, Orlando, USA. June 2022.

Submissions to national conferences

1. **Heine, Hendrik**, Henning Albers, Jonas Hartwig, Dipankar Nath, Logan Richardson, Dennis Schlippert, Wolfgang Ertmer, and Ernst M. Rasel: "Dual Species matter-wave Interferometry." Poster presented at: Annual Conference of the DPG and DPG Spring Meeting, Heidelberg, Germany. Mar. 2015.

2. Richardson, Logan, Henning Albers, **Hendrik Heine**, Jonas Hartwig, Dipankar Nath, Dennis Schlippert, Wolfgang Ertmer, and Ernst M. Rasel: "Quantum Test of the Universality of Free Fall with a Dual Species Atom Interferometer." Presentation at the Annual Conference of the DPG and DPG Spring Meeting, Heidelberg, Germany. Mar. 2015.

3. **Heine, Hendrik**, Jonas Matthias, Nina Grove, Maral Sahelgozin, Alexander Kassner, Mathias Rechel, Sven Abend, Stephan T. Seidel, Waldemar Herr, Marc C. Wurz, Wolfgang Ertmer, and Ernst M. Rasel: "Atom-Chip based BEC sources for compact and transportable experiments." Poster presented at: Annual Conference of the DPG and DPG Spring Meeting, Mainz, Germany. Mar. 2017.

4. Papakonstantinou, Alexandros, **Hendrik Heine**, Melanie Le Gonidec, Alexander Kassner, Mathias Rechel, Waldemar Herr, Marc C. Wurz, Wolfgang Ertmer, and Ernst M. Rasel: "Planar diffraction optics on an atom chip." Poster presented at: 82nd Annual Conference of the DPG and DPG Spring Meeting, Erlangen, Germany. Mar. 2018.

5. **Heine, Hendrik**, Alexander Kassner, Marc C. Wurz, Waldemar Herr, and Ernst M. Rasel: "Planar diffraction optics on an atom chip." Poster presented at: 83rd Annual Conference of the DPG and DPG Spring Meeting, Rostock, Germany. Mar. 2019.

6. **Heine, Hendrik**, Alexander Kassner, Christoph Künzler, Wurz, Marc C., Waldemar Herr, and Ernst M. Rasel: "A single beam grating magneto optical trap on an atom chip." Presentation at the 84th Annual Conference of the DPG and DPG Spring Meeting, Hannover, Germany. Mar. 2020.

7. **Heine, Hendrik**, Joseph Muchovo, Aaditya Mishra, Waldemar Herr, Christian Schubert, and Ernst M. Rasel: "Single-beam laser cooling using a nano-structured atom chip." Presentation at the 86th Annual Conference of the DPG and DPG Spring Meeting, Hannover, Germany. Mar. 2022.

8. Mishra, Aaditya, **Hendrik Heine**, Joseph Muchovo, Waldemar Herr, Christian Schubert, and Ernst M. Rasel: "Simulating atom dynamics in grating magneto-optical trap." Presentation at the 86th Annual Conference of the DPG and DPG Spring Meeting, Hannover, Germany. Mar. 2022.

9. Lemburg, Julian, **Hendrik Heine**, Joseph Muchovo, Aaditya Mishra, Kai Bruns, Ernst M. Rasel, Waldemar Herr, and Christian Schubert: "A single beam grating magneto optical trap on an atom chip." Poster presentation at the 87th Annual Conference of the DPG and DPG Spring Meeting, Hannover, Germany. Mar. 2023.

10. Mishra, Aaditya, **Hendrik Heine**, Joseph Muchovo, Julian Lemburg, Kai Bruns, Waldemar Herr, Christian Schubert, and Ernst M. Rasel: "A single beam grating magneto optical trap on an atom chip." Poster presentation at the 87th Annual Conference of the DPG and DPG Spring Meeting, Hannover, Germany. Mar. 2023.

Curriculum Vitae

Personalien

Name	Hendrik Heine 🆔
	verheiratet, deutsch

Schulbildung

07/2009	Abitur, Gymnasium Wilhelm Raabe Schule Hannover

Wehrdienst

07/2009 – 08/2010	Stabsdienstsoldat, Panzerlehrbrigade 9, Munster

Studium

10/2010 – 10/2013	Leibniz Universität Hannover, Studium der Physik
	Thema der Bachelorarbeit: "Realisierung und Charakterisierung von Strahlformungsoptiken zur Kühlung von atomaren Ensembles", durchgeführt am Institut für Quantenoptik, Leibniz Universität Hannover
10/2013	Abschluss: Bachelor of Science
10/2013 – 10/2015	Leibniz Universität Hannover, Studium der Physik
	Thema der Masterarbeit: "Atominterferometrischer Test der Universalität des freien Falls mit Kalium und Rubidium", durchgeführt am Institut für Quantenoptik, Leibniz Universität Hannover
2014 – 2015	Deutschlandstipendium
10/2015	Abschluss: Master of Science

Promotion

11/2015 – heute	Wissenschaftlicher Mitarbeiter am Institut für Quantenoptik, Leibniz Universität Hannover
10/2017 – 12/2017	Mitgliedschaft in der Marie Skłodowska-Curie Gemeinschaft mit Forschungsaufenthalt in Birmingham, Großbritannien im Rahmen des Research and Innovation Staff Exchange (RISE) Horizon 2020 Programms der Europäischen Kommission.

Danksagungen

Danke an Alex, Tim und Matthias für eure gute Freundschaft! Ihr steht mir immer mit Rat und Tat zur Seite und ich hoffe, dass wir auch weiterhin viele freudige Stunden erleben können.

Meine Familie hat mir stets den Rücken gestärkt und mich unterstützt. Ich danke meinen Eltern Dirk und Petra sowie meiner Schwester Friederike für die Begleitung auf allen meinen Wegen! Vielen Dank auch an Oma Renate für die zahlreichen Ausflüge in unserer Jugend und die stetige Unterstützung.

Vielen vielen Dank an meine Frau Nina! Du stehst mir sowohl beruflich als auch privat jederzeit zur Seite. Es ist einfach super, dass wir auf unseren gemeinsamen beruflichen Erfahrungsschatz gegenseitig zurück greifen können, auch wenn dadurch die Arbeit gelegentlich mal mit nach Hause getragen wird. Ich freue mich auf unsere weitere gemeinsame Zukunft als Familie mit unserer Tochter Marie Sophie!